Ultra-Wideband Imaging Techniques for Medical Applications

Navid Ghavami

St. Hugh's College

A thesis submitted in partial fulfilment of the requirements for the degree of Doctor of Philosophy at the University of Oxford

Department of Engineering Science

Parks Road, Oxford OX1 3PJ, UK

Trinity 2013

Abstract

Ultra-wideband (UWB) radio techniques have long promised good contrast and high resolution for imaging human tissue and tumours; however, to date, this promise has not entirely been realised. In recent years, microwave imaging has been recognised as a promising non-ionising and non-invasive alternative screening technology, gaining its applicability to breast cancer by the significant contrast in the dielectric properties at microwave frequencies of normal and malignant tissues.

This thesis deals with the development of two novel imaging methods based on UWB microwave signals. First, the mode-matching (MM) Bessel-functions-based algorithm, which enables the identification of the presence and location of significant scatterers inside cylindrically-shaped objects is introduced. Next, with the aim of investigating more general 3D problems, the Huygens principle (HP) based procedure is presented. Using HP to forward propagate the waves removes the need to apply matrix generation/inversion. Moreover, HP method provides better performance when compared to conventional time-domain approaches; specifically, the signal to clutter ratio reaches 8 dB, which matches the best figures that have been published.

In addition to their simplicity, the two proposed methodologies permit the capture of a minimum dielectric contrast of 1:2, the extent to which different tissues, or differing conditions of tissues, can be discriminated in the final image. Moreover, UWB allows all the information in the frequency domain to be utilised, by combining information gathered from the individual frequencies to construct a consistent image with a resolution of approximately one quarter of the shortest wavelength in the dielectric medium. The power levels used and the specific absorption rates are well within safety limits, while the bandwidths satisfy the UWB definition of being at least 20% of the centre frequencies. It follows that the methodologies permit the detection and location of significant scatterers inside a volume. Validation of the techniques through both simulations and measurements have been performed and presented, illustrating the effectiveness of the methods.

Acknowledgements

First of all I would like to express my deep sincere gratitude to my supervisor Prof. David Edwards for his valuable advice, instructions and guidance through the course of my D.Phil degree.

I am truly grateful to the close supervision of Dr. Gianluigi Tiberi during his fellowship at the University of Oxford in the first six months of my D.Phil degree, and to our research collaboration with University of Pisa afterwards. Some of the initial experiments of this project were performed jointly with Dr Tiberi, and his explanations on theoretical and simulation parts were thoroughly helpful.

I am also thankful for the help and guidance provided by Dr. Chris Stevens and Prof. Safaai-Jazi.

I am much grateful to Mr. Grahame Faulkner for his technical assistance on designing and building various parts for my experiments and to my colleagues in the communications group for their occasional technical help, and to Aleksander Chmielewski for his valuable contribution in Microstripes simulations.

I would also like to thank EPSRC for their generous funding of my studies throughout my D.Phil program.

Many thanks to my relatives and close friends for their company and kind moral support.

Last but definitely not least, I have to thank my beloved parents and my sister Nooshin for their encouragement, patience and support during the time spent on this project.

List of publications

Journals:

1. N. Ghavami, G. Tiberi, D. J. Edwards and A. Monorchio, “UWB Microwave Imaging of Objects With Canonical Shape,” IEEE Transactions on Antennas and Propagation, vol. 60, no. 1, pp. 231-239, Jan. 2012.

2. G. Tiberi, N. Ghavami, D. J. Edwards and A. Monorchio, “Ultrawideband microwave imaging of cylindrical objects with inclusions,” Microwaves, Antennas & Propagation, IET, vol. 5, no. 12, pp. 1440-1446, Sep. 2011.

3. G. Tiberi, N. Ghavami, D. J. Edwards and A. Monorchio, “UWB Body Area Network Channel Modeling: an Analytical Approach,” AEUE - International Journal of Electronics and Communications, vol. 66, no. 11, pp. 913–919, Nov. 2012.

4. N. Ghavami, G. Tiberi, D. J. Edwards and A. Monorchio, “Microwave Imaging through a Mode Matching Bessel functions procedure,” IEEE Transactions on Microwave Theory and Techniques, vol. 61, no. 8, pp. 2753–2760, Jul. 2013.

5. N. Ghavami, G. Tiberi, D. J. Edwards, A. Safaai-Jazi and A. Monorchio, “UWB Microwave Imaging of Multilayered Objects with Inclusions,” AEUE - International Journal of Electronics and Communications, (Under review).

Conferences:

1. N. Ghavami, D. J. Edwards, G. Tiberi, A. Monorchio and G. Manara, “Huygens Principle based technique for microwave imaging of objects with inclusions,” International Conference on Electromagnetics in Advanced Applications (ICEAA), pp. 1044-1047, Torino, 12-16 Sep. 2011.

2. N. Ghavami, G. Tiberi and D. J. Edwards, “Huygens principle-based approach for UWB medical imaging,” 41st European Microwave Conference (EuMC), pp. 1257-1260, Manchester, 10-13 Oct. 2011.

3. G. Tiberi, N. Ghavami, D. J. Edwards and A. Monorchio, “Novel Techniques for UWB Microwave Imaging of Objects with Canonical Shape,” Progress in Electromagnetics Research Symposium Proceedings, pp. 808-812, Marrakesh, Morocco, 20-23 Mar. 2011.

4. G. Tiberi, N. Ghavami, D. J. Edwards and A. Monorchio, “A mode matching - Bessel functions based approach for UWB microwave imaging,” 2010 IEEE Antennas and Propagation Society International Symposium (APS/URSI), Toronto, 11-17 July 2010.

5. G. Tiberi, N. Ghavami and D. J. Edwards, “A mode matching - Bessel functions based approach for UWB microwave imaging: validation through measurements,” 2010 IEEE Antennas and Propagation Society International Symposium (APS/URSI), Toronto, 11-17 July 2010.

List of abbreviations

BAN	Body Area Network
CAD	Computer Aided Design
CBFM	Characteristics Basis Function Method
CST	Computer Simulation Technology
CT	Computed Tomography
DFT	Discrete Fourier Transform
EIRP	Equivalent Isotropically Radiated Power
FCC	Federal Communication Commission
FDTD	Finite Difference Time Domain
FWHM	Full-Width at Half-Maximum
GPS	Global Positioning System
HP	Huygens Principle
IDFT	Inverse Discrete Fourier Transform
LMS	Least Mean Square
MIST	Microwave Imaging via Space-Time
MIT	Massachusetts Institute of Technology
MM	Mode Matching
MRI	Magnetic Resonance Imaging
NB	Narrow Band
PEC	Perfectly Electrically Conducting
P.M.M.A.	Poly Methyl Methacrylate
PSD	Power Spectral Density
PVC	Polyvinyl Chloride
RF	Radio Frequency
Rx	Receiver

SAR	Specific Absorption Rate
S/C	Signal to Clutter Ratio
TLM	Transmission Line Matrix
TR	Time Reversal
Tx	Transmitter
UTD	Uniform Theory of Diffraction
UWB	Ultra Wideband
VNA	Vector Network Analyser

List of symbols

B_f	Fractional bandwidth
f_H	Upper -10dB frequency
f_L	Lower -10dB frequency
V	Volume of interest
f	Frequency
μ	Permeability
ε	Dielectric constant (relative permittivity)
k	Wave number
$\overrightarrow{E}^i$	Plane wave
E_0	Amplitude of the plane wave
σ	Electrical conductivity
α	Integer order of Bessel function
$\Gamma(z)$	Gamma function
tx_m	Transmitting source
rx_{np}	Receiving positions
N_{PT}	Number of measured points
A, B, Z	Matrices
Δ_s	Spatial sampling
N_f	Summation truncation value
M	Number of transmitting sources
I	Intensity
Δ_f	Frequency sampling
B	Bandwidth
$\lambda_{f_{\max}}$	Wavelength calculated at the highest frequency

List of Figures

List of Tables

Contents

1

Introduction and Literature Review

1.1 Fundamentals of UWB

1.1.1 Historical Background

Ultra-wideband (UWB) is known as a new and emerging technology, although the first use of it goes back as far as many decades. In 1973 the first US patent was awarded to Sperry research centre for UWB communications [1]. For years, most of the applications and development of UWB occurred in the military or work funded by the US government under classified programs and the technology was alternatively referred to as baseband, carrier-free or impulse communication systems. By 1989, over 50 patents had been awarded to the Sperry research centre in the field covering UWB pulse generation and reception methods, in applications such as communications, radar, automobile collision avoidance, liquid level sensing, positioning systems and altimetry [2, 3]. The move to commercialise UWB communication devices and systems came in the late 1990s, when companies such as Time Domain [4] and XtremeSpectrum [5] were formed around the idea of consumer communications using UWB.

1.1.2 UWB Definitions and Regulations

In 2002, the USA based Federal Communication Commission (FCC) [6, 7], allocated a bandwidth of 7.5 GHz for UWB signals [8]. This bandwidth covers a frequency band of 3.1 to 10.6 GHz. The large spectrum covered by UWB signals results in some interference with existing users. In order to minimise this interference, the FCC and other regulatory groups specify spectral masks for different applications which show the allowed power output for specific frequencies. The spectral mask allocated by FCC for indoor applications is shown in fig. 1.1 [9]. By observing this spectral mask it can be seen that this frequency band has the largest UWB equivalent isotropically radiated power (EIRP) emission level of about -41.3 dBm/MHz among all frequencies, while the frequency band of 0.96-1.61 GHz has the lowest emission level due to usage from other applications such as the global positioning system (GPS).

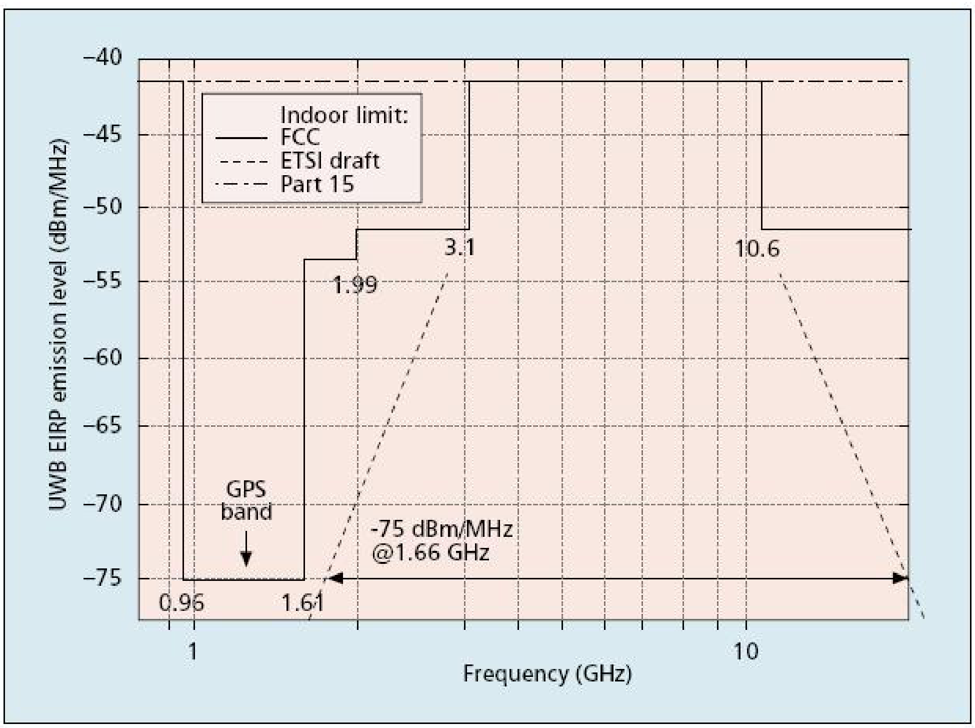

Figure 1.1: Indoor spectral mask allocated by FCC [9].

In order for any signal to be considered as a UWB signal, it must either have a bandwidth of at least 500 MHz, or it should have a fractional bandwidth of greater than 20% in the range defined by the FCC. The fractional bandwidth, B_f is defined as follows:

$$B_f = 2\left(\frac{f_H - f_L}{f_H + f_L}\right) \tag{1.1}$$

where f_H and f_L represent the upper and lower -10 dB frequencies of the spectrum of the signal, respectively.

1.1.3 UWB vs. Narrow Band

Comparing UWB signals with the conventional narrow band (NB) signals shows the key differences between them. UWB signals have a much lower power spectrum. The reason is, due to the large bandwidth occupied by UWB signals there would be a probability of interference between UWB signals and other communication systems, but we also do not require a high power spectral to be achieved. Therefore, the power spectrum of UWB is reduced. These differences can be seen in fig. 1.2 [10].

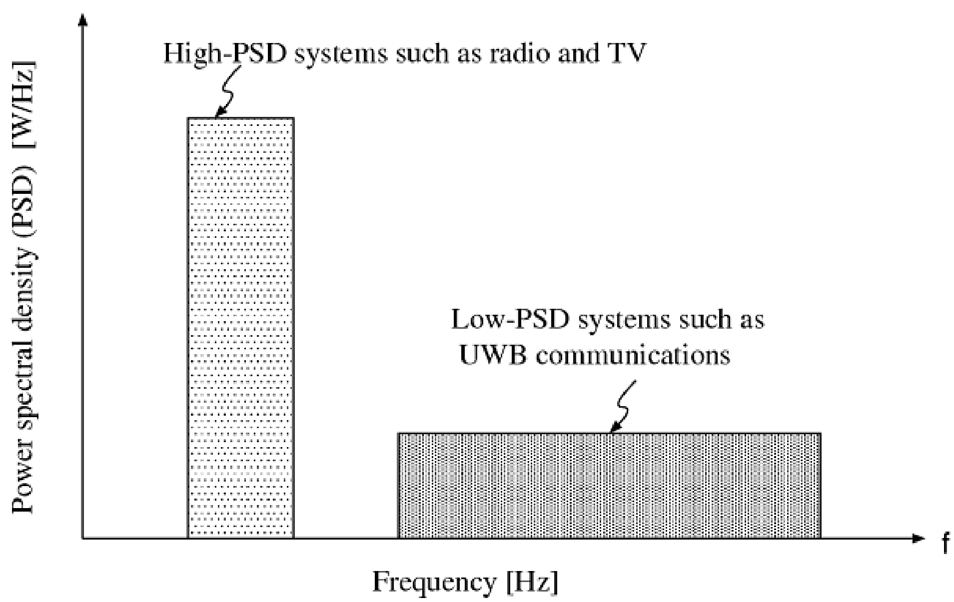

Figure 1.2: Comparison between UWB and NB signals in terms of bandwidth and power spectral density (PSD) [10].

1.1.4 UWB Benefits and Applications

There are a wide range of benefits and advantages associated with UWB signals. The key benefits are [10]:

- High data rates
- Low equipment cost
- Multipath immunity
- Ranging and communication at the same time

Having these advantages and using low power, ultra short information pulses and not requiring sine-wave carriers in modulation, enables UWB signals to be used in a wide range of applications, which include precision navigation, through wall imaging, high resolution ground penetrating radar and short range and high-speed broadband access [8].

1.2 Medical Applications of UWB

1.2.1 History of UWB Medical Applications

There has been an increasing interest in the application of the UWB technology to the medical field in recent years. The first suggestion for such application was presented in the 1970s, but was rejected due to size, cost and safety reasons [11]. However, the interest was regenerated in August 1994, by T. E. McEwan's patent on "Micropower impulse radar". In the following year, Massachusetts Institute of Technology (MIT) began an educational project focusing on the "Radar Stethoscope" [12]. In 1996, the addition of photo and sample tracing improved and simplified the biomedical use of UWB radars and in the same year, McEwan's patent on "Body monitoring and imaging apparatus and method" was awarded [13]. Ever since, UWB has been considered as an alternative to remote sensing and imaging. Its characteristics, such as having a very low average power level, using short pulses, and its power efficiency have transformed the UWB into a suitable and potentially cost effective way of human body imaging, especially in real time applications [14].

1.2.2 Existing Imaging Techniques

In recent years, there has been a growing interest in the development of imaging methods for medical applications. A number of existing medical imaging technologies are already in use today. These technologies are able to produce well-defined tomographic reconstructions of living tissues using a range of media. Most common are ultrasound scanners, X-ray based computed tomography (CT), and the radio frequency (RF) technique of nuclear magnetic resonance imaging (known as MRI). Each one of these established imaging techniques has its own drawbacks; for example, ultrasound is a very cost-effective technique and is extremely useful for selected tissues, but suffers from contrast problems and an inability to image objects with large acoustic impedance differences like air spaces and bones [15]. CT, on the other hand, is very effective for imaging of high-contrast subjects, but does result in significant dose of ionising radiation, and thus has limited application [16]. Finally, while MRI does not cause ionising radiation, it is quite expensive to purchase, maintain and operate. In addition, it has a long scan time, which for a whole body can take as long as 2 hours during which time the patient is required to remain quite still within the confines of a rather cramped and claustrophobic environment.

Moreover, concerning breast cancer detection, the limitations of conventional X-ray mammograms are well recognised. For example, this technique, even in high resolution images, with relatively low radiation doses, misses approximately 15% of all cancers while 75% of the identified breast lesions are in fact benign [17]. In response to all these limitations, microwave imaging has been recognised as a promising non-ionising and non-invasive alternative screening technology for these application areas.

1.2.3 Current Microwave Imaging Techniques

Microwave imaging has attracted growing attention in the last decade, especially for its applicability to breast cancer detection, motivated by the contrast in the dielectric properties at microwave frequencies of normal and malignant tissues. Addressing an imaging problem involves estimating the distribution of the field within a volume V based upon observations of the field on the surface of V, and this involves estimating the distribution of dielectric properties within the target volume. In recent years, other medical applications of microwave imaging, such as bone imaging [18, 19] have also been investigated.

Current research in microwave breast imaging can be divided mainly into microwave tomography, UWB radar techniques and microwave holography. In tomographic image reconstruction, a nonlinear inverse scattering problem is solved to recover an image of the dielectric properties in the breast [20, 21]. Such non-linear (and ill-posed) problems can be addressed by resorting to a number of methods, including conventional conjugate gradient methods and the modified Born iterative method [21]. More recently, a new analytical approach (partly based on previous work [22, 23]) has been introduced by reformulating the inverse scattering problem as an inverse source one. The approach requires the calculation of both the radiating and the non-radiating parts of the induced currents, and permits an efficient solution of 2D problems [24, 25].

In contrast to tomography, the UWB radar approach solves a simpler computational problem by seeking only to identify the significant scatterers [26-30]. In order to reconstruct the image, beamforming techniques of varying complexity are required. Current beamforming techniques use time domain processing algorithms; one method is confocal imaging which employs simple delay-and-sum beamforming [26, 27]. However, while confocal processing is computationally inexpensive, it presents major problems in imaging spaces which possess volumes of varying dielectric constant. In fact, internal refraction cannot be easily removed and would render the image inaccurate. An alternative technique, microwave imaging via space-time (MIST) beamforming [28, 29], uses filters that compensate for dispersion and fractional time delays. The filters solve a penalised least-squares problem such that signals originating from a candidate tumour location are passed with approximately unit amplitude and linear phase while the white noise gain is constrained. Filter designs improve clutter suppression and spatial discrimination, but they lead to an increase of complexity and computational burden. In [30], data-adaptive beamforming is proposed which accounts for some uncertainties during preprocessing steps, e.g. non-ideal time-delays, or errors in amplitude compensation.

Time-reversal (TR) based approaches have also been proposed in [31] and [32]. TR is based on the following assumption: If the scattered fields at the receiver are time-reversed and computationally reradiated into the medium, focussing is achieved at the source point. However, reradiation into the medium is possible if an approximate knowledge of the channel transfer function associated with the numerical back-propagation is known.

In microwave holography, targets in the near-field range are reconstructed by using a Fourier analysis of the wideband transmission and reflection signals recorded by antennas scanning together on both sides of the inspected region [33].

In this context, the aim of this research has been to develop novel, fast and accurate UWB microwave imaging methods. First, a procedure based on the mode-matching (MM) of Bessel functions, which permits to identify the presence and location of significant scatterers inside cylindrically-shaped objects, will be introduced. Next, with the aim of investigating more general 3D problems, a method based on Huygens Principle (HP) is presented. Using the MM procedure leads to the generation/inversion of a rather small matrix; conversely, using HP to forward propagate the waves removes the need to solve inverse problems and, consequently, no matrix generation/inversion is required. Together with their simplicity, the two methodologies permit the capturing of the extent to which different tissues, or differing conditions of tissues, can be discriminated, and hence render contrast in the final image. Moreover, UWB allows all the information in the frequency domain to be utilised by combining the information from the individual frequencies to construct a consistent image. Validation of the techniques through both simulations and measurements on cylinders and spheres with inclusions has been performed and the results are presented, illustrating the effectiveness of the methods. Potential application would be breast cancer detection, internal organ imaging, and whole body imaging.

1.3 Thesis Organisation

We now proceed with a chapter-by-chapter description of the thesis, pointing out the major contributions.

In chapter 2, the propagation of UWB signals in human tissue is investigated analytically, such that the body is modelled as a cylinder of infinite length, and Maxwell's equation is solved for plane wave and line source excitations. First, a simple perfectly electrically conducting (PEC) cylinder is considered; next, the complexity is increased considering homogeneous dielectric cylinder, 2-layer stratified cylinders, and 3-layer stratified cylinders, respectively. Finally, human-type tissue is assumed in a multilayered stratified cylinder model. In order to validate the analytical method, the comparison between the analytical frequency response and that of measurement involving a multilayered medium is presented in the last section.

The first of the two proposed imaging methods based on UWB microwave signals is described and investigated in chapter 3. The method is based on the MM of Bessel functions. In the first section, a complete analytical explanation of the MM procedure is formulated. In the last two sections the validation of the method through a number of simulations and measurements involving cylindrical shapes with inclusions is performed.

Chapter 4 investigates the second proposed imaging technique, which employs the Huygens Principle. The formulation of HP is presented in details in section 4.2. Next, the validation of the technique through simulations on cylindrical mediums with one or more inclusions is shown and the performance of HP procedure in comparison with some of the recent imaging techniques is investigated. Afterwards, HP is validated through measurements involving cylindrical mediums with one or more inclusions, and a further measurement extending the imaging to a 3D medium (sphere) with an inclusion is also performed; all the measurement results are presented in the final section of this chapter.

In chapter 5, the application of the HP method is extended to more realistic geometries constituting of multiple layers. In section 5.2, the procedure is verified through realistic simulations involving 3-layer cylindrical mediums, based on analytical calculations of section 2.8. In section 5.3, the validation of the method through measurements on a 4-layer cylinder with an inclusion is presented.

Chapter 6 presents the further extension of the HP method to cover simulations and measurements involving realistic inhomogeneous hemispherical phantoms with one more inclusions. In section 6.2, the data obtained from Microstripes^{TM}, a commercial transmission line matrix (TLM) analysis package is used in the reconstruction process for simulation purposes of an inhomogeneous breast model. Additionally, measurement results on a commercially fabricated breast phantom with multiple hidden inclusions is presented in section 6.4, and the results are compared to that of an Elastography scanning machine presented in section 6.3. At the end of the chapter, the measurement is repeated with cross-polar and horizontal polarisation configurations, and the polarisation issues of the discone antennas used in 3D measurements are also investigated.

The last chapter concludes the thesis and contains a discussion of topics for future research.

2

Human Body Modelling

2.1 Introduction

UWB wireless biomedical sensors is a promising new application area made possible by recent advances in ultra low power technology. Each sensor measures parameters of interest and sends the data in short bursts to a central device. Examples include sensors to observe brain activity for recording or warning against seizure events, to examine heart activity for diagnosis and automatic emergency calls, to measure glucose levels in diabetic patients, and to monitor oxygen, blood pressure, or disease markers. The large diversity and potential of these applications makes it an exciting new research direction in wireless communications.

In developing these sensors, detailed knowledge of the body area network (BAN) communication channel is essential. Measurements [34] and finite difference time domain (FDTD) simulations [35] have been successfully applied for specific communication scenarios. However, measurements do not directly consider the physical propagation mechanism, forcing researchers to rely on ad-hoc modelling approaches. On the other hand, realistic FDTD simulations that numerically evaluate the solution to Maxwell's equations of small antennas worn close to the sophisticated curved inhomogeneous human bodies are very time-consuming. Another approach resorts to the uniform theory of diffraction (UTD) [36]; while this approach offers considerable physical insight, it typically relies on a high-frequency asymptotic approximation. Here, in contrast to conventional approaches based on FDTD methods, the propagation of UWB signals in human tissue will be investigated analytically. In detail, the body will be modelled as a cylinder of infinite length, and Maxwell's equation will be solved for plane wave and line source excitation. First, a simple perfectly electrically conducting (PEC) cylinder will be considered; next, the complexity will be increased considering homogeneous dielectric cylinder, 2-layer stratified cylinders, and 3-layer stratified cylinders, respectively. Finally, human-type tissue will be assumed in the multilayered stratified cylinder model. In order to validate the analytical method, the comparison between the analytical frequency response and that of measurement involving a multilayered medium will be presented in the last section.

2.2 Bessel Functions

For a long time, Bessel functions have been widely used in mathematics [37, 38]. They were first described by Dutch-Swiss mathematician Daniel Bernoulli [39] and were later generalised by Friedrich Bessel [40]. Bessel functions are defined as canonical solutions $y(x)$ of Bessel's differential equation such that:

$$x^2\frac{d^2y}{dx^2}+x\frac{dy}{dx}+(x^2-\alpha^2)y=0 \tag{2.1}$$

where α is an arbitrary real or complex number representing the order of the function. Bessel functions are divided into different kinds (orders), and the common ones are described below.

2.2.1 First Kind

J_α: $J_\alpha(x)$ are solutions of Bessel's differential equation that are finite at the origin ($x = 0$) for integer α, and diverge as x approaches 0 for negative non-integer α [41].

$$J_\alpha(x) = \sum_{m=0}^{\infty} \frac{(-1)^m}{m!\Gamma(m+\alpha+1)} \left(\frac{x}{2}\right)^{2m+\alpha} \tag{2.2}$$

where, $\Gamma(\cdot)$ is the Gamma function.

Figure 2.1 shows a plot of the Bessel function of the first kind $J_\alpha(x)$ for integer orders $\alpha = 0, 1, 2$.

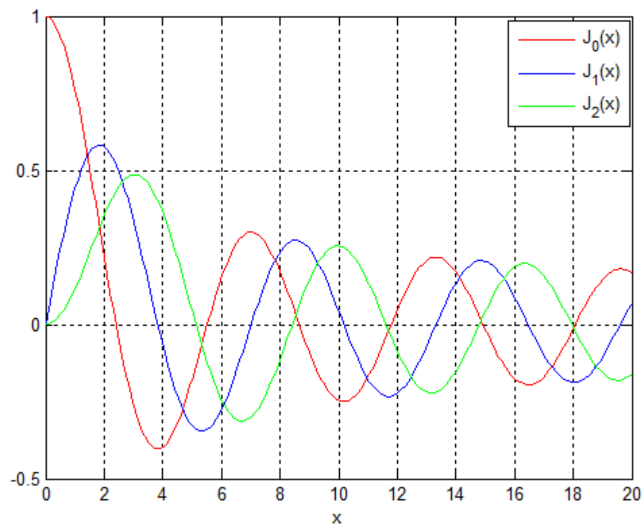

Figure 2.1: Plot of Bessel function of the first kind, $J_\alpha(x)$, for integer orders $\alpha = 0, 1, 2$.

2.2.2 Second Kind

Y_α: $Y_\alpha(x)$ are solutions of Bessel's differential equation. They have singularity at the origin ($x = 0$). They are sometimes referred to as Neumann or Weber functions [42].

$$Y_\alpha(x) = \frac{J_\alpha(x)\cos(\alpha\pi) - J_{-\alpha}(x)}{\sin(\alpha\pi)} \tag{2.3}$$

A plot of Bessel function of the 2nd kind, $Y_\alpha(x)$, for integer orders $\alpha = 0,\ 1,\ 2$ is shown in fig. 2.2.

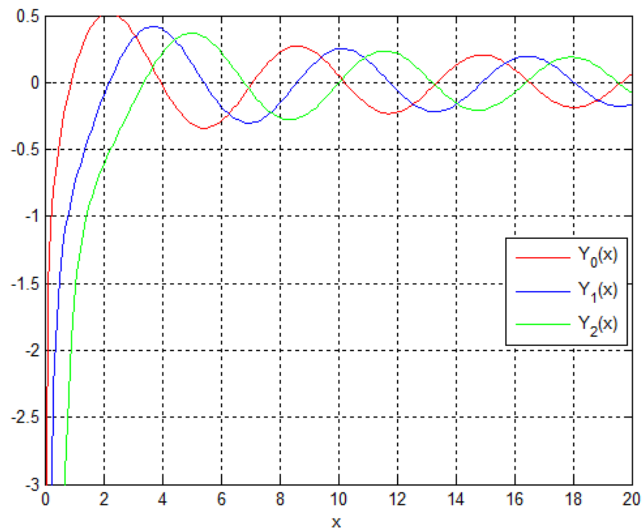

Figure 2.2: Plot of Bessel function of the second kind, $Y_\alpha(x)$, for integer orders $\alpha = 0, 1, 2$.

2.2.3 Hankel Functions (Third Kind)

H_α: Formulation of 2 linearly independent solutions to Bessel's equations are the Hankel functions $H_\alpha^{(1)}(x)$ and $H_\alpha^{(2)}(x)$ defined by:

$$H_\alpha^{(1)}(x) = J_\alpha(x) + iY_\alpha(x) = \frac{J_{-\alpha}(x) - e^{-\alpha\pi i}J_\alpha(x)}{i\sin(\alpha\pi)} \tag{2.4}$$

$$H_\alpha^{(2)}(x) = J_\alpha(x) - iY_\alpha(x) = \frac{J_{-\alpha}(x) - e^{\alpha\pi i}J_\alpha(x)}{-i\sin(\alpha\pi)} \tag{2.5}$$

where i is the imaginary unit. These linear combinations are also known as Bessel functions of the third kind, as such, they are two linearly independent solutions of Bessel's differential equation [43].

2.2.4 Modified Bessel Functions

I_α, K_α: Bessel functions are valid even for a complex argument x, for which a special case is that of a purely imaginary argument. Such solutions are referred to as modified (hyperbolic) bessel functions of the first and second kinds, defined as follows:

$$I_\alpha(x) = i^{-\alpha} J_\alpha(ix) = \sum_{m=0}^{\infty} \frac{1}{m!\Gamma(m+\alpha+1)} \left(\frac{x}{2}\right)^{2m+\alpha} \tag{2.6}$$

$$K_\alpha(x) = \frac{\pi}{2} \cdot \frac{I_{-\alpha}(x) - I_\alpha(x)}{\sin(\alpha\pi)} = \frac{\pi}{2} i^{\alpha+1} H_\alpha^{(1)}(ix) \tag{2.7}$$

where $I_\alpha(x)$ and $K_\alpha(x)$ are two linearly independent solutions to the modified Bessel's equation [44]:

$$x^2 \frac{d^2y}{dx^2} + x\frac{dy}{dx} - (x^2 + \alpha^2)y = 0 \tag{2.8}$$

Figures 2.3(a) and 2.3(b) show the plots of $I_\alpha(x)$ and $K_\alpha(x)$, for integer orders $\alpha = 0, 1, 2, 3$, respectively. It can be seen that unlike the oscillating behaviour of ordinary Bessel functions, $I_\alpha(x)$ and $K_\alpha(x)$ are exponentially growing and decaying functions, respectively.

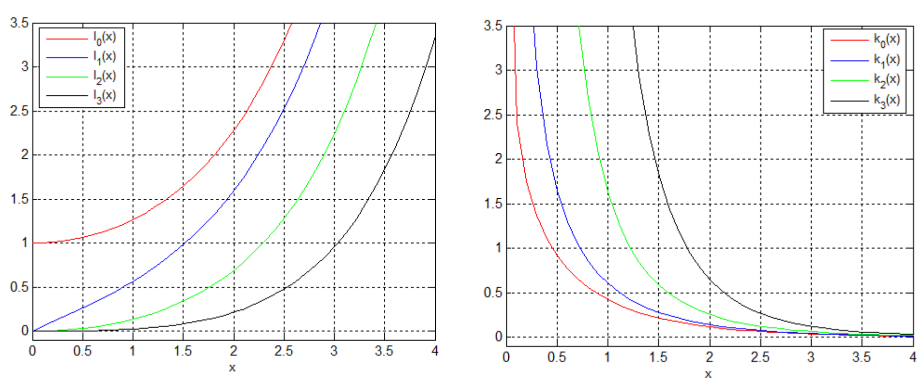

(a) (b)

Figure 2.3: Plot of modified Bessel functions (a) 1st kind, $I_\alpha(x)$, (b) 2nd kind, $K_\alpha(x)$ for integer orders $\alpha = 0, 1, 2, 3$.

2.3 PEC Cylinder

Let us consider a PEC cylinder in free space with radius a illuminated by a plane wave having a z-polarised E-field and travelling along the x-axis (fig. 2.4). In free space, characterised by ε_0 and μ_0, we define:

$$k_0 = \sqrt{(2\pi f)^2 \varepsilon_0 \mu_0} \tag{2.9a}$$

$$Z_0 = \sqrt{\frac{\mu_0}{\varepsilon_0}} \tag{2.9b}$$

where f is the frequency of the plane wave. Thus, it holds:

$$\overrightarrow{E}^i = E_0 \widehat{i}_z e^{-jk_0 x} \tag{2.10}$$

with E_0 representing the amplitude of the plane wave $\overrightarrow{E}^i$. The total field inside the cylinder is

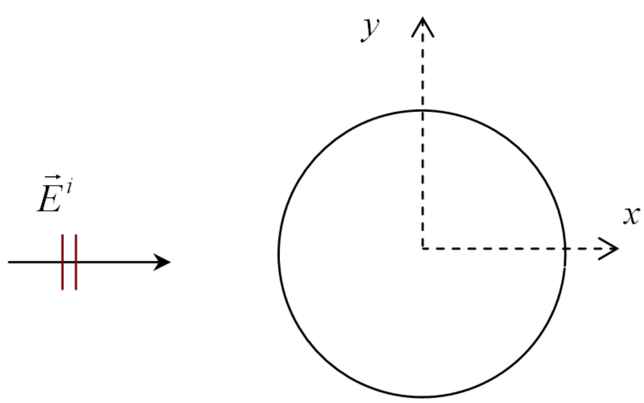

Figure 2.4: PEC cylinder in free space.

the sum of the incident and scattered fields, that is:

$$E_z = E_z^i + E_z^s \tag{2.11}$$

By using the cylindrical expansion and cylindrical coordinates (ρ,ϕ), we can write [45]:

$$E_z^i = E_0 \sum_{n=-\infty}^{+\infty} (-j)^n J_n(k_0\rho) e^{jn\phi} \tag{2.12}$$

$$E_z^s = E_0 \sum_{n=-\infty}^{+\infty} (-j)^n a_n H_n^{(2)}(k_0\rho) e^{jn\phi} \tag{2.13}$$

where $J_n(k_0\rho)$ and $H_n^{(2)}(k_0\rho)$ are Bessel functions of the first and third kind, respectively. At the cylinder, the boundary condition $E_z = 0$ at $\rho = a$ must be met. By using the orthogonality of the exponential functions, the coefficient a_n can be determined as follows:

$$a_n = -\frac{J_n(k_0 a)}{H_n^{(2)}(k_0 a)} \tag{2.14}$$

To evaluate the scattered field, the infinite summation in eq. (2.13) has to be truncated; thus, it follows:

$$E_z^s \approx E_0 \sum_{n=-N_F}^{+N_F} (-j)^n a_n H_n^{(2)}(k_0\rho) e^{jn\phi} \tag{2.15}$$

For the examples presented here, a check on the error in boundary conditions, i.e. average relative error lower than 10^{-3}, leads to N_F=50. Note that this value is related to $k_0 a$.

2.4 Homogeneous Cylinder

Let us now consider a dielectric homogenous cylinder in free space with radius a illuminated by the plane wave of eq. (2.10). The dielectric is characterised by relative constants ε_{r1}, μ_{r1}, and by conductivity σ_1. It holds that μ_{r1}=1, and:

$$\varepsilon_1 = \varepsilon_0 \varepsilon_{eq1}, \quad \mu_1 = \mu_0 \quad \text{with} \quad \varepsilon_{eq1} = (\varepsilon_{r1} - j\frac{\sigma_1}{2\pi f \varepsilon_0}) \tag{2.16}$$

From eq. (2.16) it is evident that, if $\sigma_1 \neq 0$, ε_{eq1} varies with frequency. It is worthwhile to point out that when dealing with human tissues, the frequency-dependence of ε_{r1} and σ_1 has to be taken into account as well. More concisely, it can be stated that the cylinder is characterised by ε_1, μ_1, both of which can be complex and can vary with the frequency. Next, we define the quantities:

$$k_1 = \sqrt{(2\pi f)^2 \varepsilon_1 \mu_1} \tag{2.17a}$$

$$Z_1 = \sqrt{\frac{\mu_1}{\varepsilon_1}} \tag{2.17b}$$

We proceed by writing the following equations [45]:

$$E_z^0 = E_0 \sum_{n=-\infty}^{+\infty} (-j)^n J_n(k_0\rho) e^{jn\phi} + E_0 \sum_{n=-\infty}^{+\infty} (-j)^n a_n H_n^{(2)}(k_0\rho) e^{jn\phi} \tag{2.18a}$$

$$E_z^1 = E_0 \sum_{n=-\infty}^{+\infty} (-j)^n b_n J_n(k_1\rho) e^{jn\phi} \tag{2.18b}$$

Eqs. (2.18) hold in free space and inside the cylinder respectively. Moreover, we have [45]:

$$H_\phi^0 = \frac{E_0}{jZ_0} \sum_{n=-\infty}^{+\infty} (-j)^n J_n'(k_0\rho) e^{jn\phi} + \frac{E_0}{jZ_0} \sum_{n=-\infty}^{+\infty} (-j)^n a_n H'^{(2)}_n(k_0\rho) e^{jn\phi} \tag{2.19a}$$

$$H_\phi^1 = \frac{E_0}{jZ_1} \sum_{n=-\infty}^{+\infty} (-j)^n b_n J_n'(k_1\rho) e^{jn\phi} \tag{2.19b}$$

Again, eqs. (2.19) hold in free space and inside the cylinder, respectively. All the coefficients can be determined by imposing the boundary conditions of E and H fields on the surface. Thus, the field can be determined in each region.

2.5 2-Layer Stratified Concentric Cylinder

Next, a 2-layer stratified concentric dielectric cylinder in free space illuminated by the plane wave of eq. (2.10) is considered. The two cylinders are concentric and are indicated as cylinder

'1' and cylinder '2' (fig. 2.5).

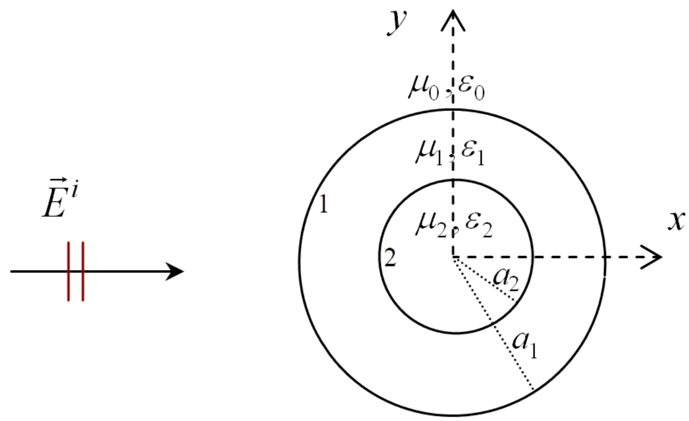

Figure 2.5: 2-layer stratified concentric cylinder in free space.

Cylinders '1' and '2' are characterised by ε_1, μ_1 and ε_2, μ_2, respectively, which can be complex and can vary with the frequency [see eq. (2.16)]. It holds:

$$k_2 = \sqrt{(2\pi f)^2 \varepsilon_2 \mu_2} \tag{2.20a}$$

$$Z_2 = \sqrt{\frac{\mu_2}{\varepsilon_2}} \tag{2.20b}$$

We proceed by deriving the following equations, where ϕ_0 has now been introduced to represent the angle of incidence of the plane wave:

$$E_z^0 = E_0 \sum_{n=-\infty}^{+\infty} (-j)^n J_n(k_0\rho) e^{jn(\phi-\phi_0)} + E_0 \sum_{n=-\infty}^{+\infty} (-j)^n a_n H_n^{(2)}(k_0\rho) e^{jn(\phi-\phi_0)} \tag{2.21a}$$

$$E_z^1 = E_0 \sum_{n=-\infty}^{+\infty} (-j)^n b_n J_n(k_1\rho) e^{jn\phi} + E_0 \sum_{n=-\infty}^{+\infty} (-j)^n c_n H_n^{(2)}(k_1\rho) e^{jn\phi} \tag{2.21b}$$

$$E_z^2 = E_0 \sum_{n=-\infty}^{+\infty} (-j)^n d_n J_n(k_2\rho) e^{jn\phi} \tag{2.21c}$$

Above equations hold in free space, inside cylinder '1' and inside cylinder '2', respectively.

Moreover, we derive the following:

$$H_\phi^0 = \frac{E_0}{jZ_0}\sum_{n=-\infty}^{+\infty}(-j)^n J_n'(k_0\rho)e^{jn(\phi-\phi_0)} + \frac{E_0}{jZ_0}\sum_{n=-\infty}^{+\infty}(-j)^n a_n {H'}_n^{(2)}(k_0\rho)e^{jn(\phi-\phi_0)} \tag{2.22a}$$

$$H_\phi^1 = \frac{E_0}{jZ_1}\sum_{n=-\infty}^{+\infty}(-j)^n b_n J_n'(k_1\rho)e^{jn\phi} + \frac{E_0}{jZ_1}\sum_{n=-\infty}^{+\infty}(-j)^n c_n {H'}_n^{(2)}(k_1\rho)e^{jn\phi} \tag{2.22b}$$

$$H_\phi^2 = \frac{E_0}{jZ_2}\sum_{n=-\infty}^{+\infty}(-j)^n d_n J_n'(k_2\rho)e^{jn\phi} \tag{2.22c}$$

Again, eqs. (2.22) hold in free space, inside cylinder '1' and inside cylinder '2', respectively. The coefficients a_n, b_n, c_n and d_n can be determined by imposing the boundary conditions of E and H field on the surfaces of '1' and '2'. For the sake of clarity, we rename the coefficient in the following way:

$$\begin{aligned} a_n &\to o_{0,n} \\ b_n &\to i_{1,n} \\ c_n &\to o_{1,n} \\ d_n &\to i_{2,n} \end{aligned} \tag{2.23}$$

where the acronyms o, i indicate the outward and inward waves, and the indexes 0, 1, 2 indicate the correspondent media. Thus, by using the orthogonality of exponential functions, we have:

$$J_n(k_0a_1)e^{-jn\phi_0} + o_{0,n}H_n^{(2)}(k_0a_1)e^{-jn\phi_0} = i_{1,n}J_n(k_1a_1) + o_{1,n}H_n^{(2)}(k_1a_1) \tag{2.24a}$$

$$\frac{1}{jZ_0}J_n'(k_0a_1)e^{-jn\phi_0} + \frac{1}{jZ_0}o_{0,n}H_n'^{(2)}(k_0a_1)e^{-jn\phi_0} = \frac{1}{jZ_1}i_{1,n}J_n'(k_1a_1) + \frac{1}{jZ_1}o_{1,n}H_n'^{(2)}(k_1a_1) \tag{2.24b}$$

$$i_{1,n}J_n(k_1a_2) + o_{1,n}H_n^{(2)}(k_1a_2) = i_{2,n}J_n(k_2a_2) \tag{2.24c}$$

$$\frac{1}{jZ_1}i_{1,n}J_n'(k_1a_2) + \frac{1}{jZ_1}o_{1,n}H_n'^{(2)}(k_1a_2) = \frac{1}{jZ_2}i_{2,n}J_n'(k_2a_2) \tag{2.24d}$$

Next, we proceed with some algebraic manipulation, eq. (2.24a) becomes:

$$o_{0,n} = \frac{1}{H_n^{(2)}(k_0a_1)}\left[-J_n(k_0a_1) + e^{jn\phi_0}\left(i_{1,n}J_n(k_1a_1) + o_{1,n}H_n^{(2)}(k_1a_1)\right)\right] \tag{2.25}$$

Combining eqs. (2.24c) and (2.24d), we can write:

$$i_{2,n} = \frac{i_{1,n}J_n(k_1a_2) + o_{1,n}H_n^{(2)}(k_1a_2)}{J_n(k_2a_2)} \tag{2.26a}$$

$$o_{1,n} = -\frac{A}{B}i_{1,n} \tag{2.26b}$$

with

$$A = \frac{1}{Z_1}J_n'(k_1a_2) - \frac{1}{Z_2}J_n(k_1a_2)\frac{J_n'(k_2a_2)}{J_n(k_2a_2)}, \quad B = \frac{1}{Z_1}H_n'^{(2)}(k_1a_2) - \frac{1}{Z_2}H_n^{(2)}(k_1a_2)\frac{J_n'(k_2a_2)}{J_n(k_2a_2)} \tag{2.26c}$$

Using eqs. (2.25) and (2.26) in eq. (2.24b), $i_{1,n}$ can be solved:

$$i_{1,n} = -\frac{C}{D}e^{-jn\phi_0} \tag{2.27}$$

with,

$$C = \frac{1}{Z_0}J_n'(k_0a_1) - \frac{1}{Z_0}J_n(k_0a_1)\frac{H_n'^{(2)}(k_0a_1)}{H_n^{(2)}(k_0a_1)} \tag{2.28}$$

and,

$$D = \frac{J_n(k_1a_1)}{Z_0}\cdot\frac{H_n'^{(2)}(k_0a_1)}{H_n^{(2)}(k_0a_1)} - \frac{A}{B}\cdot\frac{H_n^{(2)}(k_1a_1)}{Z_0}\cdot\frac{H_n'^{(2)}(k_0a_1)}{H_n^{(2)}(k_0a_1)} - \frac{J_n'(k_1a_1)}{Z_1} + \frac{A}{B}\cdot\frac{H_n'^{(2)}(k_1a_1)}{Z_1} \tag{2.29}$$

Once we have $i_{1,n}$, we go back to calculate the others coefficients. Thus, the field can be determined in each region.

2.6 2-Layer Stratified Eccentric Cylinder

Let us now consider a 2-layer stratified cylinder in free space illuminated by the plane wave of eq. (2.10). The two cylinders are eccentric and are indicated as cylinder '1' and cylinder '2' (fig. 2.6).

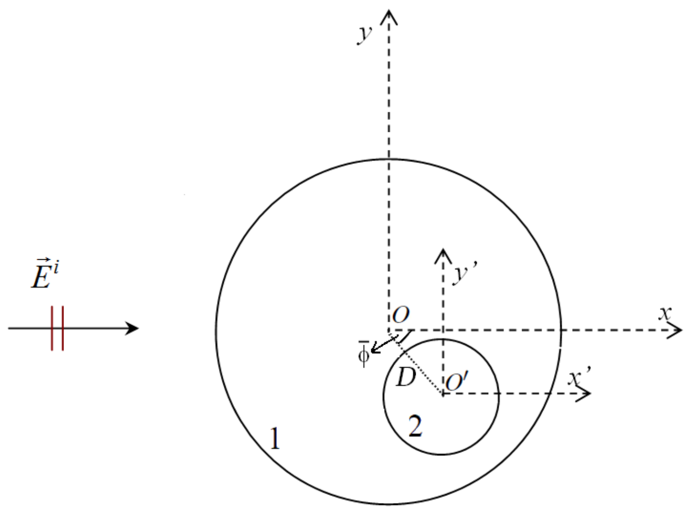

Figure 2.6: 2-layer stratified eccentric cylinder in free space.

Cylinder '1' and cylinder '2' have radii a_1 and a_2, respectively; the distance between the centres is $OO' = D$ and the angle between OO' and the x-axis is $\overline{\phi}$. We proceed to calculating the fields by writing the following field expressions for axial components [46]:

$$E_z^0 = E_0 \sum_{n=-\infty}^{+\infty} (-j)^n J_n(k_0\rho) e^{jn(\phi-\phi_0)} + E_0 \sum_{n=-\infty}^{+\infty} (-j)^n a_n H_n^{(2)}(k_0\rho) e^{jn(\phi-\phi_0)} \tag{2.30a}$$

$$E_z^1 = E_0 \sum_{n=-\infty}^{+\infty} (-j)^n b_n J_n(k_1\rho') e^{jn\phi'} + E_0 \sum_{n=-\infty}^{+\infty} (-j)^n c_n H_n^{(2)}(k_1\rho') e^{jn\phi'} \tag{2.30b}$$

$$E_z^2 = E_0 \sum_{n=-\infty}^{+\infty} (-j)^n d_n J_n(k_2\rho') e^{jn\phi'} \tag{2.30c}$$

Eqs. (2.30) hold in free space, inside cylinder '1' and inside cylinder '2', respectively.

Moreover, we have the following field expressions for azimuthal components [46]:

$$H_\phi^0 = \frac{E_0}{jZ_0} \sum_{n=-\infty}^{+\infty} (-j)^n J_n'(k_0\rho) e^{jn(\phi-\phi_0)} + \frac{E_0}{jZ_0} \sum_{n=-\infty}^{+\infty} (-j)^n a_n H'^{(2)}_n (k_0\rho) e^{jn(\phi-\phi_0)} \tag{2.31a}$$

$$H_\phi^1 = \frac{E_0}{jZ_1} \sum_{n=-\infty}^{+\infty} (-j)^n b_n J_n'(k_1\rho') e^{jn\phi'} + \frac{E_0}{jZ_1} \sum_{n=-\infty}^{+\infty} (-j)^n c_n H'^{(2)}_n (k_1\rho') e^{jn\phi'} \tag{2.31b}$$

$$H_\phi^2 = \frac{E_0}{jZ_2} \sum_{n=-\infty}^{+\infty} (-j)^n d_n J_n'(k_2\rho') e^{jn\phi'} \tag{2.31c}$$

Again, the coefficients $a_n,\ b_n,\ c_n$ and d_n can be determined by imposing the boundary condition of E and H field on the surfaces of '1' and '2'.

Once more, we rename the coefficients as shown in eq. (2.23). Next, to impose the boundary condition on the surface of cylinder '1', the fields $E_z^1(\rho',\phi')$ and $H_\phi^1(\rho',\phi')$ must be expressed in (ρ,ϕ) coordinates by resorting to the addition theorem for Hankel functions [46, 47]. Thus, by using the orthogonality of the exponential functions (which consists of multiplying each term by $e^{-jl\phi}$ and integrating between 0 and 2π, we have:

$$\begin{aligned} & j^{-l} J_l(k_0a_1) e^{-jl\phi_0} + o_{0,l} H_l^{(2)}(k_0a_1) e^{-jl\phi_0} \\ & \quad = \sum_{n=-\infty}^{+\infty} e^{-j(l-n)\bar{\phi}} J_{l-n}(k_1D) \left[i_{1,n} J_l(k_1a_1) + o_{1,n} H_l^{(2)}(k_1a_1) \right] \end{aligned} \tag{2.32a}$$

$$\begin{aligned} & \frac{1}{jZ_0} j^{-l} J_l'(k_0a_1) e^{-jl\phi_0} + \frac{1}{jZ_0} o_{0,l} H_l'^{(2)}(k_0a_1) e^{-jl\phi_0} \\ & \quad = \frac{1}{jZ_1} \sum_{n=-\infty}^{+\infty} e^{-j(l-n)\bar{\phi}} J_{l-n}(k_1D) \left[i_{1,n} J_l'(k_1a_1) + o_{1,n} H_l'^{(2)}(k_1a_1) \right] \end{aligned} \tag{2.32b}$$

Next, by proceeding with some algebraic manipulation, we obtain:

$$\begin{aligned} o_{0,l} = \frac{1}{H_l^{(2)}(k_0a_1)} \Bigg[- j^{-l} J_l(k_0a_1) + e^{jl\phi_0} \Big(\sum_{n=-\infty}^{+\infty} J_{l-n}(k_1D) \big[i_{1,n} J_l(k_1a_1) \\ + o_{1,n} H_l^{(2)}(k_1a_1) \big] \Big) e^{-j(l-n)\bar{\phi}} \Bigg] \end{aligned} \tag{2.33}$$

It should be noted that the values of $i_{2,n}$ and $o_{1,n}$ are similar to the concentric case calculated in eq. (2.27). Thus, using eqs. (2.33) and (2.26), $i_{1,n}$ can be solved:

$$\sum_{n=-\infty}^{+\infty} i_{1,n}\left[J_{l-n}(k_1 D)\left(\frac{J_l(k_1a_1)}{Z_0}\cdot\frac{H_l'^{(2)}(k_0a_1)}{H_l^{(2)}(k_0a_1)}-\frac{A}{B}\cdot\frac{H_l^{(2)}(k_1a_1)}{Z_0}\cdot\frac{H_l'^{(2)}(k_0a_1)}{H_l^{(2)}(k_0a_1)}-\frac{J_l'(k_1a_1)}{Z_1}\right.\right.$$
$$\left.\left.+\frac{A}{B}\cdot\frac{H_l'^{(2)}(k_1a_1)}{Z_1}\right)e^{-j(l-n)\bar{\phi}}\right]$$
$$=-j^{-l}\left[\frac{J_l'(k_0a_1)}{Z_0}-\frac{J_l(k_0a_1)}{Z_0}\cdot\frac{H_l'^{(2)}(k_0a_1)}{H_l^{(2)}(k_0a_1)}\right]e^{-jl\phi_0} \tag{2.34}$$

that, in compact notation becomes:

$$\sum_{n=-\infty}^{+\infty} i_{1,n}G_{l,n}=V_l \tag{2.35}$$

Eq. (2.35) represents a set of infinite equations which are transformed in a matrix form and then solved numerically after proper truncation to retrieve the proper coefficients $i_{1,n}$. Once we have $i_{1,n}$, we can go back to calculate all the other coefficients and consequently, the field can be determined in each region.

2.7 3-layer Stratified Concentric Cylinder

Next, we consider a 3-layer stratified concentric cylinder in free space illuminated by the plane wave of eq. (2.10). The three cylinders are concentric and are indicated as cylinder '1', cylinder '2', and cylinder '3', as shown in fig. 2.7.

Cylinders '1', '2' and '3' are characterised by ε_1, μ_1, ε_2, μ_2 and ε_3, μ_3, respectively, which can be complex and can vary with the frequency [see eq. (2.16)].

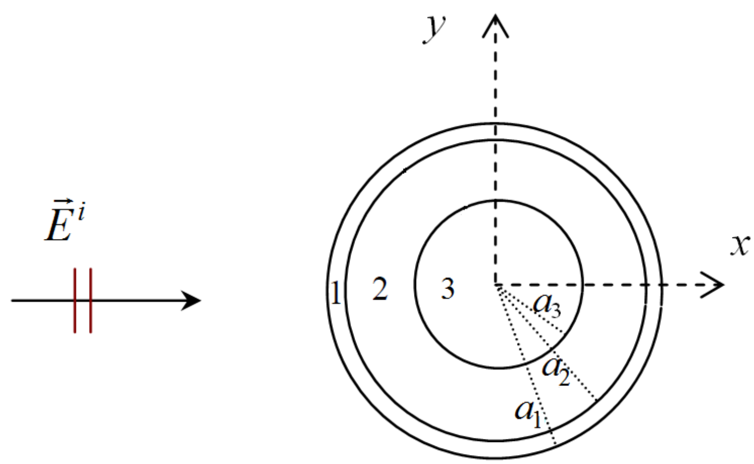

Figure 2.7: 3-layer stratified concentric cylinder in free space.

It holds:

$$k_3 = \sqrt{(2\pi f)^2 \varepsilon_3 \mu_3} \tag{2.36a}$$

$$Z_3 = \sqrt{\frac{\mu_3}{\varepsilon_3}} \tag{2.36b}$$

We proceed by writing the following equations, where ϕ_0 represents the angle of incidence of the plane wave:

$$E_z^0 = E_0 \sum_{n=-\infty}^{+\infty} (-j)^n J_n(k_0\rho) e^{jn(\phi-\phi_0)} + E_0 \sum_{n=-\infty}^{+\infty} (-j)^n a_n H_n^{(2)}(k_0\rho) e^{jn(\phi-\phi_0)} \tag{2.37a}$$

$$E_z^1 = E_0 \sum_{n=-\infty}^{+\infty} (-j)^n b_n J_n(k_1\rho) e^{jn\phi} + E_0 \sum_{n=-\infty}^{+\infty} (-j)^n c_n H_n^{(2)}(k_1\rho) e^{jn\phi} \tag{2.37b}$$

$$E_z^2 = E_0 \sum_{n=-\infty}^{+\infty} (-j)^n d_n J_n(k_2\rho) e^{jn\phi} + E_0 \sum_{n=-\infty}^{+\infty} (-j)^n e_n H_n^{(2)}(k_2\rho) e^{jn\phi} \tag{2.37c}$$

$$E_z^3 = E_0 \sum_{n=-\infty}^{+\infty} (-j)^n g_n J_n(k_3\rho) e^{jn\phi} \tag{2.37d}$$

Eqs. (2.37) are derived for free space, inside cylinder '1', cylinder '2' and cylinder '3', respectively. Moreover, we have:

$$H_\phi^0 = \frac{E_0}{jZ_0}\sum_{n=-\infty}^{+\infty}(-j)^n J_n'(k_0\rho)e^{jn(\phi-\phi_0)} + \frac{E_0}{jZ_0}\sum_{n=-\infty}^{+\infty}(-j)^n a_n H_n^{'(2)}(k_0\rho)e^{jn(\phi-\phi_0)} \tag{2.38a}$$

$$H_\phi^1 = \frac{E_0}{jZ_1}\sum_{n=-\infty}^{+\infty}(-j)^n b_n J_n'(k_1\rho)e^{jn\phi} + \frac{E_0}{jZ_1}\sum_{n=-\infty}^{+\infty}(-j)^n c_n H_n^{'(2)}(k_1\rho)e^{jn\phi} \tag{2.38b}$$

$$H_\phi^2 = \frac{E_0}{jZ_2}\sum_{n=-\infty}^{+\infty}(-j)^n d_n J_n'(k_2\rho)e^{jn\phi} + \frac{E_0}{jZ_2}\sum_{n=-\infty}^{+\infty}(-j)^n e_n H_n^{'(2)}(k_2\rho)e^{jn\phi} \tag{2.38c}$$

$$H_\phi^3 = \frac{E_0}{jZ_3}\sum_{n=-\infty}^{+\infty}(-j)^n g_n J_n'(k_3\rho)e^{jn\phi} \tag{2.38d}$$

Again, eqs. (2.38) are derived for free space, inside cylinder '1', cylinder '2' and cylinder '3', respectively. All the coefficients can be determined by imposing the boundary conditions of E and H on the surfaces of '1', '2' and '3'; thus, the field can be determined in each region.

The procedure can be iterated if an n-layer stratified concentric cylinder is considered.

2.8 3-layer Stratified Eccentric Cylinder

Here, we consider a 3-layer stratified eccentric cylinder in free space, illuminated by a plane wave. The three cylinders are indicated as cylinder '1', cylinder '2' and cylinder '3', and have radii a_1, a_2 and a_3 respectively (see fig. 2.8).

Cylinder '1' is characterised by ε_1,μ_1, cylinder '2' is characterised by ε_2,μ_2 and cylinder '3' is characterised by ε_3,μ_3.

To determine the field in different regions, we start by writing the field expressions for axial components, where ϕ_0 represents the angle of incidence of the plane wave:

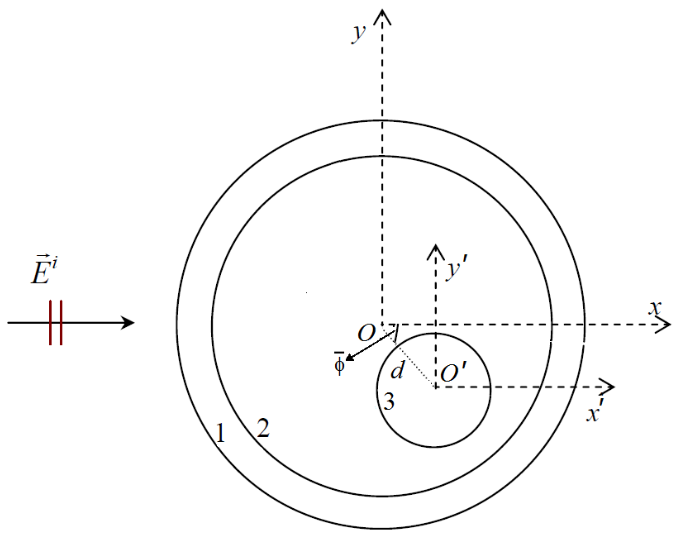

Figure 2.8: 3-layer stratified eccentric cylinder in free space.

$$E_z^0 = E_0 \sum_{n=-\infty}^{+\infty} (-j)^n [J_n(k_0\rho) + o_{0,n} H_n^{(2)}(k_0\rho)] e^{jn(\phi-\phi_0)}, \quad \rho > a_1 \tag{2.39a}$$

$$E_z^1 = E_0 \sum_{n=-\infty}^{+\infty} (-j)^n [i_{1,n} J_n(k_1\rho) + o_{1,n} H_n^{(2)}(k_1\rho)] e^{jn\phi}, \quad a_2 < \rho < a_1 \tag{2.39b}$$

$$E_z^2 = E_0 \sum_{n=-\infty}^{+\infty} (-j)^n [i_{2,n} J_n(k_2\rho') + o_{2,n} H_n^{(2)}(k_2\rho')] e^{jn\phi'}, \quad \rho < a_2 \text{ and } \rho' > a_3 \tag{2.39c}$$

$$E_z^3 = E_0 \sum_{n=-\infty}^{+\infty} (-j)^n i_{3,n} J_n(k_3\rho') e^{jn\phi'}, \qquad \rho' < a_3 \tag{2.39d}$$

Eqs. (2.39) are derived for free space, inside cylinder '1', inside cylinder '2' and inside cylinder '3', respectively. Similarly we derive the following field expressions for azimuthal components:

$$H_{\phi}^{0} = \frac{E_0}{jZ_0}\sum_{n=-\infty}^{+\infty}(-j)^n[J_n'(k_0\rho)+o_{0,n}H'^{(2)}_n(k_0\rho)]e^{jn(\phi-\phi_0)}, \quad \rho > a_1 \tag{2.40a}$$

$$H_{\phi}^{1} = \frac{E_0}{jZ_1}\sum_{n=-\infty}^{+\infty}(-j)^n[i_{1,n}J'_n(k_1\rho)+o_{1,n}H'^{(2)}_n(k_1\rho)]e^{jn\phi}, \quad a_2 < \rho < a_1 \tag{2.40b}$$

$$H_{\phi'}^{2} = \frac{E_0}{jZ_2}\sum_{n=-\infty}^{+\infty}(-j)^n[i_{2,n}J'_n(k_2\rho')+o_{2,n}H'^{(2)}_n(k_2\rho')]e^{jn\phi'}, \quad \rho < a_2 \text{ and } \rho' > a_3 \tag{2.40c}$$

$$H_{\phi'}^{3} = \frac{E_0}{jZ_3}\sum_{n=-\infty}^{+\infty}(-j)^n i_{3,n}J_n'(k_3\rho')e^{jn\phi'}, \quad \rho' < a_3 \tag{2.40d}$$

By applying the boundary condition at $\rho = a_1$ we have:

$$E_z^0(\rho=a_1) = E_z^1(\rho=a_1) \;\Rightarrow$$
$$[J_n(k_0a_1)+o_{0,n}H_n^{(2)}(k_0a_1)]e^{-jn\phi_0} = i_{1,n}J_n(k_1a_1)+o_{1,n}H_n^{(2)}(k_1a_1) \tag{2.41a}$$

$$H_{\phi}^0(\rho=a_1) = H_{\phi}^1(\rho=a_1) \;\Rightarrow$$
$$[J_n'(k_0a_1)+o_{0,n}H'^{(2)}_n(k_0a_1)]e^{-jn\phi_0} = \frac{Z_0}{Z_1}[i_{1,n}J_n'(k_1a_1)+o_{1,n}H'^{(2)}_n(k_1a_1)] \tag{2.41b}$$

From eqs. (2.41a) and (2.41b),

$$i_{1,n} = R_n + o_{0,n} S_n \tag{2.42a}$$

$$o_{1,n} = \overline{R}_n + o_{0,n} \overline{S}_n \tag{2.42b}$$

where

$$R_n = \frac{\pi k_1 a_1 e^{-jn\phi_0}}{j2}\left[J_n(k_0a_1){H'}^{(2)}_n(k_1a_1) - \frac{Z_1}{Z_0}H^{(2)}_n(k_1a_1)J'_n(k_0a_1)\right] \tag{2.43a}$$

$$S_n = \frac{\pi k_1 a_1 e^{-jn\phi_0}}{j2}\left[H^{(2)}_n(k_0a_1){H'}^{(2)}_n(k_1a_1) - \frac{Z_1}{Z_0}H^{(2)}_n(k_1a_1){H'}^{(2)}_n(k_0a_1)\right] \tag{2.43b}$$

$$\overline{R}_n = -\frac{\pi k_1 a_1 e^{-jn\phi_0}}{j2}\left[J_n(k_0a_1)J'_n(k_1a_1) - \frac{Z_1}{Z_0}J_n(k_1a_1)J'_n(k_0a_1)\right] \tag{2.43c}$$

$$\overline{S}_n = -\frac{\pi k_1 a_1 e^{-jn\phi_0}}{j2}\left[H^{(2)}_n(k_0a_1)J'_n(k_1a_1) - \frac{Z_1}{Z_0}J_n(k_1a_1){H'}^{(2)}_n(k_0a_1)\right] \tag{2.43d}$$

Next, applying the boundary condition at $\rho' = a_3$ we have:

$$E_z^2(\rho' = a_3) = E_z^3(\rho' = a_3) \;\;\Rightarrow\;\; i_{2,n}J_n(k_2a_3) + o_{2,n}H^{(2)}_n(k_2a_3) = i_{3,n}J_n(k_3a_3) \tag{2.44a}$$

$$H_{\phi'}^2(\rho' = a_3) = H_{\phi'}^3(\rho' = a_3) \;\;\Rightarrow\;\; i_{2,n}J'_n(k_2a_3) + o_{2,n}{H'}^{(2)}_n(k_2a_3) = \frac{Z_2}{Z_3}i_{3,n}J'_n(k_3a_3) \tag{2.44b}$$

From eqs. (2.44a) and (2.44b),

$$o_{2,n} = -i_{2,n}Q_n \tag{2.45}$$

with

$$Q_n = \frac{J_n(k_2a_3)J'_n(k_3a_3) - (Z_3/Z_2)J'_n(k_2a_3)J_n(k_3a_3)}{H^{(2)}_n(k_2a_3)J'_n(k_3a_3) - (Z_3/Z_2){H'}^{(2)}_n(k_2a_3)J_n(k_3a_3)} \tag{2.46}$$

To facilitate the imposition of boundary conditions at $\rho = a_2$, E_z^2 and $H_{\phi'}^2$ are first expressed in terms of ρ and ϕ:

$$\begin{aligned}E_z^2 =&E_0 \sum_{n=-\infty}^{+\infty} (-j)^n [i_{2,n} \sum_{m=-\infty}^{+\infty} J_{m-n}(k_2 d) J_m(k_2\rho) e^{jm\phi} e^{-j(m-n)\bar{\phi}} \\ &+ o_{2,n} \sum_{m=-\infty}^{+\infty} H_m^{(2)}(k_2\rho) J_{m-n}(k_2 d) e^{jm\phi} e^{-j(m-n)\bar{\phi}}], \\ &\qquad\qquad\qquad \rho < a_2 \text{ and } \rho' > a_3\end{aligned} \tag{2.47a}$$

$$\begin{aligned}H_{\phi'}^2 =&\frac{E_0}{jZ_2} \sum_{n=-\infty}^{+\infty} (-j)^n E_0 [i_{2,n} \sum_{m=-\infty}^{+\infty} J_{m-n}(k_2 d) J'_m(k_2\rho) e^{jm\phi} e^{-j(m-n)\bar{\phi}} \\ &+ o_{2,n} \sum_{m=-\infty}^{+\infty} H'^{(2)}_m(k_2\rho) J_{m-n}(k_2 d) e^{jm\phi} e^{-j(m-n)\bar{\phi}}], \\ &\qquad\qquad\qquad \rho < a_2 \text{ and } \rho^{'} > a_3\end{aligned} \tag{2.47b}$$

In above, d and $\bar{\phi}$ represent the distance between the axes of cylinders '2' and '3' (OO'), and the angle between OO' and the x-axis, respectively.

Moving on to the boundary condition at $\rho = a_2$, we have:

$$\begin{aligned}&E_z^1(\rho = a_2) = E_z^2(\rho = a_2) \;\; \Rightarrow \\ &\sum_{n=-\infty}^{+\infty} (-j)^n [i_{1,n} J_n(k_1 a_2) + o_{1,n} H_n^{(2)}(k_1 a_2)] e^{jn\phi} \\ &= \sum_{n=-\infty}^{+\infty} (-j)^n [i_{2,n} \sum_{m=-\infty}^{+\infty} J_{m-n}(k_2 d) J_m(k_2 a_2) e^{jm\phi} e^{-j(m-n)\bar{\phi}} \\ &\quad + o_{2,n} \sum_{m=-\infty}^{+\infty} H_m^{(2)}(k_2 a_2) J_{m-n}(k_2 d) e^{jm\phi} e^{-j(m-n)\bar{\phi}}]\end{aligned} \tag{2.48a}$$

$$H^1_\phi(\rho=a_2)=H^2_\phi(\rho=a_2) \quad \Rightarrow$$
$$\sum_{n=-\infty}^{+\infty}(-j)^n[i_{1,n}J'_n(k_1a_2)+o_{1,n}H'^{(2)}_n(k_1a_2)]e^{jn\phi}$$
$$=\frac{Z_1}{Z_2}\sum_{n=-\infty}^{+\infty}(-j)^n[i_{2,n}\sum_{m=-\infty}^{+\infty}J_{m-n}(k_2d)J'_m(k_2a_2)e^{jm\phi}e^{-j(m-n)\overline{\phi}}$$
$$+o_{2,n}\sum_{m=-\infty}^{+\infty}H'^{(2)}_m(k_2a_2)J_{m-n}(k_2d)e^{jm\phi}e^{-j(m-n)\overline{\phi}}] \tag{2.48b}$$

Employing the orthogonality property of $e^{-jl\phi}$ ($\int_0^{2\pi}e^{-jl\phi}e^{jm\phi}d\phi=2\pi$ if $l=m$ and equals to 0 if $l\neq m$), yields:

$$(-j)^l[i_{1,l}J_l(k_1a_2)+o_{1,l}H^{(2)}_l(k_1a_2)]$$
$$=\sum_{n=-\infty}^{+\infty}(-j)^n e^{-j(l-n)\overline{\phi}}i_{2,n}[J_{l-n}(k_2d)J_l(k_2a_2)-Q_nH^{(2)}_l(k_2a_2)J_{l-n}(k_2d)] \tag{2.49a}$$
$$(-j)^l[i_{1,l}J'_l(k_1a_2)+o_{1,l}H'^{(2)}_l(k_1a_2)]$$
$$=\frac{Z_1}{Z_2}\sum_{n=-\infty}^{+\infty}(-j)^n e^{-j(l-n)\overline{\phi}}i_{2,n}[J_{l-n}(k_2d)J'_l(k_2a_2)-Q_nH'^{(2)}_l(k_2a_2)J_{l-n}(k_2d)] \tag{2.49b}$$

Substituting for $i_{1,l}$ and $o_{1,l}$ from eqs. (2.42a) and (2.42b), results in:

$$(-j)^l\left[[R_lJ_l(k_1a_2)+\overline{R_l}H^{(2)}_l(k_1a_2)]+o_{0,l}[S_lJ_l(k_1a_2)+\overline{S_l}H^{(2)}_l(k_1a_2)]\right]$$
$$=\sum_{n=-\infty}^{+\infty}(-j)^n e^{-j(l-n)\overline{\phi}}i_{2,n}[J_{l-n}(k_2d)J_l(k_2a_2)-Q_nH^{(2)}_l(k_2a_2)J_{l-n}(k_2d)] \tag{2.50a}$$

$$(-j)^l\left[[R_lJ'_l(k_1a_2)+\overline{R_l}H'^{(2)}_l(k_1a_2)]+o_{0,l}[S_lJ'_l(k_1a_2)+\overline{S_l}H'^{(2)}_l(k_1a_2)]\right]$$
$$=\frac{Z_1}{Z_2}\sum_{n=-\infty}^{+\infty}(-j)^n e^{-j(l-n)\overline{\phi}}i_{2,n}[J_{l-n}(k_2d)J'_l(k_2a_2)-Q_nH'^{(2)}_l(k_2a_2)J_{l-n}(k_2d)] \tag{2.50b}$$

Eliminating $o_{0,l}$ from eqs. (2.50a) and (2.50b), the following result is obtained,

$$\sum_{n=-\infty}^{+\infty}i_{2,n}G_{l,n}=V_l \tag{2.51}$$

where

$$
\begin{aligned}
V_l &= (-j)^l \Big[[R_l J_l(k_1a_2) + \overline{R_l} H_l^{(2)}(k_1a_2)][S_l J_l'(k_1a_2) + \overline{S_l} H'^{(2)}_l(k_1a_2)] \\
&\quad - [R_l J_l'(k_1a_2) + \overline{R_l} H'^{(2)}_l(k_1a_2)][S_l J_l(k_1a_2) + \overline{S_l} H_l^{(2)}(k_1a_2)] \Big]
\end{aligned} \tag{2.52a}
$$

and

$$
\begin{aligned}
G_{l,n} = \Big[& [S_l J_l'(k_1a_2) + \overline{S_l} H'^{(2)}_l(k_1a_2)][J_{l-n}(k_2d) J_l(k_2a_2) \\
& - Q_n H_l^{(2)}(k_2a_2) J_{l-n}(k_2d)] - (\frac{Z_1}{Z_2})[S_l J_l(k_1a_2) \\
& + \overline{S_l} H_l^{(2)}(k_1a_2)][J_{l-n}(k_2d) J_l'(k_2a_2) \\
& - Q_n H'^{(2)}_l(k_2a_2) J_{l-n}(k_2d)] \Big] (-j)^n e^{-j(l-n)\overline{\phi}}
\end{aligned} \tag{2.52b}
$$

Thus, all inward and outward fields, and hence the field everywhere inside the stratified cylinder have been calculated. The procedure can be easily iterated if more layers are considered. It should be noted that if the cylinder in fig. 2.8 is illuminated by an electrical z-directed line source of intensity *I*, then all the expressions in this section which have been derived from the plane wave illumination can still be used by simply replacing $(-j)^n$ with $H_n^{(2)}(k_0\rho_0)$, where ρ_0 represents the distance of the line source from the axis of the cylinder.

2.9 UWB Pulse

The previous equations hold for each frequency of the plane wave. Let us now consider a UWB pulse *u(t)* associated with the $\overrightarrow{E}^i$ of eq. (2.10). It is evident that:

$$
U(f) = \int_{-\infty}^{+\infty} u(t) e^{-j2\pi ft} dt \tag{2.53}
$$

$$
u(t) = \int_{-\infty}^{+\infty} U(f) e^{j2\pi ft} df \tag{2.54}
$$

By sampling the spectrum of $U(f)$ over its band B at the frequencies $[f_1,...,f_{nf}]$, we can write:

$$u(t) = \Delta f \sum_{k=1}^{nf} U(f_k) e^{j2\pi f_k t} \tag{2.55}$$

The samples of the spectrum $R(f_k,u)$ of the received signal at a given point u are expressed as:

$$R(f_k,u) = U(f_k)H(f_k,u) \tag{2.56}$$

The samples of the frequency response $H(f_k,u)$ can be determined by employing the previous equations, after setting $f = f_k$ and expressing the point u in the appropriate cylindrical coordinates. Then, an inverse discrete Fourier transform (IDFT) provides the sampled version of the impulse response $h(t,u)$ and the received signal $r(t,u)$:

$$h(t,u) = \mathrm{IDFT}\{H(f,u)\} \tag{2.57}$$

$$r(t,u) = \mathrm{IDFT}\{U(f)H(f,u)\} \tag{2.58}$$

Note that $h(t,u),\ r(t,u) \in R$ if a bilateral spectral interval is assumed.

2.10 UWB Channel Modelling of Human Body

Stratified cylinder configurations can be used as a starting point to model the human body. In this context, we will analyse the problem of UWB BAN channel modelling as following:

1. We construct a stratified cylinder model by using the required number of layers and consistent dielectric parameters.
2. We calculate the spectrum of the UWB signal.
3. For each frequency component (sample) we derive the analytical solution by resorting to the previous sections.
4. The set of solutions is collected and transformed into the time domain (IDFT).

5. The required channel parameters are derived.

A key point to address is using the dielectric parameters which correctly represent human tissues. The interaction between microwave frequency ($\sim 1-40$GHz) electromagnetic signals and most materials is governed by two parameters, the material's complex dielectric permittivity ($\varepsilon_r = \varepsilon' - j\varepsilon''$) and its conductivity σ (assuming the material is not magnetic). The components of the dielectric permittivity are functions of frequency, its real part ε' decreases monotonically from a stationary value at low frequencies towards low values at high frequencies. This behaviour can be seen in literature [26, 48]; specifically, in [48] it is pointed out that in frequencies below 100 Hz the relative permittivity of a tissue could reach up to 10^7, while its value decreases at high frequencies through three main steps known as the α, β, and γ dispersions. On the other hand, the imaginary component ε'' reveals two major contributions; at low frequencies this "loss" term is dominated by bulk conduction (and hence σ) effects and at higher frequencies (>10GHz) dipolar rotational excitations introduce distinct peaks. This means that the majority of the effects a tissue has on the propagation of electromagnetic waves, arises from ε' and the conductivity σ.

Many measurement campaigns have been conducted to determine the dielectric properties of biological tissues [48]. The dielectric constant and conductivity values from a selection of tissues at different frequencies are presented in tables 2.1 and 2.2, respectively. Meanwhile table 2.3 lists the dielectric constant and conductivity values for a variety of different tissues at a frequency of 5 GHz. The data for all three tables were extracted from [48]. The measured data can be extrapolated to all the frequencies using the Debye model [26].

$$\varepsilon_{eq}^{\text{Debye}}(f) = \varepsilon_\infty - j\frac{\sigma_s}{2\pi f \varepsilon_0} + \frac{\varepsilon_s - \varepsilon_\infty}{1 + j2\pi f \tau} \tag{2.59}$$

Referring to the above equation, for each tissue the parameters ε_∞ (permittivity at high frequency limit), ε_s (static permittivity), σ_s (static conductivity) and τ (relaxation time) are chosen in order to match the measured dielectric constant and the conductivity. Thus, each tissue will be characterised by its equivalent dielectric constant $\varepsilon_{eq}^{\text{Debye}}$. It follows that the proposed model adequately takes into account the frequency-dependence of human tissues.

Table 2.1: Dielectric constant ($\varepsilon_{eq}^{\text{Debye}}$) of a selection of tissues for different frequencies [48].

Frequency	Skin (dry)	Average muscle	Fat (Mean)	Cancellous Bone	Cortical Bone
0.1 GHz	45	60	11	25	15
1 GHz	40.94	55.74	11.29	20.58	12.36
2 GHz	38.57	54.17	10.96	19.09	11.65
3 GHz	37.45	52.85	10.66	17.94	11.07
4 GHz	36.59	51.52	10.36	16.95	10.53
5 GHz	35.77	50.13	10.08	16.05	10.04
6 GHz	34.95	48.70	9.80	15.24	9.56

Table 2.2: Conductivity of a selection of tissues for different frequencies [48].

Frequency	Skin (dry)	Average muscle	Fat (Mean)	Cancellous Bone	Cortical Bone
0.1 GHz	0.8	0.8	0.07	0.2	0.1
1 GHz	0.90	1.01	0.12	0.36	0.16
2 GHz	1.27	1.51	0.21	0.65	0.31
3 GHz	1.74	2.24	0.34	1.00	0.51
4 GHz	2.34	3.16	0.50	1.40	0.73
5 GHz	3.06	4.24	0.68	1.81	0.96
6 GHz	3.89	5.45	0.87	2.23	1.20

Table 2.3: Dielectric constant and conductivity from a large variety of tissue at the frequency of 5 GHz [48].

Tissue	**Epsilon** (ε)	**Sigma** (σ)
Bladder	16.67	1.53
Blood	53.95	5.39
Bone (Cancellous)	16.05	1.81
Bone (Cortical)	10.04	0.96
Bone (Marrow Infiltrated)	9.05	0.98
Breast fat	4.65	0.35
Cartilage	33.63	4.09
Cerebellum	41.05	4.19
Cerebrospinal fluid	61.95	6.60
Colon (large intestine)	49.72	4.58
Cornea	47.73	4.72
Dura	38.86	3.58
Eye tissue	49.0	4.5
Fat	5.03	0.24
Fat (average)	10.08	0.68
Gall bladder	54.76	4.65
Heart	50.27	4.86
Kidney	48.06	4.94
Liver	39.26	3.83
Lung (Inflated)	18.97	1.72
Lung (Deflated)	44.86	3.94
Nerve (Spinal chord)	27.89	2.43
Ovary	39.96	4.48
Skin (Dry)	35.77	3.06
Skin (Wet)	39.61	3.57

2.11 UWB Channel Modelling of Human Body: Numerical Example

Let us consider a 3-layer stratified cylinder in free space. We assume that cylinder '1' ($a_1 = 0.15$ m) is made of dry skin; cylinder '2' ($a_2 = 0.149$ m) is made of fat, and cylinder '3' ($a_3 = 0.02$ m) is made of cortical bone. It has to be highlighted that each tissue is characterised by its own equivalent dielectric constant $\varepsilon_{eq}^{\text{Debye}}$, calculated as shown in the previous section.

The cylinder (fig. 2.9) is illuminated by an electrical z-directed line source of intensity I positioned at (ρ_0, ϕ_0). It can be shown that the field radiated by the line source is expressed as

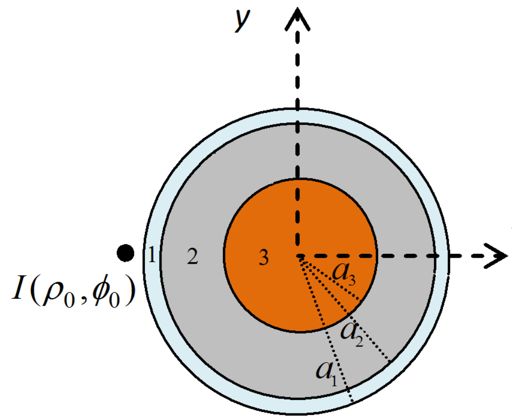

Figure 2.9: 3-layer stratified concentric cylinder in free space illuminated by an electrical z-directed line source; cylinder '1' is made of dry skin, cylinder '2' is made of fat, and cylinder '3' is made of cortical bone.

[45, 49]:

$$E_z^i = -\frac{k_0^2 I}{8\pi f \varepsilon_0} \sum_{n=-\infty}^{+\infty} H_n^{(2)}(k_0\rho_0) e^{jn(\phi-\phi_0)} \tag{2.60}$$

Thus, it follows that all the expressions of the previous sections which have been derived from plane wave illumination can still be used by simply replacing $(-j)^n$ with $H_n^{(2)}(k_0\rho_0)$.

We assume that the pulse $u(t) = \sqrt{2\pi e}\frac{t}{\tau} e^{-\pi(\frac{t}{\tau})^2}$ is associated to the line source. When $\tau = 0.14$ ns we have the pulse given in fig. 2.10 and the spectrum in fig. 2.11.

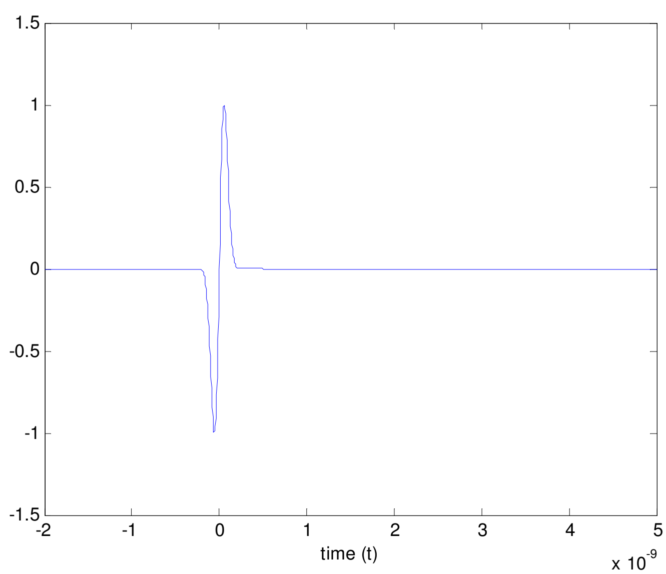

Figure 2.10: Amplitude of the transmitted pulse (time-domain).

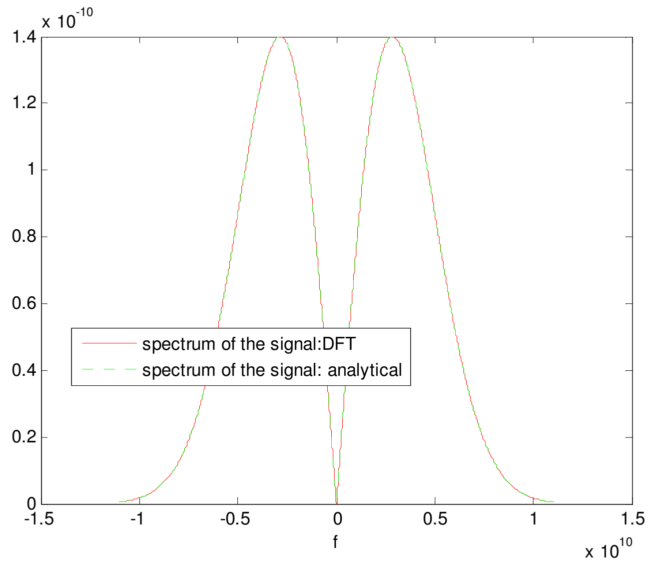

Figure 2.11: Amplitude of the spectrum of transmitted pulse (frequency-domain): the continuous line refers to a discrete Fourier transform (DFT) approach, while the dotted lines represents the analytical Fourier Transform.

Figure 2.12 shows the path loss of the impulse when assuming the line source positioned at $(\rho_0 = 0.016, \phi_0 = \pi)$ and moving along the circumstance having radius equal to ρ_0; a frequency sampling of $\Delta f = 10$ has been used. The path loss is shown in dB relative to the loss at a reference distance of 0.01 m; the distance has to be intended to represent the distance around the body. It is useful to point out that, when determining the path loss, the received signal is intended as the total received signal, i.e. it comprises both the incident and scattering components.

Figure 2.13 depicts the path loss for different frequency components. From the figure, it is possible to see that the decay increases with frequency. Moreover, all the curves tend to flatten out on the opposite side of the cylinder (note that half diameter is approximately 0.502 m). This behaviour is presumably due to the clockwise and counter-clockwise diffracting waves interfacing with each other on the opposite sides of the cylinder. The same conclusion can be found in [50], where a homogeneous lossy cylinder model has been used. A representation of the path loss with respect to the distance and frequency is given in fig. 2.14.

Finally, fig. 2.15 shows the normalised pulse received in the forward direction. From

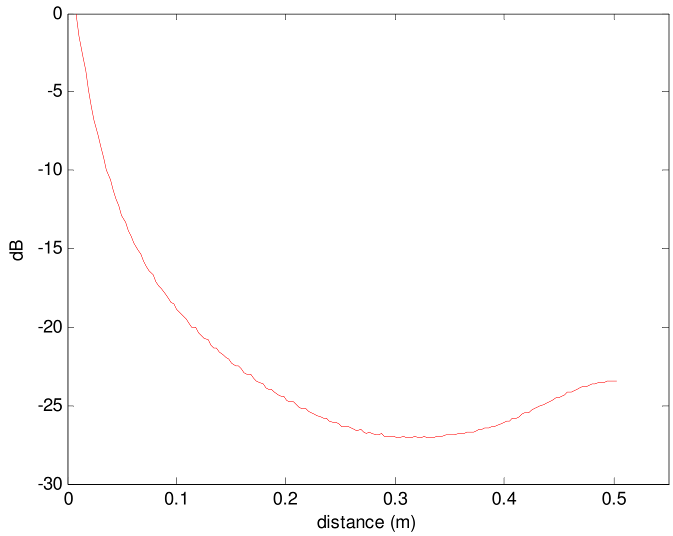

Figure 2.12: Path loss of the impulse when assuming the line source positioned at $(\rho_0 = 0.016, \phi_0 = \pi)$ and moving along the circumference having radius $\phi_0 = 0.016$.

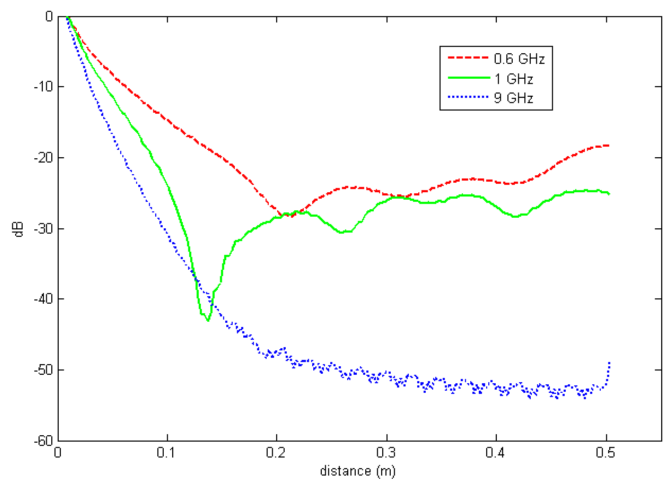

Figure 2.13: Path loss for different frequency components when assuming the line source positioned at $(\rho_0 = 0.016, \phi_0 = \pi)$ and moving along the circumference having radius $\phi_0 = 0.016$.

this figure, it is possible to note how the pulse has been distorted by the frequency-dependent effects of human tissues. The knowledge (even approximated) of the received pulse can be of vital importance for this design of the communication link [51]. Again, it can be useful to note that fig. 2.15 refers to the total received signal, i.e. it comprises both incident and scattering components.

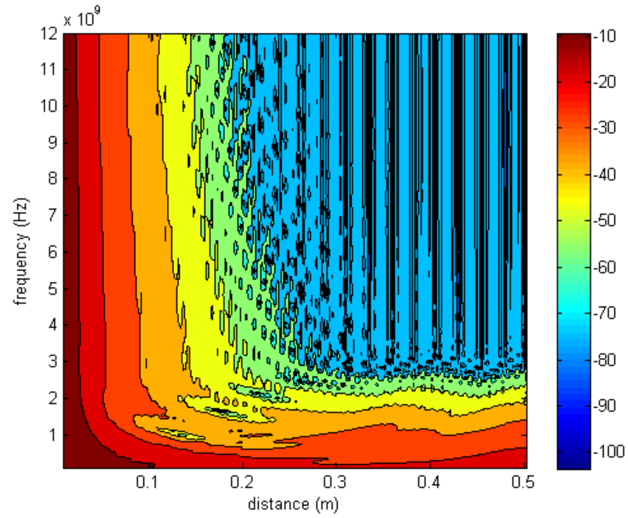

Figure 2.14: Path loss with respect to the distance and frequency when assuming the line source positioned at $(\rho_0 = 0.016, \phi_0 = \pi)$ and moving along the circumference having radius $\phi_0 = 0.016$.

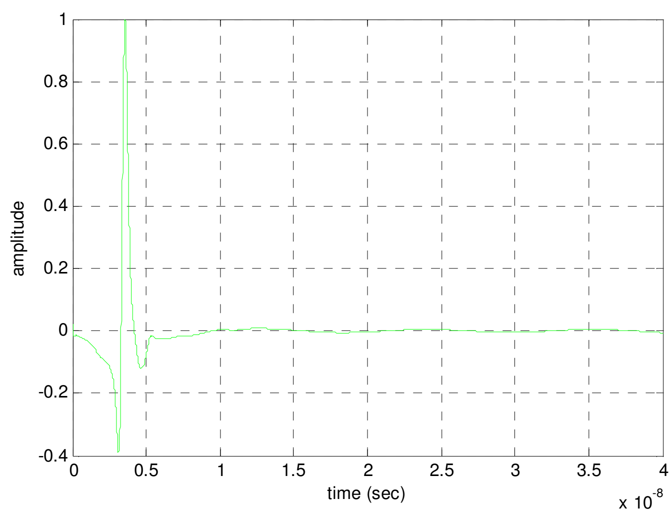

Figure 2.15: Normalised received pulse.

2.12 Validation of the Procedure Through Measurements

To assess the validity of the proposed method a comparison with measurement is presented. Specifically, a multilayered human tissue like phantom was constructed. To achieve this purpose, a 2 mm thick Polyvinyl chloride (PVC) cylindrical pipe with radius of 5 cm and height of 30 cm was concentrically placed inside a larger PVC cylindrical pipe, also 2 mm thick and 30 cm tall, but with a larger radius of 6.25 cm. Both pipes (having dielectric constant of 2.6

and negligible conductivity) were filled with Agar-Agar gel approximating high water-content human tissues. Although the thickness of the pipes was chosen to be as narrow as possible, their minimal effect could not be ignored, making this model effectively a 4-layer problem [see fig. 2.16(a)]. The Agar-Agar was dissolved in hot water at approximately 95°C and then cooled to room temperature to form a semitransparent gel. For all measurements performed throughout this thesis, a concentration of approximately 6% (15g per 250g) was used. The dielectric constant and the conductivity are functions of the concentration of the Agar-Agar [52]; for this experiment two distinct concentrations of Agar-Agar were used. The external plastic pipe was filled with a lower conductive Agar-Agar (σ =0.5), while the smaller plastic pipe was filled with a higher conductive Agar-Agar (σ =2). This increase in conductivity value can be gained by adding the necessary amount of salt to the original Agar-Agar mixture; the approximate relationship between the salt concentration and the Agar-Agar's conductivity was first given by eq. (2.61) [53], and later improved in [54], as represented in eq. (2.62):

$$\sigma(\mathrm{S/m}) = 200 \times \frac{\text{grams of NaCl}}{\text{solution volume (mL)}} \tag{2.61}$$

$$\sigma(\mathrm{S/m}) = 215 \times \frac{\text{grams of NaCl}}{\text{solution volume (mL)}} + 0.0529 \tag{2.62}$$

For all measurements performed in this thesis, the relationship stated in eq. (2.61) has been used to adjust the conductivity of the Agar-Agar. Meanwhile, the change in the dielectric constant value was insignificant [52] and was assumed to be equal to 70 for both Agar-Agar solutions. By comparing these values with those given in [48], it can be noted that the dielectric constant and the conductivity of Agar-Agar can be used to simulate the actual dielectric properties of human tissues. Frequency-domain UWB measurement in an anechoic chamber was performed, using a vector network analyser (VNA) arrangement to obtain the transfer function (frequency response) at 1601 discrete frequencies in the band of 3.5-8 GHz. Throughout this thesis, two different types of antennas have been used in the measurements. Wideband bow-tie antennas have been used in the more basic 2D measurements; while for 3D measurements and more complex 2D measurements wideband discone antennas were employed. The use of two different antennas would also allow for showcasing the robustness of the reconstruction algorithm for different UWB designed antennas.

For this experiment, Wideband discone antennas, vertically polarised and omni-directional in the azimuth plane were used (after checking that the S_{11} is lower than -10 dB in the band of interest). A careful adjustment was done for both antennas to be in vertical position to avoid any polarisation mismatch. The location of the transmitting antenna was fixed at approximately 20 cm away from the centre of the cylinder, while the receiver antenna was positioned close to the external surface of the cylinder at the opposite side of the cylinder. Both antennas were placed at the same height (approximately half of the height of the cylinder).

The measured frequency response $H(f)$ is given in 2.16(b), shown with continuous line. In the same figure, the $H(f)$ calculated analytically by using the approach presented in this chapter is also plotted (dotted lines), showing a good agreement with the measurements [55].

It is worthwhile to point out that, to allow comparison with measurements, the transmitter reflection coefficient (S_{11}) of the discone antennas had to be included in the analytical procedure.

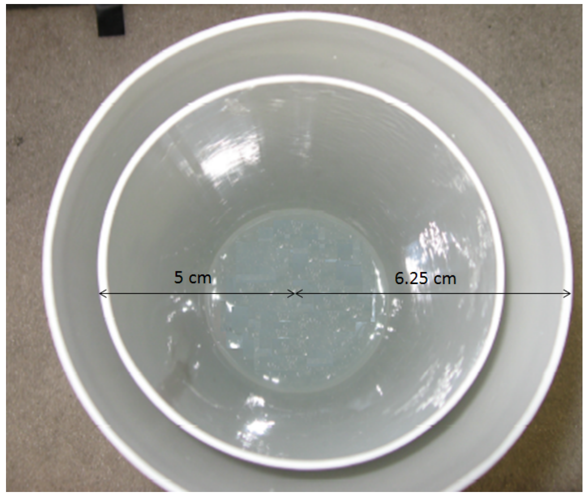

(a)

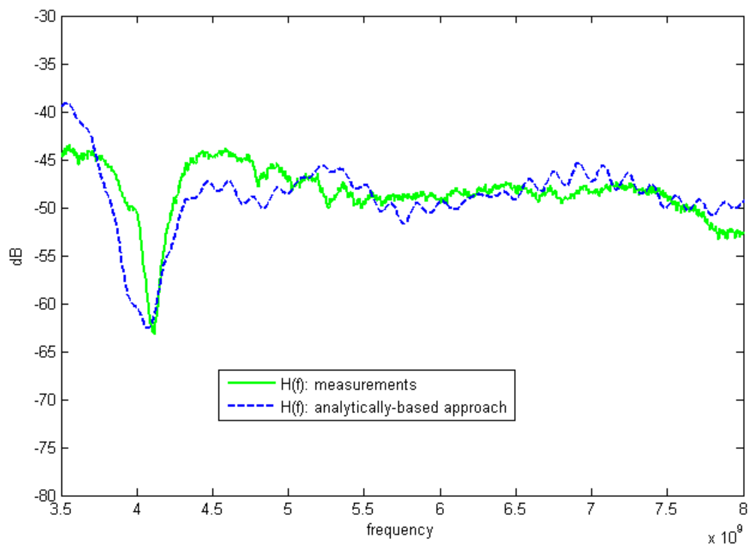

(b)

Figure 2.16: (a) 4-layer human tissue-like phantom, (b) Comparison between the frequency response calculated analytically (blue) and the one achieved using measurements (green).

2.13 Summary

The proposed approach uses an analytical process based on the exact Maxwell's equation solution for stratified cylinders. The model assumes the body can be approximated as a stratified multilayered infinite cylinder. Each layer represents a human tissues, and is characterised by the consistent equivalent dielectric constant $\varepsilon_{eq}^{\text{Debye}}$. It follows that the model adequately takes into account the frequency-dependence of human tissues. Moreover, the stratified multilayered infinite cylinder can represent a reasonable approximation of a human body allowing us to take into account many propagation phenomena, including diffraction around a curved lossy surface, reflections off the body, multi-reflection between different tissues and penetration. All of these effects are expected to play a role in BAN propagation, though the relative importance of each effect will depend on such factors as the frequency, polarity, radius of curvature, and tissue properties.

The modelling approach proposed in this chapter is very generic and we can postulate several future uses and extensions. Examples include sensors to observe brain activity for recording or warning against seizure events, to examine heart activity for diagnosis and automatic emergency calls, to measure glucose levels in diabetic patients, and to monitor oxygen, blood pressure, or disease markers. For all these systems, channel parameters such as frequency dispersion and path loss trends can be investigated. The approach is computationally faster than FDTD, clearly at the cost of a simplified body model. For the example presented in section 2.11, the execution time is less than 10 minutes in an Intel Pentium M 2 GHz with 1 GB RAM. It follows that the model is suited not only for providing a physical insight into the BAN propagation phenomena, but also to be used in Monte-Carlo approaches for deriving communication statistics. In the next chapter, the first proposed imaging algorithm, which is based on the MM of Bessel functions, will be introduced.

3

Proposed Imaging Technique I: Mode-Matching Bessel-Functions-Based Procedure

3.1 Introduction

First of the two proposed methods based on UWB microwave signals is described and investigated in this chapter. Specifically, a procedure based on the mode-matching (MM) [56, 57] of Bessel functions is introduced, which enables the identification of the presence and location of significant scatterers inside cylindrically-shaped volumes [58]. Using the MM procedure leads to the generation/inversion of a rather small matrix. Together with its simplicity, the methodology permits the capture of contrast, to the extent in which different media can be discriminated in the final image. Potential applications of the proposed method would be breast cancer detection and internal organ imaging.

In the first section, a complete analytical explanation of the MM procedure is formulated, while in the last two sections the validation of the method through a number of simulations and measurements involving cylindrical shapes with inclusions is performed.

3.2 Mode-Matching Bessel-Function-Based Procedure

3.2.1 Formulation

In order to explain this procedure, let us consider a cylinder with a radius a_1 in free space. The cylinder is illuminated by a transmitting line source tx_m and operates at a frequency f. It is assumed that the dielectric properties of the cylinder, i.e. the dielectric constant ε_{r1} and the conductivity σ_1 are known. The cylinder is envisaged to contain an inclusion (fig. 3.1), here assumed to be cylindrically-shaped and with a higher dielectric constant than ε_{r1}. The problem consists of identifying the presence and location of the inclusion by using only the fields measured outside the cylinder.

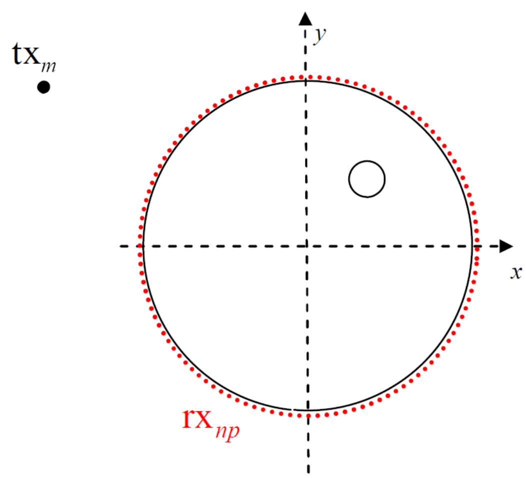

Figure 3.1: Pictorial view of the problem, with the red and black dots representing the receiving and transmitting positions, respectively.

Assume that the field at the surface points $\mathrm{rx}_{np} = (a_1, \phi_{np})$ is known, such that:

$$E^{\text{known}}_{\mathrm{tx}_m}|_{\mathrm{rx}_{np}} = E^{\text{known}}_{np,\mathrm{tx}_m} \quad \text{with} \quad np = 1, \ldots, N_{\mathrm{PT}} \tag{3.1}$$

where N_{PT} indicates the number of measured points across the outside cylinder. By exploiting the cylindrical symmetry of the problem, the field within the cylinder is expressed as the summation of Bessel functions, or modes, as follows:

$$E_{\mathrm{MM}}^{\mathrm{rcstr}}(\rho,\phi;\mathrm{tx}_m;f)=\sum_{n=-\infty}^{n=\infty}a_nJ_n(k_1\rho)e^{jn\phi}\approx\sum_{n=-N_F}^{n=N_F}a_nJ_n(k_1\rho)e^{jn\phi} \tag{3.2}$$

In eq. (3.2), k_1 represents the wave number of the cylinder and is assumed to be uniform, the string "rcstr" is used to indicate the reconstructed internal field, while the string "MM" indicates that mode-matching procedure will be employed.

Moreover, the size of the reconstructed field will depend on the illuminating source and the frequency (since $E_{np,\mathrm{tx}_m}^{\mathrm{known}}$ depends on these parameters). The summation in eq. (3.2) contains an infinite number of terms: to render the problem manageable, the summation needs to be truncated after N_F terms, where N_F has to be determined. If $(1+2N_F)<N_{\mathrm{PT}}$, then the weights a_n can be calculated by following the least mean square (LMS) approach. For this purpose, we write the matrix equation $ZA\approx B$, where:

$$Z=\begin{bmatrix} J_{-N_F}(k_1a_1)e^{-jN_F\phi_1} & \dots & J_{N_F}(k_1a_1)e^{jN_F\phi_1} \\ \dots & & \dots \\ J_{-N_F}(k_1a_1)e^{-jN_F\phi_{N_{\mathrm{PT}}}} & \dots & J_{N_F}(k_1a_1)e^{jN_F\phi_{N_{\mathrm{PT}}}} \end{bmatrix} \tag{3.3}$$

$$A=\begin{bmatrix} a_{-N_F} & \dots & a_{N_F} \end{bmatrix}^T \tag{3.4}$$

and

$$B=\begin{bmatrix} E_{1,\mathrm{tx}_m}^{\mathrm{known}} & \dots & E_{N_{\mathrm{PT}},\mathrm{tx}_m}^{\mathrm{known}} \end{bmatrix}^T \tag{3.5}$$

The coefficient vector A can then be calculated by minimising the residuum:

$$\|r\|^2=\|ZA-B\|^2 \tag{3.6}$$

It then follows that:

$$A = (Z^{*T}Z)^{-1}Z^{*T}B \tag{3.7}$$

Having calculated the weights a_n, the reconstructed field is determined in the entire internal region using eq. (3.2), and it matches the field observed on the surface points rx_{np}. The constant number N_F has to be set large enough to allow an accurate reconstruction of the field, but also to avoid the matrix Z from becoming poorly scaled (singular).

The MM procedure is subject to linear Born approximation; this holds true because it can be shown that the linear Born approximation is equivalent to the least mean square error method which is used here to calculate the coefficients of the expansion.

Other authors have used expansion into functional series to reduce the ill-posedness of the inverse problem [59, 60]. In [59], an iterative algorithm is adopted to achieve the solution, leading to an increasing of the CPU time. In [60], the number of iteration is reduced by exploiting the adjoint variable method.

3.2.2 Validation Through Simulations

3.3.2.1 Cylinder without an inclusion: internal field reconstruction

Some numerical examples are now provided to show the capability of eq. (3.2) to represent the internal field [61]. First, we consider a cylinder without an inclusion, i.e. a homogenous cylinder. The cylinder ($a_1 = 5$ cm, $\varepsilon_{r1} = 4$, $\sigma_1 = 0$) is illuminated by a 0.001 amplitude line source located at ($\rho_{\mathrm{source}} = 8$ cm, $\phi_{\mathrm{source}} = \pi$) and operating at a frequency of $f = 9$ GHz. The field at $N_{\mathrm{PT}} = 180$ equally phi-spaced points lying on the external surface, $E^{\mathrm{known}}_{np,\mathrm{tx}_m}$, is calculated, and these values are used to fill the vector B. Note that the number of points used leads to a spatial sampling of approximately $0.1\lambda_1$, where λ_1 represents the wavelength in the cylinder. Moreover, it is worthwhile to point out that in the examples presented in this section $E^{\mathrm{known}}_{np,\mathrm{tx}_m}$ has been determined analytically, while in realistic situations it will be determined through measurements. Next, the Z matrix is constructed using $N_F = 50$; this value has been chosen after a check on the convergence of the solution (performed by evaluating the relative error in magnitude of the reconstructed field); the same value is used in all examples given in this chapter. It has to be clearly pointed out that the dimensions of the Z matrix are rather small being equal to $(1+2N_F)\times N_{\mathrm{PT}}$, and conversely to other inverse techniques, they are not related to the discretisation of the volume where the image is required. Finally, the weights a_n are obtained by resorting to eq. (3.7) and the internal field is reconstructed. In fig. 3.2(a) the linear magnitude of the reconstructed internal field is plotted, while fig. 3.2(b) refers to the reference solution, which has been obtained by resorting to the analytical calculation for the entire internal region. By comparing the figures, it is possible to see that the use of MM Bessel functions procedure permits the accurate reconstruction of the internal field of homogenous cylinders.

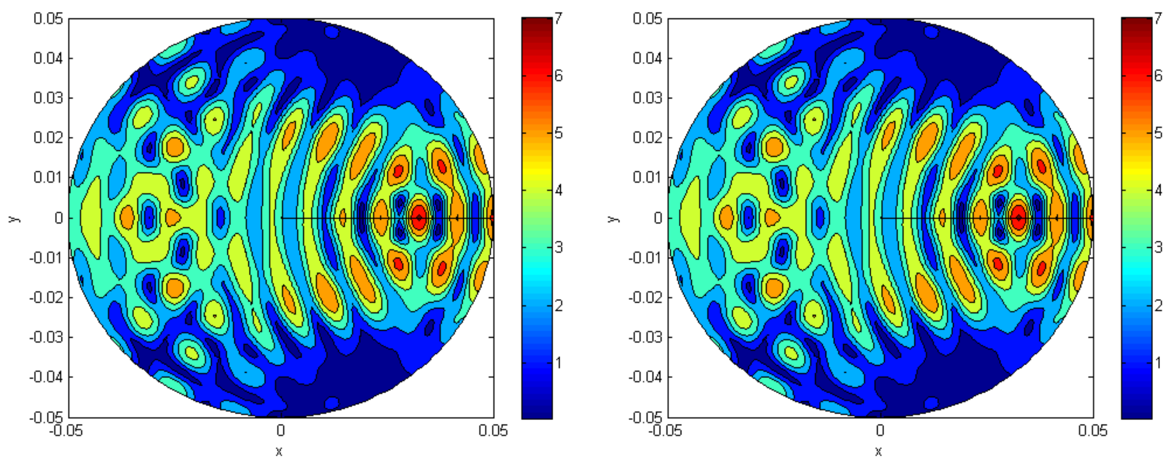

(a)

(b)

Figure 3.2: Linear magnitude of the field of a homogeneous cylinder illuminated by a line source: (a) reconstructed and (b) reference field, obtained through the MM procedure. x and y axes are in metres.

3.3.2.2 Cylinder with an inclusion: internal field reconstruction

Next, a cylinder with an inclusion is considered; in particular, a concentric 5 mm radius PEC cylindrical inclusion is assumed. The cylinder is illuminated by the same line source as in the previous case and the field at $N_{\mathrm{PT}} = 180$ points lying on the external surface, $E^{\mathrm{known}}_{np,\mathrm{tx}_m}$, is calculated; next, the MM Bessel functions procedure is employed to reconstruct the internal field. In fig. 3.3(a) the linear magnitude of the reconstructed internal field is plotted when using $N_F = 50$, while fig. 3.3(b) refers to the reference solution, which has been obtained by resorting to analytical calculation for the entire internal region.

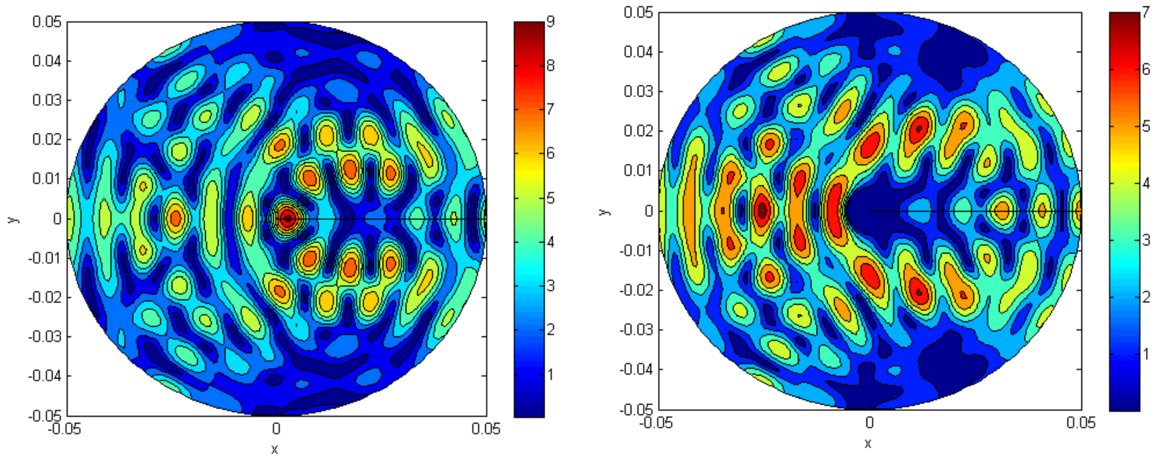

(a) (b)

Figure 3.3: Linear magnitude of the field of cylinder with inclusion illuminated by a line source: (a) reconstructed and (b) reference field, obtained through the MM procedure. x and y axes are in metres.

From the figures, it is possible to note that the internal field is reconstructed quite well everywhere except "near" and "inside" the inclusion. This is due to the difference in properties between the two media, which is not taken into account by eq. (3.2) (Some discrepancy can be seen on the right side of figures, which is due to the contour plotting algorithm connecting the wrong points, and can be fixed by changing the threshold). Moreover, a mismatch in the region of transition of the two media is clearly visible in the reconstructed field, paving the way for a new strategy for detection and localisation. Considering the problem in more detail, suppose the external cylinder is illuminated using a range of different frequencies and from different illuminating points; all the reconstructed fields will exhibit the mismatch, which will always be located in the region of transition of the two media. Thus, by summing incoherently all the solutions, i.e. the reconstructed fields, the inclusion will be detected and localised.

Mathematically speaking, assuming we use M transmitting sources tx_m with $m = 1, 2, ..., M$, and F frequencies f_i with $i = 1, 2, ..., F$, it follows that the intensity of the final image I can be obtained through the following equation:

$$I(\rho, \phi) = \frac{1}{B} \sum_{m=1}^{M} \sum_{i=1}^{F} \Delta f |E_{\mathrm{MM}}^{\mathrm{rcstr}}(\rho, \phi; \mathrm{tx}_m; f_i)|^2 \tag{3.8}$$

where Δ_f and B are the frequency sampling and the bandwidth, respectively. The resolution is expected to achieve the optical resolution limit of $\lambda_{1,f_{\max}}/4$, where $\lambda_{1,f_{\max}}$ represents the wavelength in the cylinder calculated at the highest frequency; this gives a rule of thumb for determining the highest frequency to be used.

3.3.2.3 Cylinder with an inclusion: detection and localisation

A numerical example is now provided to validate the proposed method. Consider a cylinder with a radius of 5 cm, which has dielectric constant and conductivity values of 10 and 0, respectively ($a_1 = 5$ cm, $\varepsilon_{r1} = 10$, $\sigma_1 = 0$). The cylinder has an eccentrically placed cylindrically-shaped inclusion with radius $a_2 = 2.5$ mm, dielectric constant of $\varepsilon_{r2} = 50$, and conductivity $\sigma_2 = 0$; the distance between the centres of the two cylinders is 1 cm (see fig. 3.4).

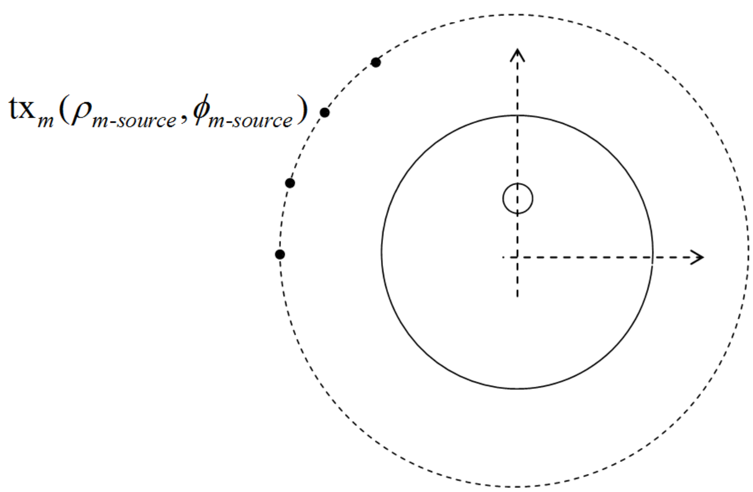

Figure 3.4: Pictorial view of the problem: multi-sources illumination (not to scale).

The cylinder is illuminated by $M = 12$ transmitting line sources tx_m with $m = 1, 2, ..., M$, located at a distance of 8 cm from the centre and equally spaced along phi. Frequency band of 8-10 GHz was considered, and a frequency sample spacing of 10 MHz was used. For each frequency sample and each illuminating source, the field $E^{\text{known}}_{np,\text{tx}_m}$ at $N_{\text{PT}} = 180$ points lying on the external surface was calculated. Then, the MM Bessel functions procedure was employed to reconstruct the internal field. It should be noted that in this example, $E^{\text{known}}_{np,\text{tx}_m}$ has been determined analytically by resorting to [46] and [47].

Figures 3.5(a), (b) and (c) show the linear magnitude of the reconstructed fields corresponding to a given frequency sample and 3 different illuminating sources. The figures highlight the fact that all the reconstructed fields exhibit the mismatch, which is always located in the region of the transition of the two media.

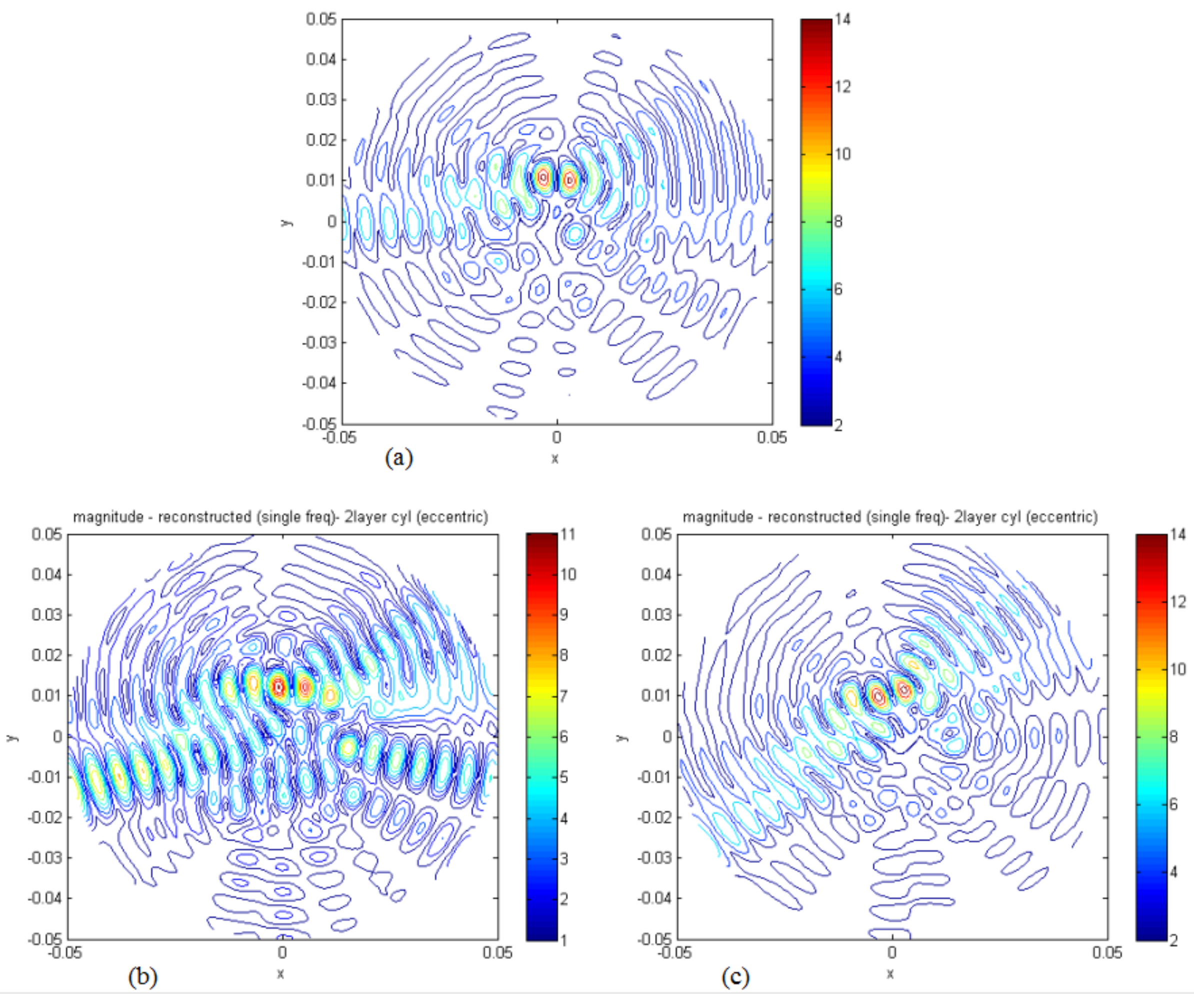

Figure 3.5: Linear magnitude of the field of cylinder with inclusion illuminated by a line source: reconstructed field obtained through the MM procedure when considering f=9 GHz and (a) $\phi_{\text{source}} = 180°$, (b) $\phi_{\text{source}} = 195°$, (c) $\phi_{\text{source}} = 210°$; x and y axes are in metres.

Figure 3.6 shows the linear normalised intensity obtained through eq. (3.8); a peak can be clearly detected in the region of the inclusion. This region is indicated inside the figure with a white circle surrounding it. Thus, both detection and localisation are achieved [62]. By observing the figure, it can be stated that the resolution (the dimension of the region with normalised intensity greater than 0.5) is approximately 2.5 mm. This value is in agreement with the expected optical resolution limit of $\lambda_{1,f_{\max}}/4$. For the signal to clutter ratio (S/C), defined as the quantity which compares the maximum inclusion response with the maximum clutter response in the same image, a value of 7 dB was achieved. This value was obtained with $M = 12$ transmitting positions and 2 GHz of bandwidth. A lower number of transmitting positions leads to a lower S/C, while an increase of the bandwidth leads to a higher S/C [63].

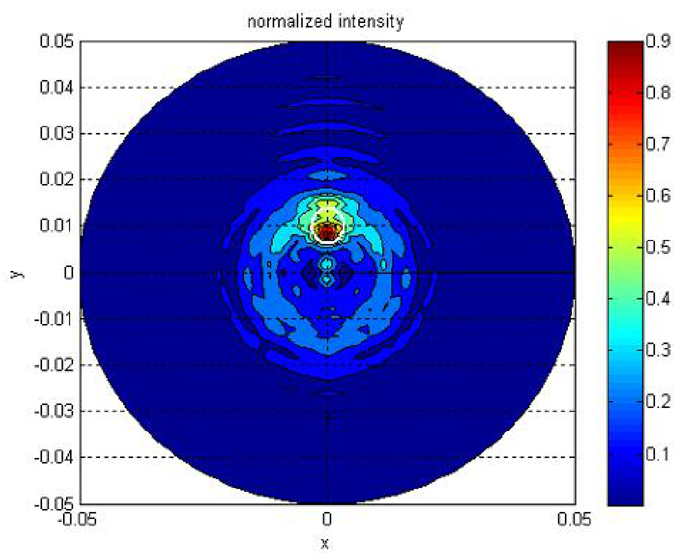

Figure 3.6: Linear normalised intensity obtained by adding all the reconstructed fields gathered using different frequencies and from different illuminating points; the white circle indicates the position of the inclusion. x and y axes are in metres.

In this example, the values for dielectric constant of two media (ε_{r1} and ε_{r2}) were chosen according to [28] and [29] to more realistically reproduce the normal and malignant breast tissue properties in the band of interest. Accordingly, it is worth pointing out that in the example considered here, the electrical properties of the external cylinder were assumed to be frequency independent. However, frequency dependence of the electrical properties can also be taken into account by this approach.

It must be pointed out that in [28] and [29] the contrast between malignant tissue and healthy breast tissue is assumed to be quite significant (i.e. equal or greater than a factor of 5 in permittivity and conductivity). However, more recent studies indicate that such contrast exists between malignant and fatty (or adipose) breast tissue, while the contrast between malignant and healthy fibroglandular tissues can be as low as 10% in both permittivity and conductivity [64].

3.3 Measurement Results

3.3.1 Cylinder with an Inclusion

The capability of the MM Bessel function procedure to detect and locate inclusions has been verified through measurements. Specifically, a cast Poly Methyl Methacrylate (P.M.M.A.) cylinder having a radius of 4.25 cm and a height of 30 cm was constructed. The cylinder has electrical properties of ε_{r1}=2.7 and $\sigma_1 = 3 \times 10^{-7}$ S/m, where ε_{r1} and σ_1 represent the dielectric constant (relative permittivity) and the conductivity of the cylinder, respectively. The cylinder has an eccentric inclusion, made from a PEC cylinder with a radius of 3 mm. The distance between the two cylinders is approximately 2.1 cm as shown in fig. 3.7.

Frequency-domain UWB measurements in an anechoic chamber were performed, using a VNA arrangement to obtain the transfer function at 1601 discrete frequencies, in the band of 6-10 GHz (frequency sampling of 2.5 MHz), and using the nominal power output of the VNA (2mW). Wideband bow-tie antennas, vertically polarised and omni-directional in the azimuth plane were used, after a proper check of s-parameters. For each set of measurements, the transmitting antenna was fixed at approximately 20 cm from the centre of the cylinder, while the receiver antenna was positioned close to the external surface of the cylinder and placed on a computer-controlled rotating stage with 3° of angular resolution (fig. 3.8).

Next, the field $E^{\text{known}}_{np,\text{tx}_m}$ at N_{PT}=120 equally phi-spaced points lying on the external surface

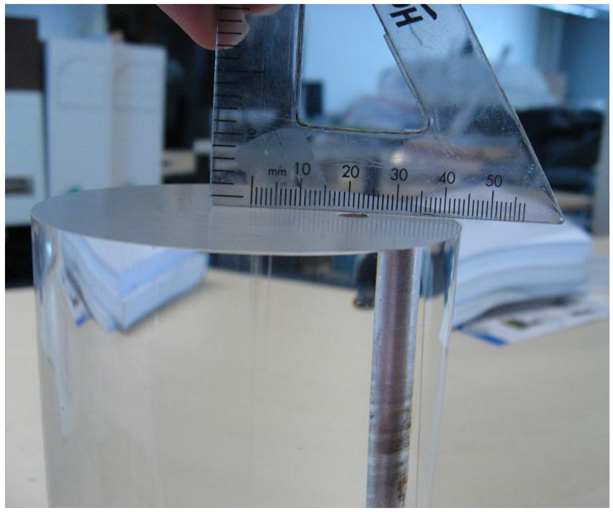

Figure 3.7: Close up image of cast P.M.M.A. cylinder with PEC eccentric inclusion.

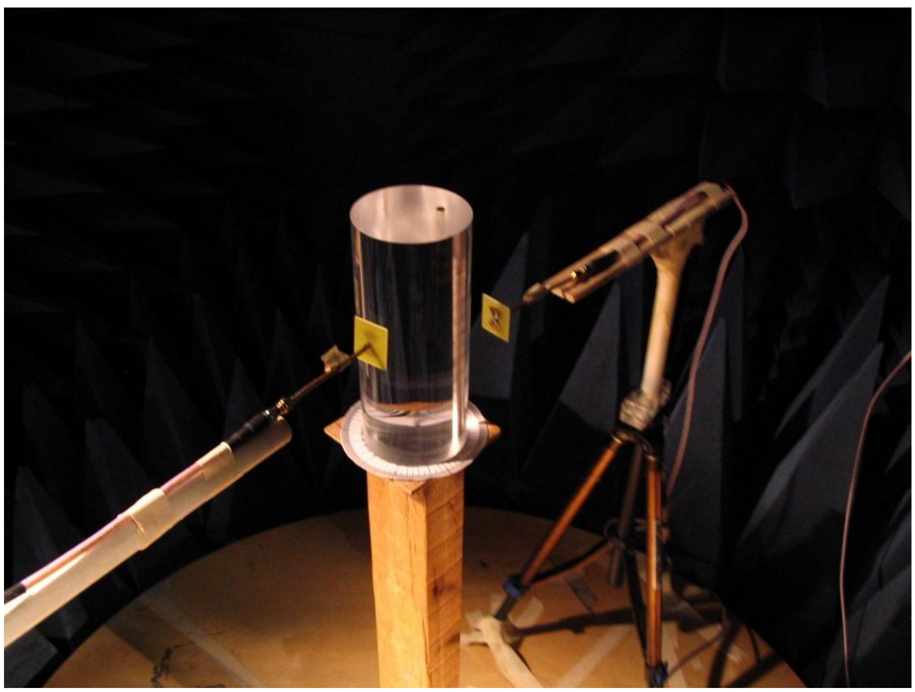

Figure 3.8: Measurement equipment, transmitting and receiving antennas are on the right and left sides of the figure, respectively.

was measured. It should be noted that these number of points lead to a spatial sampling of approximately $0.1\lambda_{1,f_{\max}}$, where $\lambda_{1,f_{\max}}$ represents the wavelength in the P.M.M.A. cylinder calculated at the highest measured frequency (10 GHz). By changing the position of the transmitting antenna by 30° between each set of measurements, 12 sets of data were recorded (fig. 3.9).

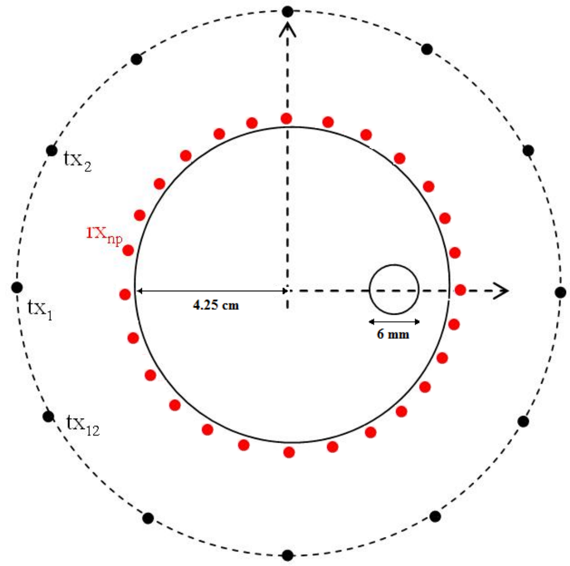

Figure 3.9: Pictorial view of the problem, with the red and black dots representing the receiving and transmitting positions, respectively.

Figure 3.10 shows the normalised intensity obtained through eq. (3.8) after proper image adjustments. The image is adjusted by enforcing to zero the intensity values below 0.5 and expanding from 0 to 1 of the values above 0.5. It can be seen that a peak can be clearly detected in the region of the inclusion, which is marked with a white circle. Two other smaller peaks can also be observed in the image, which most probably correspond to the mirror images (which are imaging artifacts) and have intensity values of less than 0.5. Therefore, both detection and localisation are achieved [65]. The total time required to perform all 12 sets of measurements was approximately 2 hours, while the CPU time required to process the MM Bessel function procedure on MATLAB was approximately 45 minutes on an Intel Pentium M 2 GHz with 1 GB RAM system. In section 4.3.2, it will be shown that the measurement time will be reduced by a factor of 5, if a spatial sampling of $0.5\lambda_{1,f_{\max}}$ is used.

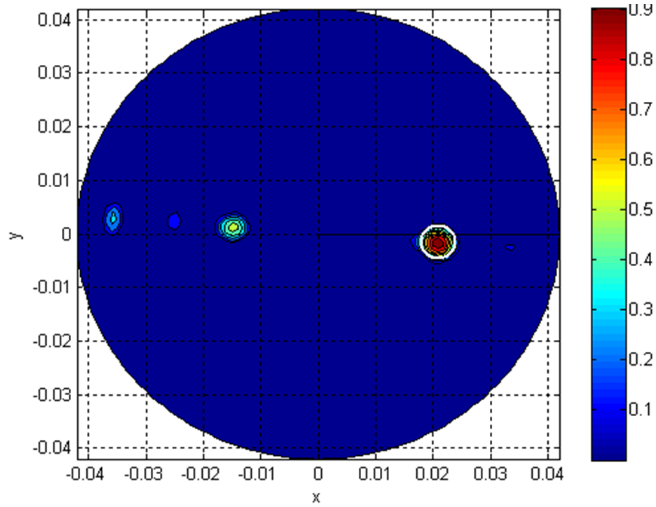

Figure 3.10: Linear normalised intensity, with the white circle indicating the position of the inclusion.

3.3.2 Cylinder with Multiple Inclusions

Here, to assess the applicability of MM procedure in solving more complex problems, a medium with two inclusions was considered. A P.M.M.A. cylinder ($\varepsilon_{r1} = 2.7$, $\sigma_1 = 3 \times 10^{-7}$ S/m), with identical geometry to the one in the previous section but now with an extra inclusion, was constructed. The cylinder has an eccentric inclusion consisting of a PEC cylinder with a radius of 3 mm, and in addition, a second inclusion was emplaced by drilling a 3 mm radius hole at 90° (relative to centre) from the PEC and filling it with an Agar-Agar solution (fig. 3.11). The distance between the centres of each inclusion and that of the outer cylinder is approximately 2.1 cm. The Agar-Agar was dissolved in hot water at approximately 95°C and then cooled to room temperature to form a semi-transparent gel. The dielectric constant and the conductivity are functions of the concentration of the Agar-Agar [52]; for this experiment a concentration of approximately 6% (15g per 250g), leading to $\varepsilon_{r2} = 70$, $\sigma_2 = 1$ S/m, was used. Agar-Agar gels are often used for approximating high-water-content human tissues [66].

Frequency-domain UWB measurements in an anechoic chamber were performed, using a VNA arrangement to obtain the transfer function at 1601 discrete frequencies in the band of 6-8 GHz. Wideband bow-tie antennas, vertically polarised and omni-directional in the azimuth plane, were used (after checking that the S_{11} is lower than -10 dB in the band of interest). For

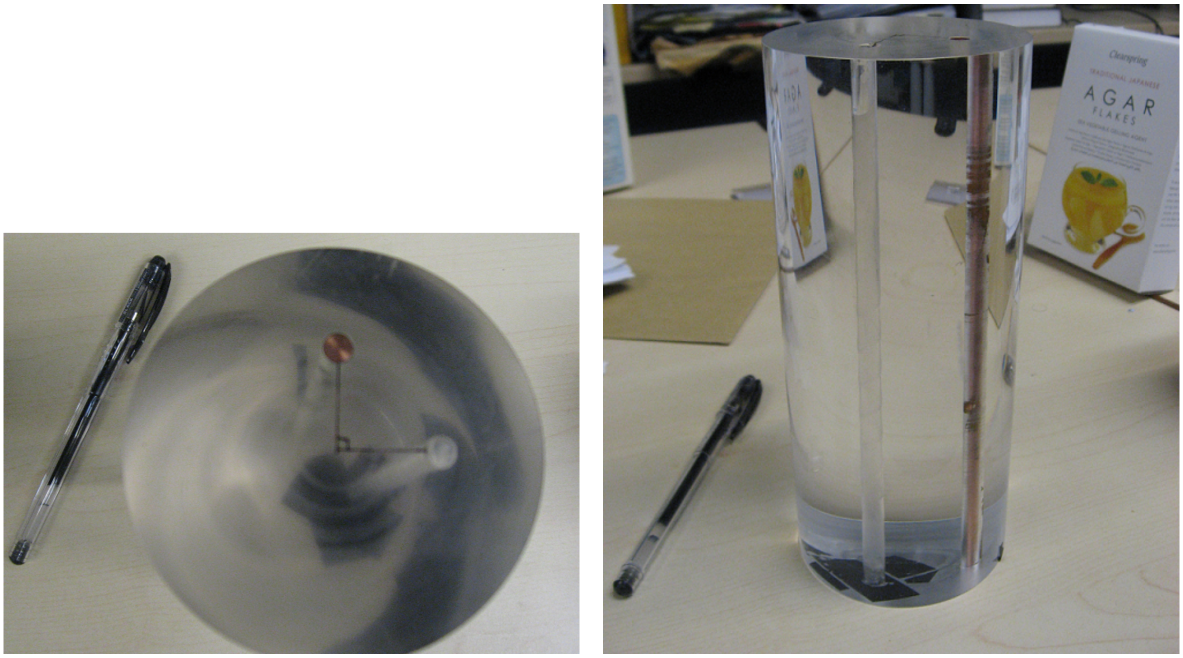

(a) (b)

Figure 3.11: Cast P.M.M.A. cylinder having a radius of 4.25 cm with PEC and Agar-Agar solution inclusions: (a) from above, (b) from side.

each set of measurements, the location of the transmitting antenna was fixed at approximately 20 cm away from the centre of the cylinder, while the receiver antenna was positioned close to the external surface of the cylinder and placed on a computer controlled rotating stage with 3° of angular resolution. Thus, the field $E^{\text{known}}_{np,\text{tx}_m}$ at N_{PT}=120 equally phi-spaced points lying on the external surface were measured. A total number of $M = 6$ sets of data were recorded (with $m = 1, 2, ..., 6$), changing the position of the transmitting antenna along phi with a step of 60°; fig. 3.12 shows the linear normalised intensity obtained through eq. (3.8) after a proper image adjusting. Two peaks can be clearly detected in the region of inclusions, with different intensities. Specifically, the peak with the higher intensity corresponds to the PEC cylinder (due to the fact that a greater contrast, i.e. greater mismatch boundaries, occurs when going from P.M.M.A. to PEC cylinder), while the less intense peak represents the location of the Agar-Agar solution cylinder. Hence, both detection and localisation are achieved, showing the ability of the methodology in resolving multiple scatterers and paving the way for addressing problems involving tissue inhomogeneities too.

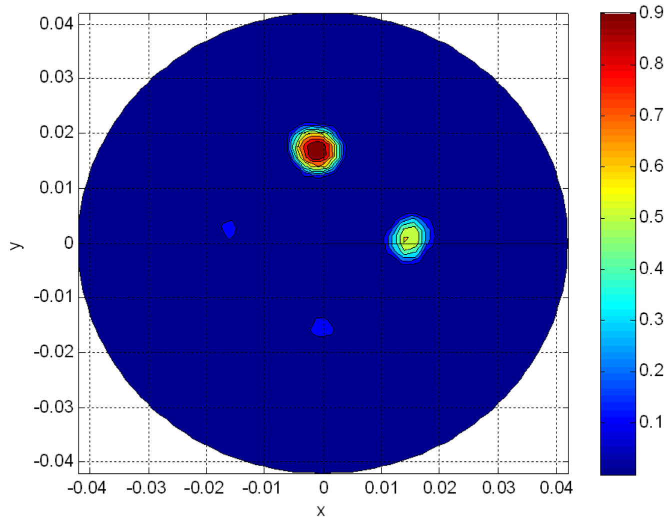

Figure 3.12: Normalised intensity (linear) obtained through eq. (3.8) when using a cast P.M.M.A. cylinder having a radius of 4.25 cm with PEC and Agar-Agar solution inclusions.

3.4 Summary

In this chapter, it has been shown that the MM Bessel function procedure permits the detection of the presence and location of significant scatterers inside cylinders. Using the MM Bessel function procedure leads to the generation/inversion of a rather small matrix, whose dimensions are not related to the discretisation of the volume where the image is required. The method allows all the information in the frequency domain to be utilised by combining the information from the individual frequencies to construct a consistent image with a resolution of approximately one quarter of the shortest wavelength in the dielectric medium. Validation of the technique through both simulations and measurements has been performed and presented, illustrating the effectiveness of the method. It follows that, if the properties of the external object are known, both detection and localisation are achieved using MM. Further research will be focused on the investigation on the robustness with respect to errors in the measurement grid and knowledge of the dielectric properties of the target volume.

The use of Bessel functions seems to limit the applicability to cylindrically-shaped volumes. One can think to replace Bessel functions with Mathieu functions [67, 68] or spherical Bessel functions [69] if ellipsoidal and spherical problems are encountered. An extension to more realistic 3D geometries is possible by resorting to the extraction of the modes. Specifically, the modes are a set of basis functions that are necessary and sufficient for the representation of the electromagnetic field inside the object (at a given frequency); the modes can be numerically evaluated by resorting to the characteristic basis function method (CBFM) [70, 71]. In any case, the need of finding a more efficient method, both in terms of computational cost and time, and applicability to more general geometries was evident, and therefore, a new imaging technique was investigated . This new technique, based on the Huygens principle will be introduced in the next chapter.

4

Proposed Imaging Technique II: Huygens-Principle-Based Procedure

4.1 Introduction

In the previous chapter, the first proposed imaging technique employing MM of Bessel functions was investigated. It was shown that this approach permits the detection of the presence and location of significant scatterers inside cylindrical volumes. However, MM requires matrix generation and inversion, and the knowledge of the field on the entire external surface; moreover, the use of Bessel functions limits the applicability of this procedure to cylindrically-shaped objects. Therefore the extension of this approach to more realistic 3D geometries would not be trivial. Hence, due to these difficulties, another approach was needed to be exploited; this novel, fast, and accurate microwave imaging method is based on the principles of physical optics. The method deals with the Huygens Principle (HP) [72, 73]: Using HP to forward-propagate the waves removes the need to solve inverse problems and, consequently, no matrix generation/inversion is required. Together with its simplicity, it will be shown that the methodology permits the capturing of the extent to which different tissues, or differing conditions of tissues, can be discriminated, and hence provides contrast in the final image. Moreover, UWB allows all the information in the frequency domain to be utilised by combining the information from the individual frequencies to construct a consistent image. It follows that the methodology can identify the presence and location of significant scatterers inside a volume.

The formulation of HP is presented in detail in the following section. Next, the validation of the technique through both simulations and measurements involving cylinders and spheres with one or more inclusions has been performed, and results are presented in the final two sections of this chapter. Following on from this initial exposition, all the simulation and measurement results involving mediums with multiple layers, and employing HP will be presented separately in chapter 5.

4.2 Formulation

As stated previously, a key feature of the MM based procedure is that a mismatch appears in the region of transition between the two media. The mismatch is due to the difference between the properties of the two media, which is not taken into account by eq. (3.2). Such mismatch offers the capability of capturing the contrast, and it can be used for detection and localisation of inhomogeneities. To make a comparison between the HP and the MM method, let's consider the same example that was given in the MM chapter (fig. 4.1). The HP states that: "Each locus of a wave excites the local matter which reradiates a secondary wavelets, and all wavelets superpose to a new, resulting wave (the envelope of those wavelets), and so on" [72]. Therefore we consider what would happen if we apply the HP using $E^{\text{known}}_{np,\text{tx}_m}$ as locus of a wave. Then, in order to exploit such a strategy, we calculate the field inside the cylinder as the superposition of the fields radiated by the N_{PT} observation points of eq. (3.1):

$$E^{\text{rcstr}}_{\text{HP,2D}}(\rho,\phi;\text{tx}_m;f) = \Delta_s \sum_{np=1}^{N_{PT}} E^{\text{known}}_{np,\text{tx}_m} J_0(k_1|\overrightarrow{\rho}_{np} - \overrightarrow{\rho}|) \tag{4.1}$$

where $(\rho,\phi) \equiv \overrightarrow{\rho}$ is the observation point, k_1 represents the wave number for the media constituting the cylinder, and Δ_s is the spatial sampling. In eq. (4.1), the string "rcstr" is used

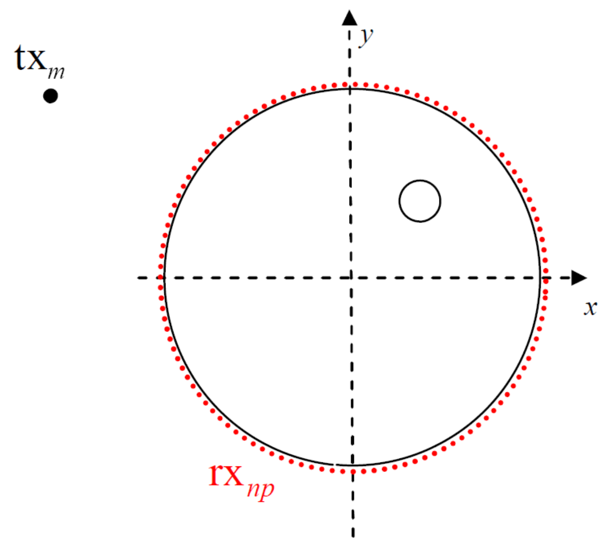

Figure 4.1: Pictorial view of the problem, with the red and black dots representing the receiving and transmitting positions, respectively.

to indicate the reconstructed internal field, while the string “HP” indicates that an HP-based procedure will be employed. Moreover, we note that the reconstructed field will depend on the illuminating source and the frequency (since $E^{\text{known}}_{np,\text{tx}_m}$ depends on these parameters). In eq. (4.1), the Bessel functions for homogeneous media are used to forward propagate the field. However, when dealing with 3-D problems, the Green’s function can be used. Thus, we have:

$$E^{\text{rcstr}}_{\text{HP,3D}}(r,\theta,\phi;\text{tx}_m;f) = \Delta_s \sum_{np=1}^{N_{PT}} E^{\text{known}}_{np,\text{tx}_m} G(k_1|\overrightarrow{r}_{np} - \overrightarrow{r}|) \tag{4.2}$$

where $(r,\theta,\phi) \equiv \overrightarrow{r}$ is the observation point. It follows that eq. (4.1) can be used for 2-D problems (such as cylinders), while eq. (4.2) represents the generalisation to 3-D problems.

It should be emphasised that the HP procedure does not give the correct internal field, even when dealing with homogenous problems. This is due to the essence of HP, which is formulated for far field phenomena, i.e. it refers to a propagating wavefront. More in detail, to be able to capture the far field, only the knowledge of the E field is enough as we have plane wavefronts. On the other hand, to be able to capture and recover the near field, the knowledge of the H field or normal derivative of the E field is also necessary. Anyhow, in this case the intention is not to evaluate the internal field, but to see if the HP can capture the contrast (mismatch boundaries) and locate an inclusion within a volume (as in MM procedure). The capability of capturing the contrast is due to the difference in properties between the two media, which is not considered in eqs. (4.1) and (4.2). Consequently, the reconstructed field exhibits a mismatch in the region of transition of the two media. This mismatch opens the way for a new detection and localisation strategy. In order to further explain this problem, suppose the external cylinder is illuminated using a range of different frequencies and from different illuminating points; all the reconstructed fields will exhibit the mismatch, which will always be located in the region of transition of the two media. Hence, by summing up incoherently all the solutions, i.e. the reconstructed fields, the inclusion will be detected and localised.

Mathematically speaking, assuming we have M transmitting sources tx_m with $m = 1, 2...M$, and F frequencies f_i, then the Intensity of the resulting image I using Bessel and Green's functions respectively can be obtained through the following equations:

$$I_{2D}(\rho,\phi) = \frac{1}{B}\sum_{m=1}^{M}\sum_{i=1}^{F}\Delta_f|E^{\mathrm{rcstr}}_{\mathrm{HP,2D}}(\rho,\phi;\mathrm{tx}_m;f_i)|^2 \tag{4.3}$$

$$I_{3D}(r,\theta,\phi) = \frac{1}{B}\sum_{m=1}^{M}\sum_{i=1}^{F}\Delta_f|E^{\mathrm{rcstr}}_{\mathrm{HP,3D}}(r,\theta,\phi;\mathrm{tx}_m;f_i)|^2 \tag{4.4}$$

where Δ_f and B are the frequency sampling and the bandwidth, respectively. The resolution is expected to reach the optical resolution limit of $\lambda_{f_{\max}}/4$, where $\lambda_{f_{\max}}$ represents the wavelength in the cylinder calculated at the highest frequency; this gives the rule of thumb for determining the highest frequency to be used.

Finally, it should be emphasised that the use of Green's function implies a singularity for $|\overrightarrow{r}_{np} - \overrightarrow{r}| = 0$. This singularity can be removed by performing a multiplication between the same Green's function and $|\overrightarrow{r}_{np} - \overrightarrow{r}|$. Furthermore, when dealing with mediums with high losses, the constant k_1 in eqs. (4.1) and (4.2) can be replaced with $\mathrm{Re}\{k_1\}$, in order to compensate the field attenuation, which could mask the target feature.

The proposed procedure can be seen as an application of holography theory, first developed by R. P. Porter and A. J. Devaney in the early 1980s [74, 75], who showed that an inverse source problem can be determined from the value of the field and its normal derivative over any closed surface completely surrounding the volume of interest. However, [74, 75] are focused on recovering an image of the dielectric properties in the volume. Conversely, the approach proposed here solves a simpler computational problem by seeking only to identify the significant scatterers; to achieve our goal, only the field on an arbitrary closed surface is used. For this purpose, in [76], it is shown that, under certain conditions, an exact solution can be derived by using only the field on an arbitrary closed surface. Moreover, in the same [76], the well known delay-and- sum algorithm (back-propagation) is demonstrated quantitatively from basic physics.

The proposed HP-based procedure is equivalent to a synthetic time-reversal algorithm performed in the frequency domain for a wide range of frequencies. In time-reversal and delay-and-sum algorithms, which do not require any inverse problem solution perform a non-coherent summation in the time domain; here instead, the non-coherent summation is performed in the frequency domain for each frequency component. This means that the approach allows all the information in the frequency domain to be utilised by combining the information from the individual frequencies to construct a consistent image.

Furthermore, there is a difference between HP and Kirchhoff migration method [77], whose algorithms usually perform time-reversal and back-propagation to find the phase, that is, time traces. Conversely, here we are not interested in finding the phase traces; in fact, we use HP with the aim of reconstructing the field. In the reconstruction process, if the Green's function for a homogeneous medium is used, a mismatch appears when going from one medium to another, and the capability of capturing the mismatch boundaries represents the key feature of the proposed method allowing the detection of anomalies. This difference between the proposed HP-based procedure and the Kirchhoff migration method is further supported by the observation that the position of the transmitter is not required at any step of the image reconstruction algorithm [63, 78]. In section 4.3.2, it will be shown that this feature is capable of providing as good or even better performances when compared to conventional time-domain approaches.

4.3 Validation Through Simulations

4.3.1 Cylinder with a Single Inclusion

To clarify the method, let us consider a cylinder, with an inclusion. In particular, the external cylinder is assumed to have a radius of 4.25 cm, and is constituted by cast P.M.M.A. with dielectric constant and conductivity values of 2.7 and 3×10^{-7} S/m, respectively. The inclusion is a PEC cylinder having a radius of 3 mm, a radial offset of 1 cm and an angular offset of 45° [fig. 4.2(a)]. One single transmitting line source illumination tx_1 is considered, while the frequency band spans from 8 to 10 GHz with frequency sample spacing of 10 MHz. For each frequency sample, the field at $N_{\mathrm{PT}} = 180$ points lying on the external surface of the cylinder was calculated analytically by resorting to [46] and [47].

In order to be able to distinguish between the two fields, the notation $E_{np,\mathrm{tx}_1}^{\mathrm{known,withrod}}$ has been used to refer to the field corresponding to the cylinder with a rod, illuminated by tx_1. Next, the HP procedure is applied to $E_{np,\mathrm{tx}_1}^{\mathrm{known,withrod}}$, and the image is obtained through eq. (4.3). The resulting image can be seen in fig. 4.2(b); a peak can be detected, but not at the location of the inclusion. This peak is postulated to be the image of the transmitter, which masks the image of the rod, thus detection cannot be achieved.

Next, we consider the same cast P.M.M.A. cylinder, but without an inclusion [fig. 4.3(a)], again, the cylinder is illuminated using the single transmitting line source tx_1. HP is applied to $E_{np,\mathrm{tx}_1}^{\mathrm{known,norod}}$ (notation is used to indicate the field corresponding to the the cylinder without the rod), and the image is obtained through eq. (4.3). Again, the peak representing the image of the transmitter appears, supporting the postulation [see fig. 4.3(b)]. This is further supported by the observation that this feature moves as the position of the transmitter is varied.

As the last step, HP is applied to the difference between the two fields, (i.e. $E_{np,\mathrm{tx}_1}^{\mathrm{known,withrod}} -$

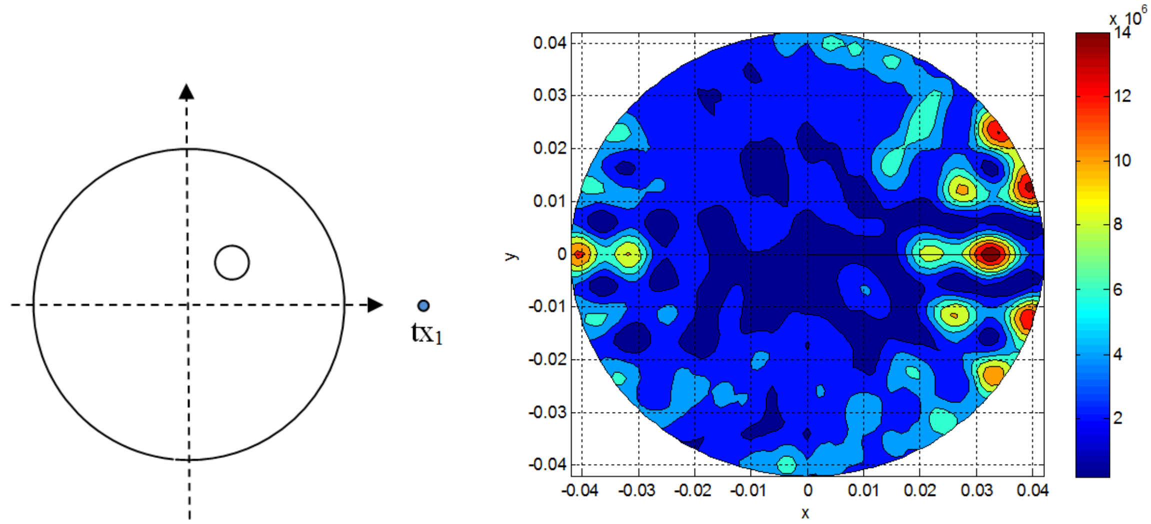

(a) (b)

Figure 4.2: (a) Cast P.M.M.A. cylinder with a PEC rod, (b) linear normalised intensity. x and y axes are in metres.

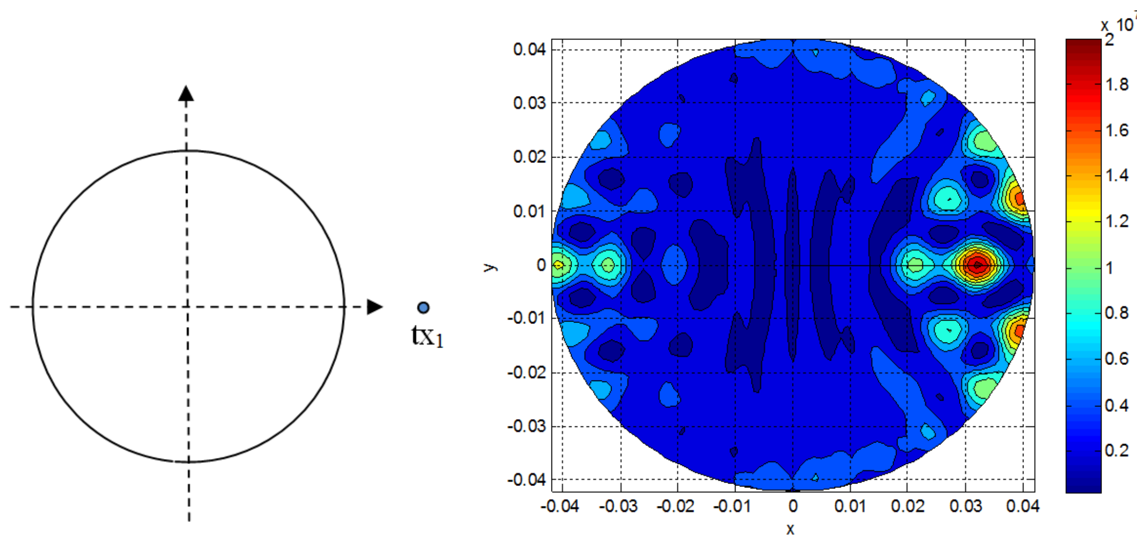

(a) (b)

Figure 4.3: (a) Homogeneous cast P.M.M.A. cylinder without the PEC rod, (b) linear normalised intensity. x and y axes are in metres.

$E^{\text{known,norod}}_{np,\text{tx}_1}$). Figure 4.4 shows the normalised intensity after an appropriate image adjusting (consisting in enforcing to zero the values below 0.25 and expanding from 0 to 1 the values above 0.25) obtained through eq. (4.3).

From the figure, it is possible to note that image of the transmitter has been removed, and the peak representing the rod appears. The other peak probably corresponds to a mirror image, but its intensity is lower than 0.5. The presence of the mirror image can be explained due to the circular symmetry of the transmitter positions, and Residual (fitting) error due to the convergence of the algorithm.

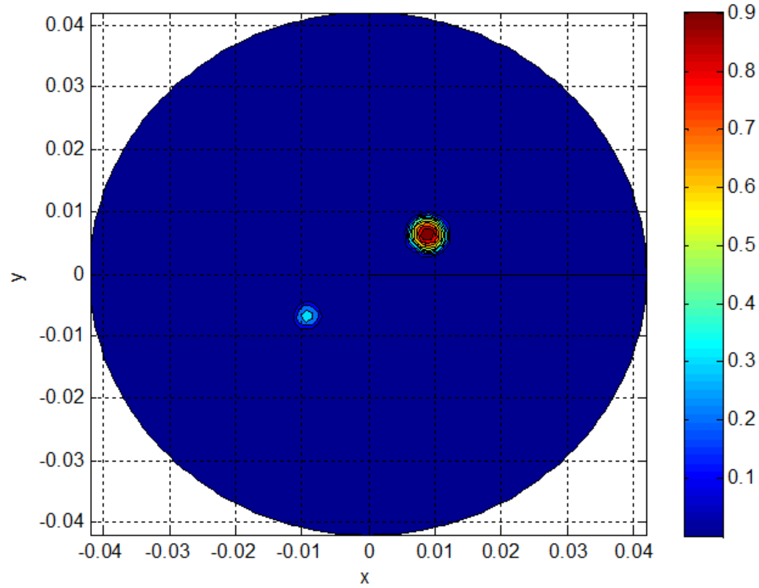

Figure 4.4: HP applied to the difference between two fields, linear normalised intensity obtained through eq. (4.3). x and y axes are in metres.

In a practical situation, it is not possible to determine $E^{\text{known,norod}}_{np,\text{tx}_1}$. However, it can be shown that the image of the transmitter can be removed, also by applying the HP as follows:

$$E^{\text{rcstr}}_{\text{HP,2D}}(\rho,\phi) = \Delta_s \sum_{np=1}^{N_{\text{PT}}} (E^{\text{known}}_{np,\text{tx}_m} - \text{avg}_M\{E^{\text{known}}_{np,\text{tx}_\text{m}}\}) J_0(k_1|\vec{\rho}_{np} - \vec{\rho}|) \tag{4.5}$$

$$E^{\text{rcstr}}_{\text{HP,3D}}(r,\theta,\phi) = \Delta_s \sum_{np=1}^{N_{\text{PT}}} (E^{\text{known}}_{np,\text{tx}_m} - \text{avg}_M\{E^{\text{known}}_{np,\text{tx}_\text{m}}\}) G(k_1|\vec{r}_{np} - \vec{r}|) \tag{4.6}$$

where $\text{avg}_M\{E^{\text{known}}_{np,\text{tx}_\text{m}}\}$ represents the average of signals obtained illuminating the object using M different transmitter positions. This in effect smears out the transmitter image; later in section 4.4.2, it will be shown that the minimum number of M=3 sources is required.

Next, let us consider a similar problem, this time assigning realistic human tissue electrical properties to the cylinder and the inclusion. Specifically, we consider a cylinder in free space with $a_1 = 4.25$ cm, $\varepsilon_{r1} = 10$ and $\sigma_1 = 0.4$ S/m. The cylinder has an eccentrically placed cylindrically-shaped inclusion having radius $a_2 = 3$ mm, dielectric constant $\varepsilon_{r2} = 50$ and conductivity $\sigma_2 = 5$ S/m; The distance between the centres of the two cylinders is again 1 cm and the phi offset is equal to 120°. The cylinder is illuminated by 12 transmitting line sources, located at a distance of 8 cm from the centre and equally spaced along phi. The band 1.5-7.5 GHz is considered, and a frequency sample spacing of 5 MHz is used. Note that the values of ε_{r1}, σ_1, ε_{r2} and σ_2 were chosen in accordance with [29] to reproduce the normal and malignant breast tissue properties. For this purpose, it is worthwhile pointing out that in the examples presented here the electric properties of the external cylinder have been assumed to be frequency-independent; however, a frequency-dependence of the electric properties can be taken into account by this approach. For each illuminating source and for each frequency sample, the field at 120 points on the external surface is calculated. Next, the average of 12 sets is computed and HP is applied as illustrated in eq. (4.5). Figure 4.5 shows the normalised intensity obtained through eq. (4.3). A peak can be clearly detected in the region of the inclusion; thus, both detection and localisation are achieved.

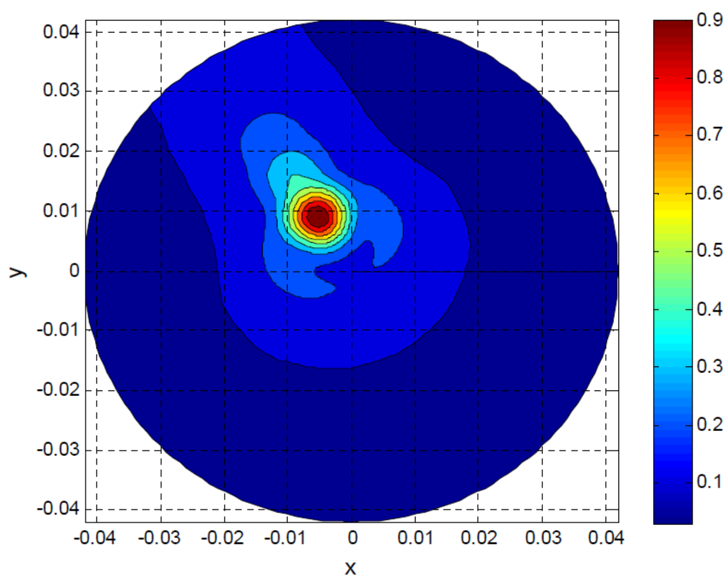

Figure 4.5: Cylinder ($\varepsilon_{r1} = 10$, $\sigma_1 = 0.4$ S/m) with eccentric inclusion ($\varepsilon_{r2} = 50$, $\sigma_2 = 5$ S/m) Linear normalised intensity obtained through eq. (4.3). x and y axes are in metres.

4.3.2 HP Methodology Characterisation

At this point, validation of the technique through simulations has been performed, illustrating the effectiveness of the method. However, the following points need to be accurately characterised with regards to the simulation in the previous section (fig. 4.5):

1. Analysis of signal-to-clutter ratio (S/C) and resolution with respect to the band.
2. Investigating the optimum number of employed transmitting and receiving positions.
3. Investigating the frequency sampling.
4. Analysis of the performance with respect to uncertain knowledge of the dielectric properties of the target volume.

Concerning the S/C, the following definition can be found in microwave breast-cancer imaging literature [27]: “The within-breast S/C compares the maximum tumour response with the maximum clutter response in the same image. The maximum clutter is determined by locating the maximum pixel value outside of the volume containing the imaged tumour (defined by twice the extent of the full-width at half-maximum (FWHM) response of the tumour)”.

Thus, let us refer to the aforementioned definition. To evaluate the S/C with respect to the band, we apply eq. (4.3) for different bandwidths: specifically, we perform image reconstruction assuming a bandwidth of 0.5, 1, 2, 4 and 6 GHz, respectively. In this example, the lower limit of the band coincides with the lower frequency. Next, for each image the S/C is calculated by applying the within-breast definition. It is worthwhile pointing out that within-breast S/C calculation has to be performed by using the not-normalised (and not-adjusted) image. Figure 4.6 shows the image obtained through eq. (4.3) when using 4 GHz of bandwidth (starting from 1.5 GHz); in the same image, the maximum tumour response and the maximum clutter response are highlighted, together with their correspondent intensity.

Figure 4.7(a) shows the S/C for the bandwidths given above. It is important to highlight that in HP procedure the within breast S/C approaches 8 dB for a bandwidth of 6 GHz. This value has been obtained with M=12 transmitter positions. Note that in [27], for a similar problem of 6 GHz bandwidth, a within breast S/C of 4.1 dB has been obtained by employing 45 transmitter

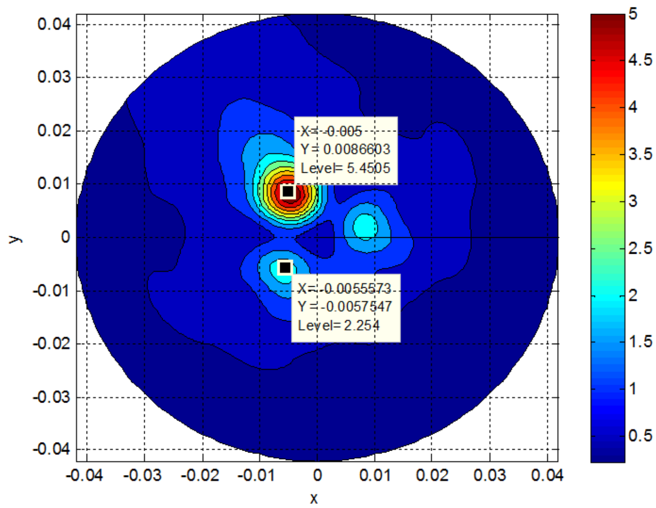

Figure 4.6: Image (not-normalised and not-adjusted) obtained through eq. (4.3) when using 4 GHz of bandwidth (1.5-5.5 GHz); the maximum tumour response and the maximum clutter response are highlighted. x and y axes are in metres.

positions, and using delay-and-sum beamforming algorithm.

Next, the resolution with respect to the band is addressed. Specifically, the resolution, here defined as the dimension of the region whose normalised intensity is above 0.5, is calculated assuming a bandwidth of 0.5, 1, 2, 4 and 6 GHz, respectively. It can be shown [see fig. 4.7(b)] that the resolution achieves the optical resolution limit of $\lambda_{1,f_{\max}}/4$, where $\lambda_{1,f_{\max}}$ represents the wavelength in the cylinder calculated at the highest frequency. From fig. 4.7(b), one could suggest to further increase the maximum frequency so as to obtain a better resolution; however, it has to be pointed out that we are dealing with lossy materials, that is, the penetration depth decreases if the frequency is increased.

Turning now to the investigation of the optimum number of employed transmitting positions, it will be shown that M=3 is the minimum number of transmitter positions used which can successfully smear out the transmitter image in both simulations and measurements, whilst achieving good detection and localisation. A lower number of transmitting positions M leads to a lower S/C and causes mirror ambiguity. It can be shown that a degradation of 4 dB occurs when using M=3 rather than M=12. Conversely, the S/C does not vary significantly from that given in fig. 4.7(a) if a lower number of receiving positions and a lower number of frequency

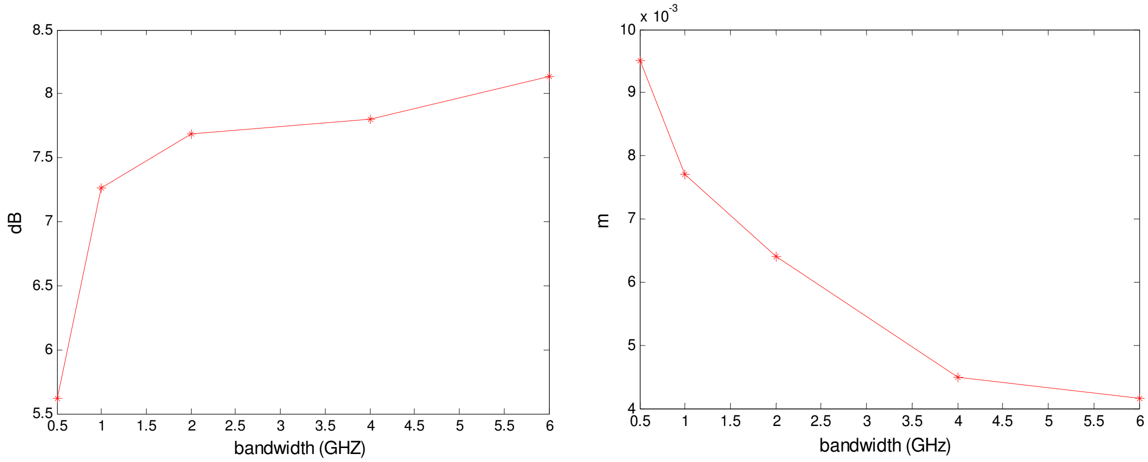

Figure 4.7: Analysis for S/C and resolution: (a) Within-breast S/C for bandwidth of 0.5, 1, 2, 4 and 6 GHz, (b) Resolution for bandwidth of 0.5, 1, 2, 4 and 6 GHz.

samples is used. Specifically, a spatial sampling of approximately $0.5\lambda_{1,f_{\max}}$, that is, $N_{\mathrm{PT}} = 24$, and a frequency sampling of 20 MHz can be used without any significant degradation in terms of S/C.

Finally, the characterisation of HP procedure with respect to the uncertain knowledge of the dielectric properties of the target volume is addressed. We begin our analysis by evaluating the S/C assuming that the dielectric properties in HP procedure are equal to:

1. $\varepsilon_{r1} = 5$, $\sigma_1 = 0.2$ S/m
2. $\varepsilon_{r1} = 20$, $\sigma_1 = 0.8$ S/m

while the dielectric properties in analytical simulation remained fixed to $\varepsilon_{r1} = 10$ and $\sigma_1 = 0.4$ S/m. For both sets of values, the process of S/C calculation was repeated assuming bandwidth of 0.5, 1, 2, 4 and 6 GHz, respectively. In both cases, the S/C has only a small variation of less than 1 dB from that given in fig. 4.7(a), which refers to the matching case. However, if the dielectric properties in HP procedure do not match the dielectric properties of the analytical simulation, the inclusion is not accurately localised. Figure 4.8 shows the normalised intensity along phi=120° cut, that is, the cut containing the inclusion, when assuming the dielectric properties in HP procedure is equal to $\varepsilon_{r1} = 5$ and $\sigma_1 = 0.2$ S/m (dotted line), $\varepsilon_{r1} = 10$ and $\sigma_1 = 0.4$ S/m (continuous line), and $\varepsilon_{r1} = 20$ and $\sigma_1 = 0.8$ S/m (dashed line), respectively.

The location of the peak intensity changes significantly in all the three cases investigated here. As expected, the figure shows that the inclusion (which is indicated with the red stem) is most accurately localised when the dielectric properties used in analytical simulation are equal to those assumed in the HP procedure. Thus, the primary effect of mismatch between actual and assumed dielectric properties is a location bias. The same effect has been highlighted in [29]. It has to be stated that fig. 4.8 has been obtained using 4 GHz of bandwidth (1.5-5.5 GHz) and using an image adjusting (which consists of zero enforcing the values below 0.25 and expanding from 0 to 1 the values above 0.25).

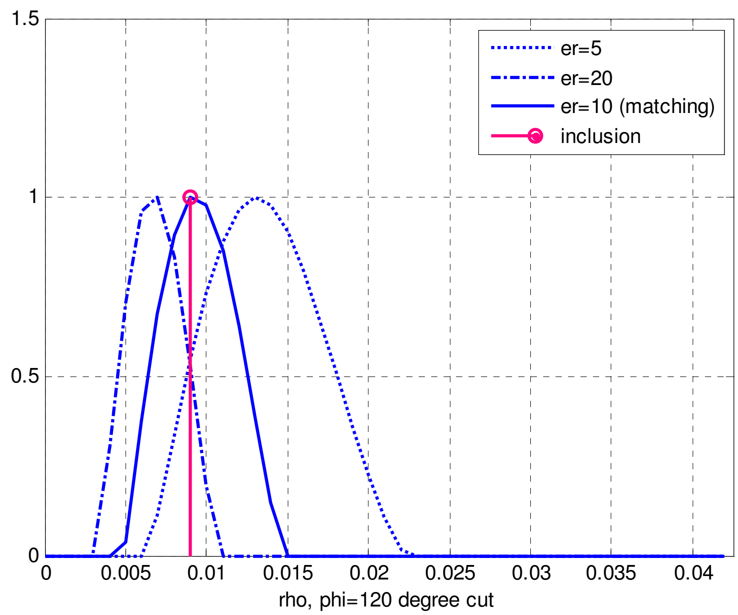

Figure 4.8: Linear normalised intensity along phi=120° cut, that is the cut containing the inclusion, when assuming the dielectric constant in HP procedure is equal to $\varepsilon_{r1} = 5$ (dotted line), $\varepsilon_{r1} = 10$ (continuous line), and $\varepsilon_{r1} = 20$ (dashed line), respectively. Inclusion (3 mm radius and positioned at 0.9 cm from the centre) is indicated with the red stem.

4.3.3 Agar-Agar Solutions with Different Conductivities

In order to investigate the effect of changing the conductivity on the quality of the image detected, let's consider a different scenario of cylinder with an inclusion. More in detail, the external cylinder is assumed to have a radius of 4.25 cm, simulating an Agar-Agar solution, which has electrical properties of $\varepsilon_{r1} = 70$ and $\sigma = 0.1$ S/m. The inclusion is assumed to be a cylindrically-shaped plastic tube with a radius of 3 mm, a radial offset of 1 cm and an angular offset of 45°, representing a more conductive Agar-Agar solution, which has the same $\varepsilon_{r1} = 70$ but a higher conductivity of $\sigma = 2$ S/m. Three illuminating sources are considered, while the frequency band spans from 1 to 3 GHz with a sampling rate of 10 MHz. Then, for each source and each frequency, the field on the external surface $E^{\text{known}}_{np,\text{tx}_m}$ is calculated. For the purpose of removing the transmitter image, HP is applied as in eq. (4.6). Figure 4.9 shows the linear normalised intensity, a peak can be clearly detected in the region of the inclusion.

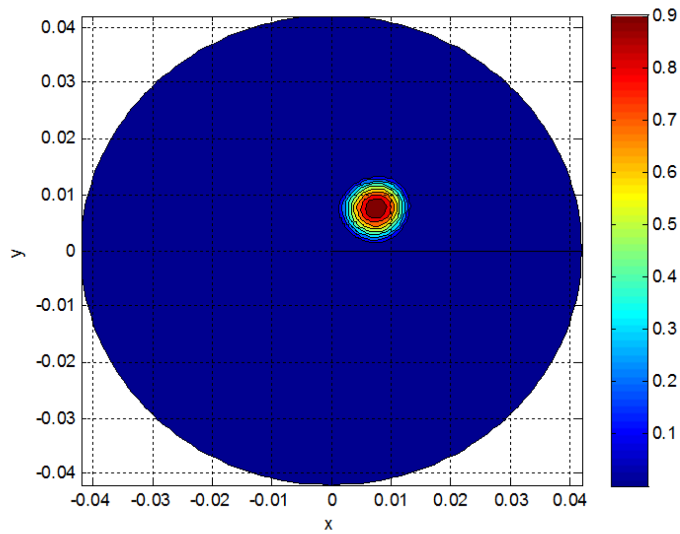

Figure 4.9: Linear normalised intensity when going from a less conductive medium into a medium with higher conductivity.

A similar simulation is performed afterwards, the only difference being that this time the outer cylinder is filled with an Agar-Agar solution of higher conductivity (i.e. $\sigma = 2$ S/m), while the inclusion (plastic tube) was filled with Agar-Agar solution with original conductivity value of $\sigma = 0.1$ S/m. HP is applied through eq. (4.6), and the linear normalised intensity image is shown in fig. 4.10.

Again, the inclusion can be detected and located at its correct position. Two mirror images with a much lower intensity can be seen at 165° and 285° with respect to the x-axis, which are due to the 120° symmetry of the illuminating sources. They can be easily removed by breaking this symmetry or by raising the threshold when adjusting the image.

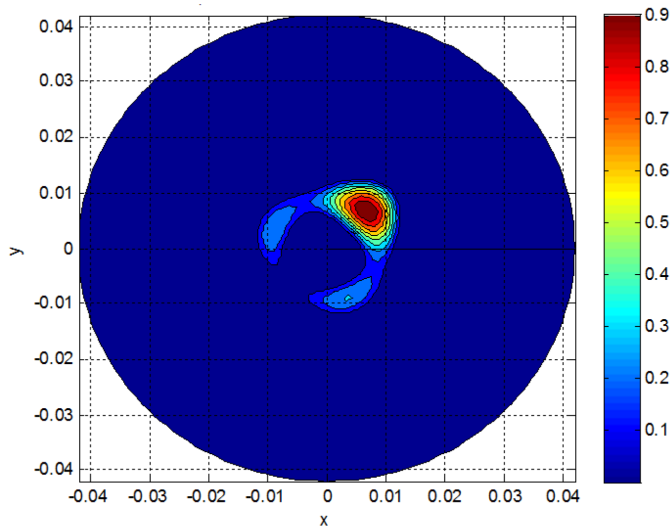

Figure 4.10: Linear normalised intensity when going from a more conductive medium into a medium with lower conductivity.

4.3.4 Cylinder with Multiple Inclusions

4.3.4.1 Identical inclusions

An important test for any imaging algorithm would be to check whether it could detect multiple inclusions within a particular medium. Previous simulation results have already shown the capability of the method in capturing and locating a single inclusion. To verify the detection of multiple inclusions using the HP procedure, an external Agar-Agar cylinder in free space having a radius of 4.25 cm, with electrical properties (frequency independent for the moment) of $\varepsilon_{r1} = 70$ and $\sigma_1 = 0.2$ S/m, with inclusions is considered. Three identical inclusions, all having a radius of 3 mm, dielectric constant $\varepsilon_{r2} = 70$, and conductivity $\sigma_2 = 2$ S/m are situated 2 cm away from the centre of the cylinder, and at angular offset of 0°, 60° and 120° relative to the x-axis respectively.

The external cylinder is illuminated using 4 transmitter sources situated 8 cm from the centre of the cylinder, while a frequency band of 1-2 GHz with frequency spacing of 5 MHz is used. For each illuminating source and for each frequency, the field at $N_{\mathrm{PT}} = 120$ points lying on the external surface is calculated. The number of points used leads to a spatial sampling of approximately $0.1\lambda_{1,f_{\max}}$. Finally, the average of the 4 data sets is calculated and HP is applied to the difference between the measured field and the average field as stated in eq. (4.6). Figure 4.11 shows the linear normalised intensity obtained using an appropriate image adjusting. Three peaks can be clearly detected in the regions of the inclusions; thus, both detection and localisation are achieved for this multi-inclusion problem [79].

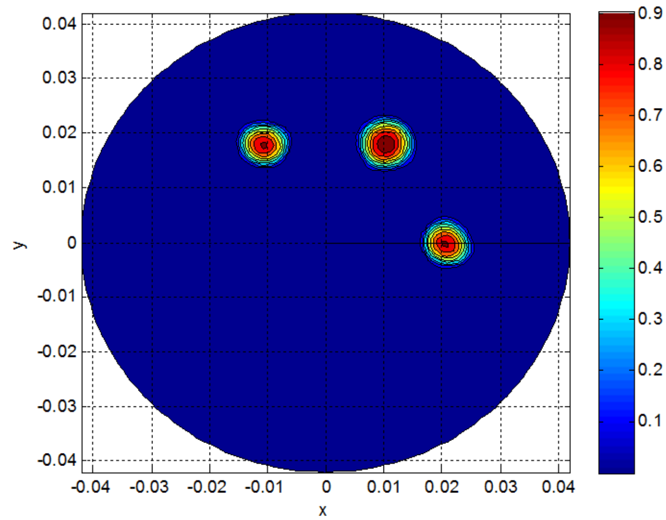

Figure 4.11: Linear normalised intensity , when considering outside cylinder with parameters $\varepsilon_{r1} = 70$, $\sigma_1 = 0.2$ S/m, and inclusions with parameters $\varepsilon_{r2} = 70$, $\sigma_2 = 2$ S/m. x and y axes are in metres.

4.3.4.2 Realistic inclusions

The ability of the method in detecting multiple identical inclusion inside a medium was investigated in the previous simulation. Next, in order to consider a more realistic scenario, the electrical properties of human body tissues are assigned to the inclusions. This time, an external cylinder with radius 4.25 cm, dielectric constant $\varepsilon_{r1} = 10$ and conductivity $\sigma_1 = 0.4$ S/m is considered. Values of ε_{r1} and σ_1 are chosen to represent the properties of normal human breast tissue [29]. Three eccentrically placed cylindrically-shaped inclusions with radii of 3 mm, placed 2 cm from the centre and with phi offsets equal to 0°, 60° and 120°, respectively, are considered. The inclusion at phi offset of 0°, with $\varepsilon_{r21} = 50$ and $\sigma_{21} = 5$ S/m represents a malignant breast tissue [29], while the one with 60° offset is assigned the properties of breast fat, $\varepsilon_{r22} = 4.65$ and $\sigma_{22} = 0.35$ S/m [48]. Lastly, the third inclusion, with 120° offset is assigned the properties of cartilage, i.e. $\varepsilon_{r23} = 33.6$ and $\sigma_{23} = 4.1$ S/m [48]. The same frequency range, sampling value, transmitting sources and other conditions as the previous simulation are implemented here. Figure 4.12 shows the normalised intensity obtained through eq. (4.4) and using an image adjusting and averaging. Three peaks can be clearly detected in the regions

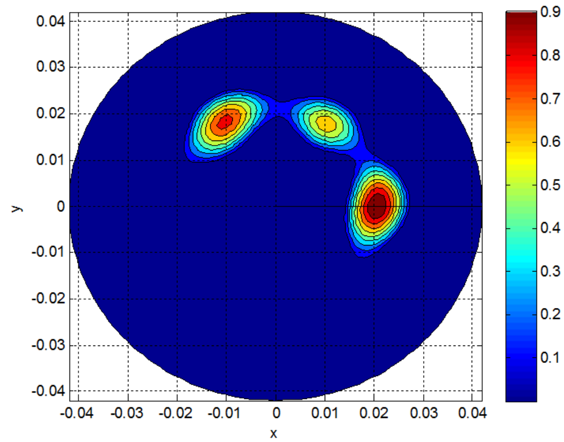

Figure 4.12: Linear normalised intensity obtained through eq. (4.4), when considering outside cylinder with parameters $\varepsilon_{r1} = 10$, $\sigma_1 = 0.4$ S/m, and inclusions with parameters $\varepsilon_{r21} = 50$, $\sigma_{21} = 5$ S/m at 0°, $\varepsilon_{r22} = 4.65$, $\sigma_{22} = 0.35$ S/m at 60° and $\varepsilon_{r23} = 33.6$, $\sigma_{23} = 4.1$ S/m at 120°. x and y axes are in metres.

of the inclusions. However, by looking closely at the resulting intensity figure it can be seen that the inclusions are detected with different intensities, such that the inclusion with higher conductivity (malignant breast tissue) is more intense than the other two. Thus, it can be concluded that the detection of the malignant tissues will be achieved in nearly all cases, as it has a conductivity value higher than most human tissues [48].

4.4 Measurement Results

4.4.1 Cylinder with an Inclusion

A series of experiments were performed to verify that the HP can detect and locate an inclusion from measured data. Similar to the MM chapter, a cast P.M.M.A. cylinder with dielectric constant of $\varepsilon_{r1} = 2.7$, conductivity of $\sigma_1 = 3 \times 10^{-7}$ S/m, and a radius of 4.25 cm and height of 30 cm was used as the first test medium. The cylinder has an eccentric inclusion consisting of a PEC cylinder with a radius of 3 mm; the distance between the centres of the two cylinders is approximately 2.1 cm (fig. 3.7).

Frequency-domain UWB measurements in an anechoic chamber were performed using a VNA arrangement to obtain the transfer function at 1601 discrete frequencies in the band of 6-10 GHz ($\Delta_f = 2.5$ MHz); this measurement only used the nominal output power level of the VNA (2 mW). Wideband bow-tie antennas, vertically polarised and omni-directional in the azimuth plane were used, after calibration and a careful check of S_{11} parameters (fig. 3.8). A careful adjustment was done for both antennas to be in vertical position to avoid any polarisation mismatch. For each set of measurements, the location of the transmitting antenna was fixed at approximately 20 cm away from the centre of the cylinder, while the receiver antenna was positioned close to the external surface of the cylinder and placed on a computer-controlled rotating stage with 3° of angular resolution. Thus, the field $E^{\text{known}}_{np,\text{tx}_m}$ at $N_{PT} = 120$ equally phi-spaced points lying on the external surface was measured. A total number of $M = 12$ sets of data was recorded (with m=1, 2, ...,12), changing the position of the transmitting antenna along phi with a step of 30° [fig. 4.13(a)]. Next, the average of the 12 data sets was computed, i.e. $(\text{avg}_M\{E^{\text{known}}_{np,\text{tx}_m}\})$ and HP was applied to the difference between the measured field and the average field as stated in eq. (4.5). Figure 4.13(b) shows the normalised intensity (linear) obtained using eq. (4.3) after a proper image adjusting. A peak can be clearly detected in the region of the inclusion, which is at approximately 270° relative to the x-axis.

Again, by looking at the figure, it can be observed that the resolution (i.e. the dimension of the region whose normalised intensity is above 0.5) is approximately 4.5 mm. Previously, it was stated that the optical resolution limit should be $\lambda_{1,f_{\max}}/4$, as calculated below:

$$\lambda_{\text{air}} = \frac{c}{f_{\max}} = \frac{3 \times 10^8}{10\text{GHz}} = 0.03 \text{ m} \tag{4.7}$$

$$\lambda_{1,f_{\max}} = \frac{\lambda_{\text{air}}}{\sqrt{\varepsilon_{r1}}} = \frac{0.03}{\sqrt{2.7}} = 18.26 \text{ mm} \tag{4.8}$$

$$\lambda_{1,f_{\max}}/4 = 4.56 \text{ mm} \tag{4.9}$$

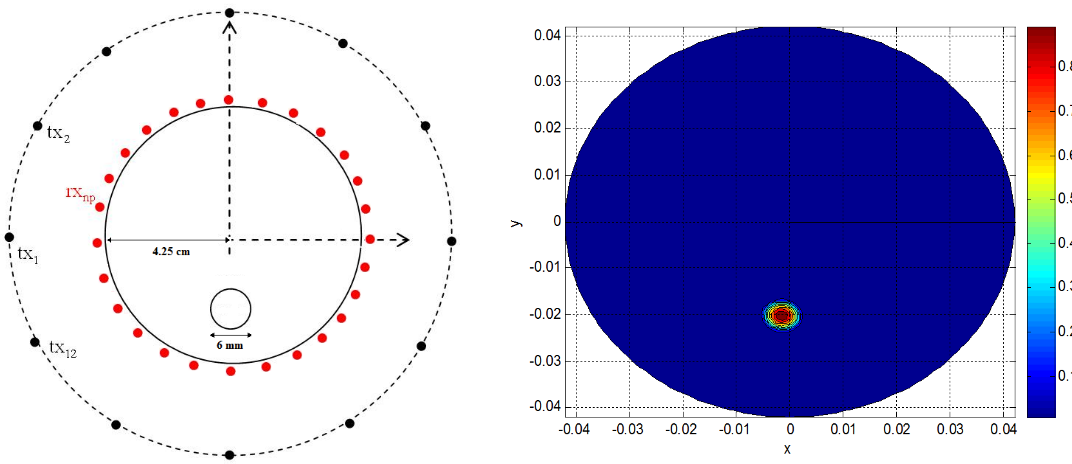

(a) (b)

Figure 4.13: (a) Pictorial view of the problem, with the red and black dots representing the receiving and transmitting positions, respectively. (b) Normalised intensity obtained through eq. (4.3); a peak can be clearly detected in the region of the inclusion. x and y axes are in metres.

Therefore the resolution achieved from performing the experiment is in agreement with the expected optical resolution limit.

The time required to perform all 12 sets of measurements is approximately 2 hours with a single network analyser, while the CPU time required by the HP procedure is approximately 10 minutes on an Intel Pentium M 2 GHz with 1 GB RAM. The high measurement time depends on the number of transmitting and receiving positions, which for this example has been set to $M = 12$ and $N_{\mathrm{PT}} = 120$, respectively. It follows that a reduction of the measurement time of a factor 5 can be achieved by reducing the number of measured points to $N_{\mathrm{PT}} = 24$. A further reduction is achievable if employing an array configuration rather than a full mechanical scanning system, yielding to a measurement time comparable to that given in [30]. The CPU time required by the HP procedure depends on the number of transmitting and receiving positions and on the number of frequency samples. Referring to section 4.3.2, it has been shown that the S/C does not vary significantly if a spatial sampling of $0.5\lambda_{1,f_{\max}}$ and a frequency sampling 20 MHz is used. It follows that a reduction of the computational time of a factor 40 can be achieved.

4.4.2 Agar-Agar Cylinder with Inclusion

After achieving successful and promising results by applying the HP on P.M.M.A. made cylindrical object, the next step was to focus on more realistic human tissue-like example. To achieve this goal, a cylindrical container (plastic cup) with radius of 4.2 cm was filled with Agar-Agar gel, mimicking a high-water-content human tissue. A small PEC cylinder with a radius of 1 mm, representing a tumour was positioned inside the Agar-Agar gel, at a distance of 1 cm from the centre of the cylinder. Furthermore, the thin layer of the plastic cup can be viewed as representing the skin layer covering the tissue simulant.

The Agar-Agar was dissolved in hot water at approximately 95°C and then cooled down to room temperature, to form a semi-transparent gel. The dielectric constant and the conductivity are functions of the concentration of the Agar-Agar [52]; for this experiment, an Agar-Agar substance with approximately 6% concentration (by weight) in water was used, leading to $\varepsilon_{r1} = 70$ and $\sigma_1 = 1$ S/m at 1GHz. By comparing these values with those given in [48], it can be noted that the dielectric constant and the conductivity of the Agar-Agar can be used to simulate the actual dielectric properties of human tissues. It is important to point out that the loss in Agar-Agar is even greater than that encountered in some human tissue imaging problems. Therefore, it follows that the example here presented can be considered representative of lossy media imaging problems.

To couple the microwave energy into the Agar-Agar cylinder more efficiently, both transmitting and receiving antennas are placed in a matching medium. Here, for simplicity, water has been used as a matching medium as sketched in fig. 4.14.

After cooling down, the Agar-Agar cylinder was positioned inside a circular container having radius of 20 cm and filled with water. (see fig. 4.15). Frequency domain UWB measurements were performed inside an anechoic chamber, using a VNA arrangement to obtain the corresponding transfer function. Discone antennas, vertically polarised and omni-directional in the azimuth plane were used, after calibration.

It was important to analyse the transfer function of the receiver with respect to the trans-

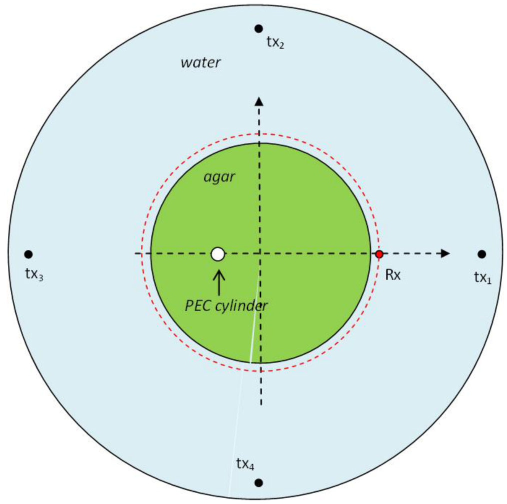

Figure 4.14: Pictorial view of the problem, with the red and black dots representing the receiving and transmitting positions, respectively.

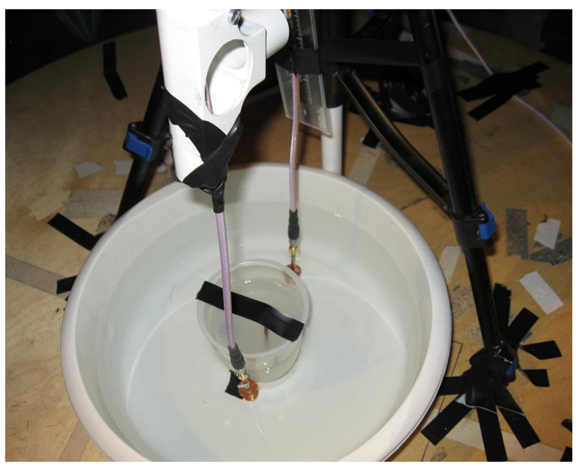

Figure 4.15: Measurement setup, Agar-Agar solution inside water.

mitter, S_{21}, in order to get an idea of the appropriate frequency band to be used. The frequency range of 1-3 GHz was chosen for the experiment, as higher frequencies would cause very high losses due to the high conductivity of water. Figures 4.16 and 4.17 show the magnitude of S_{21} for the frequency range of 1-3 GHz at the nearest and farthest point between the two antennas, respectively.

It can be observed that, the amplitude of S_{21} for the longest path falls below the noise level (-70 dB) for $f > 1.6$ GHz. This measurement only used the nominal output power level of the VNA (2 mW), and hence only the frequency band 1-1.6 GHz was used, recording the transfer

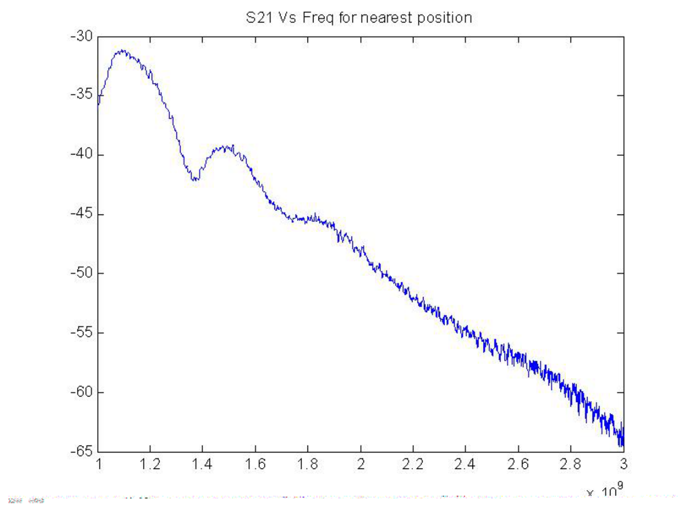

Figure 4.16: Magnitude of S_{21} for the frequency range 1-3 GHz for the nearest point.

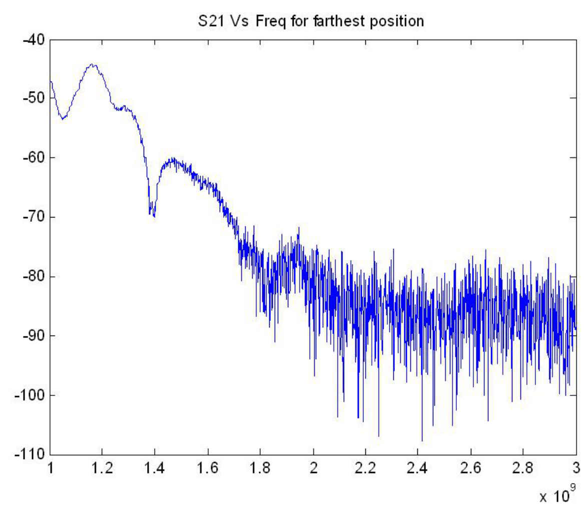

Figure 4.17: Magnitude of S_{21} for the frequency range 1-3 GHz for the farthest point.

function at 1601 discrete frequencies (frequency sampling $\Delta f = 0.375$ MHz). Obviously, the upper frequency limit can be increased when a matching liquid with lower losses is used or if a proper amplifier is introduced in the measurement system (subject to clinical power-level considerations).

For each set of measurements, the location of the transmitting antenna was fixed at a distance of approximately 15 cm away from the centre of the cylinder, while the receiver antenna was positioned close to the external surface of the Agar-Agar cylinder and mounted on a computer-controlled rotating stage with 3° of angular resolution. Then, the field $E^{\text{known}}_{np,\text{tx}_m}$ at

N_{PT}=120 equally phi-spaced points lying on the external surface was measured; again, the number of points leads to a spatial sampling of approximately $0.1\lambda_{1,f_{\max}}$, where $\lambda_{1,f_{\max}}$ represents the wavelength inside the Agar-Agar cylinder calculated at the highest frequency of 1.6 GHz. In total, 4 data sets (M=4) were recorded, by changing the position of the transmitting antenna along the azimuth plane with a step of 90° (see fig. 4.14). Next, the average of 4 sets was computed, using $\text{avg}_M\{E^{\text{known}}_{np,\text{tx}_m}\}$ and HP was applied through eq. (4.5). Figure 4.18 shows the linear normalised intensity, it can be seen that, a peak has been clearly detected in the region of the inclusion, and hence both detection and localisation of the inclusion have been achieved.

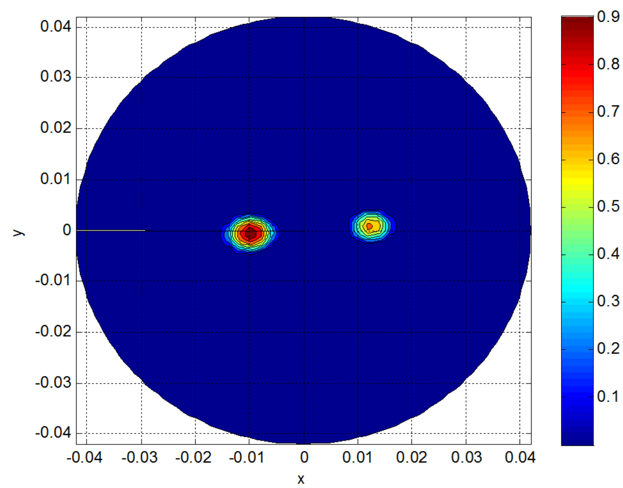

Figure 4.18: Normalised intensity (linear), when using 4 illuminating sources and the band 1-1.6 GHz. x and y axes are in metres.

By exploring the figure, another spot having approximately the same intensity can be detected; this corresponds to the "mirror image" of the object with respect to the y-axis and is due to the ambiguity introduced by the symmetry in the position of the illuminating sources used in the measurements. However, further investigation on the experimental data showed that this artefact could be removed by increasing the number of illuminating sources, or alternatively by breaking the symmetry of the 4 illuminating sources. In this context, in order to remove the ghost image, the same experiment was repeated using only 3 illuminating sources (M=3), with a transmitting step of approximately 120°. The resulting image is shown in fig. 4.19; it can be seen that the false image has successfully been removed. This is due to the fact that when

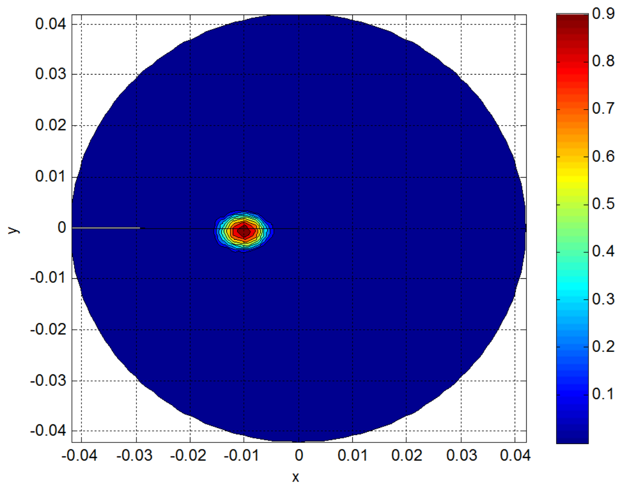

Figure 4.19: Normalised intensity (linear), after breaking the symmetry of the illuminating sources. x and y axes are in metres.

using M=4, two of the transmitting positions (0° and 180° with respect to x-axis) will be on the same axis as the inclusion, causing quadrantal symmetry, resulting in the presence of a mirror image. The figure also shows that the resolution of the image is approximately 5 mm; again, this value is in agreement with the optical resolution limit of $\lambda_{1,f_{\max}}/4$. In general, it will be realised that a measurement regime can be adopted which avoids any ambiguities (non-unique solutions) by breaking any symmetry in the transmitter and receiver positions. Moreover, it can be shown that the minimum number of M=3 illuminating sources is required to smear out the transmitter image [see eq. (4.5)].

4.4.3 Cylinder with Multiple Inclusions

Here, to assess the applicability of HP in solving more complex problems, the measurement in 3.3.2 (fig. 4.20) was repeated, this time applying the HP for the purpose of reconstruction. In brief, a P.M.M.A. cylinder ($\varepsilon_{r1} = 2.7$, $\sigma_1 = 3 \times 10^{-7}$ S/m) with two inclusions was considered; the cylinder has an eccentric inclusion consisting of a PEC cylinder with a radius of 3 mm, and in addition, a second inclusion was emplaced by drilling a 3 mm radius hole at 90° (relative to centre) from the PEC and filling it with an Agar-Agar solution. The distance between the axis of each inclusion and that of the outer cylinder is approximately 2.1 cm.

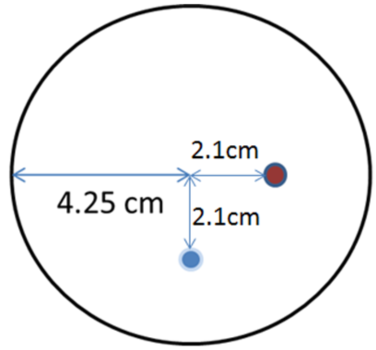

(a) (b)

Figure 4.20: (a) Cast P.M.M.A. cylinder having a radius of 4.25 cm with PEC and Agar-Agar solution inclusions. (b) Pictorial view of the problem, with the dark and light circles representing the PEC and Agar-Agar solution inclusions, respectively.

Frequency-domain UWB measurements in an anechoic chamber were performed, using a VNA arrangement to obtain the transfer function at 1601 discrete frequencies in the band of 6-8 GHz. Wideband bow-tie antennas, vertically polarised and omni-directional in the azimuth plane, were used. For each set of measurements, the location of the transmitting antenna was fixed at approximately 20 cm away from the centre of the cylinder, while the receiver antenna was positioned close to the external surface of the cylinder and placed on a computer controlled rotating stage with 3° of angular resolution. Thus, the field $E^{\text{known}}_{np,\text{tx}_m}$ at N_{PT}=120 equally phi-spaced points lying on the external surface were measured. A total number of M=6 sets of data were recorded (with m=1, 2, ..., 6), changing the position of the transmitting antenna along phi with a step of 60°. Next, the average of the six sets was computed, and HP was applied. Figure 4.21 shows the linear normalised intensity obtained through eq. (4.3) after a proper image adjusting. Two peaks can be clearly detected in the region of inclusions, with different intensities. Specifically, the peak with the higher intensity corresponds to the PEC cylinder (due to the fact that a greater contrast, i.e. greater mismatch boundaries, occurs when going from P.M.M.A. to PEC cylinder), while the less intense peak represents the location of the Agar-Agar solution cylinder. Hence, both detection and localisation are achieved, showing the ability of the methodology in resolving multiple scatterers and paving the way for addressing problems involving tissue inhomogeneities as well.

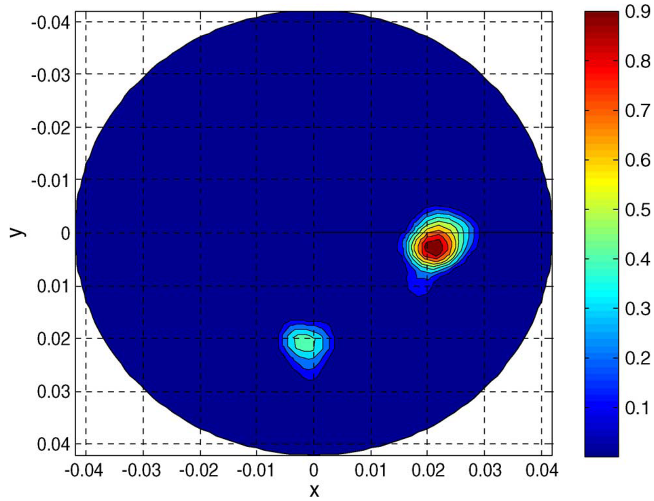

Figure 4.21: Normalised intensity (linear). Two peaks can be clearly detected in the region of the inclusions. x and y axes are in metres.

4.4.4 3D Measurements (Sphere)

From the previous examples, it follows that the proposed HP-based procedure can capture the contrast in order to detect and locate an inclusion. Using HP to forward-propagate the wave removes the need to solve any inverse problem, thus no matrix generation/inversion is required. Moreover, extension to more realistic 3D geometries is straightforward. In fact, for a given 3D object, the field $E_{np,\mathrm{tx}_m}^{\mathrm{known}}$ can be determined in the external surface, and eq. (4.6) can be applied to forward propagate the field in order to construct the corresponding image. The 3D extension has been validated through measurements. In particular, a cast P.M.M.A. sphere with a radius of 6 cm, dielectric constant value of $\varepsilon_{r1} = 3.45$ and conductivity value equal to $\sigma_1 = 3 \times 10^{-7}$ S/m has been considered. An inclusion consisting of a PEC cylinder having a radius of 3 mm and a height of 6 mm was positioned inside the sphere by drilling it, putting the PEC cylinder into the hole, and refilling the hole with liquid P.M.M.A. having dielectric properties similar but not equal to those of the sphere. Figure 4.22 gives two pictorial views of the sphere used in the measurements.

Figure 4.22: Cast P.M.M.A. sphere having a radius of 6 cm with PEC eccentric inclusion.

Frequency-domain UWB measurements in an anechoic chamber were performed; the VNA was adjusted to obtain the transfer function at 1601 discrete frequencies in the range of 6-10 GHz, with a frequency sampling of $\Delta f = 2.5$ MHz. Wide-band discone antennas, vertically polarised and omni-directional in the azimuth plane were used, after calibration. A careful adjustment was done for both antennas to be in vertical position to avoid any polarisation mismatch. To observe the radiation pattern of the discone antenna over the frequency range of 1-10 GHz when no object is present, the S_{21} magnitudes between the transmitting and receiving antennas at their nearest point (15 cm) and farthest point (25 cm) are shown in figs. 4.23(a) and 4.23(b), respectively.

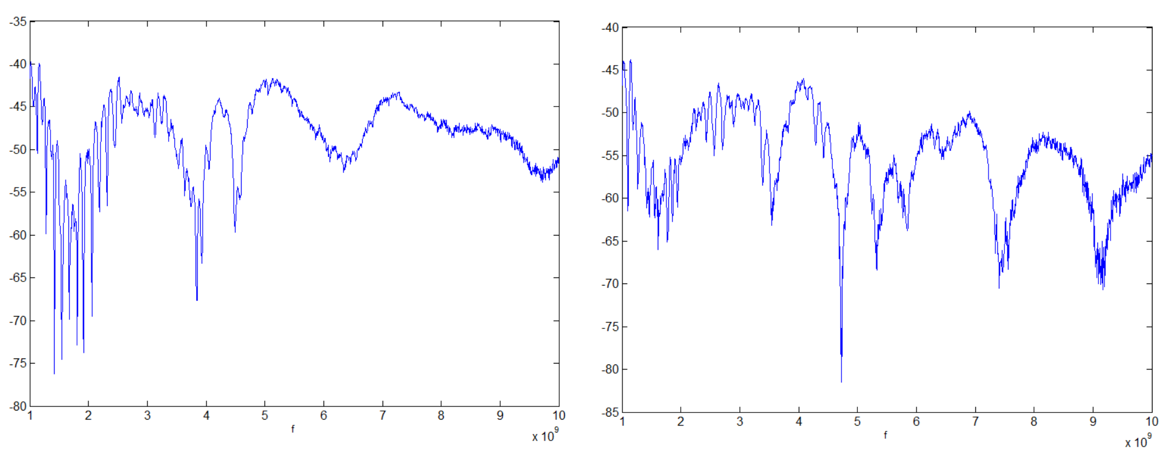

(a) (b)

Figure 4.23: Logarithmic magnitude of S_{21} over the frequency range 1-10 GHz for (a) the nearest point (∼15 cm), (b) farthest point (∼25 cm).

A large variation over the frequency range can be seen, along with occasional dips which correspond to the frequencies which do not include any usable information; however this does not have an impact on the measured result as this effect is normalised and the unwanted frequencies will be naturally excluded by the algorithm.

For each set of measurements, the location of the transmitting antenna was fixed at approximately 20 cm away from the centre of the sphere, while the receiver antenna was positioned close to the external surface of the sphere and placed on a computer-controlled rotating stage with measurements taken at intervals of 3° (fig. 4.24).

In total, 8 sets of measured data $E_{np,\mathrm{tx}_m}^{\mathrm{known}}$, were recorded. Each set of measurements differed from the previous ones, as 8 equally spaced equatorial planes were used to record the measurements, whilst keeping both antennas in vertical positions with respect to such planes. For simplicity, in order to produce measurements along 8 different equally spaced equatorial planes, the sphere was rotated with respect to the x-axis, while the data was recorded in the same xy-plane (fig. 4.25).

Finally, the average of the 8 sets was computed, and HP was applied as indicated in eq. (4.6). Figures 4.26(a) and 4.26(b) show views of the normalised intensity of the resulting field in which a peak can be clearly detected in the region of the inclusion. Looking at the figures, a region of dark-red areas can be observed surrounding the peak. This area can be attributed to the difference in dielectric properties between the P.M.M.A. of the sphere and the liquid P.M.M.A. used to refill the hole.

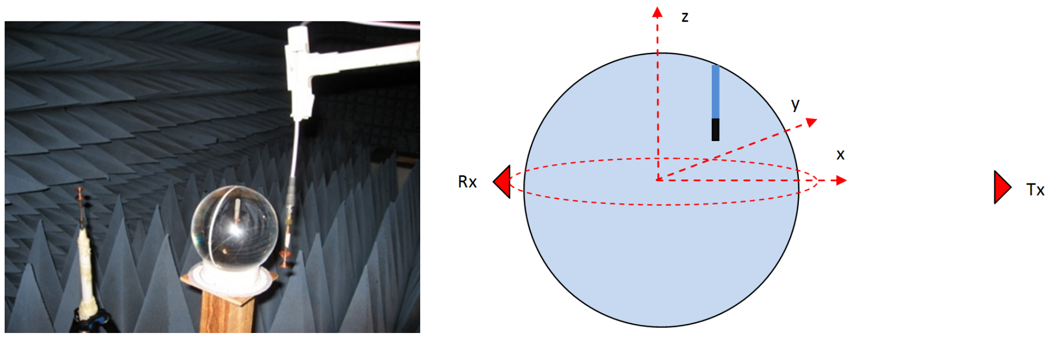

(a) (b)

Figure 4.24: (a) Measurement equipment. (b) pictorial view of the problem, with the circumference lying on the xy-plane representing the equatorial plane where the measures are recorded.

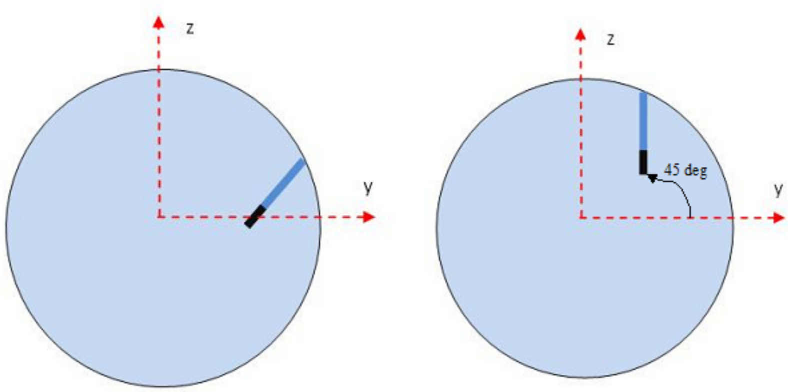

Set 1 Set 2

Figure 4.25: To reproduce 8 sets of measurements along different equatorial planes, between each set of measurements the sphere is rotated by 45° with respect to z-plane, while the measurements are recorded on the same xy-plane.

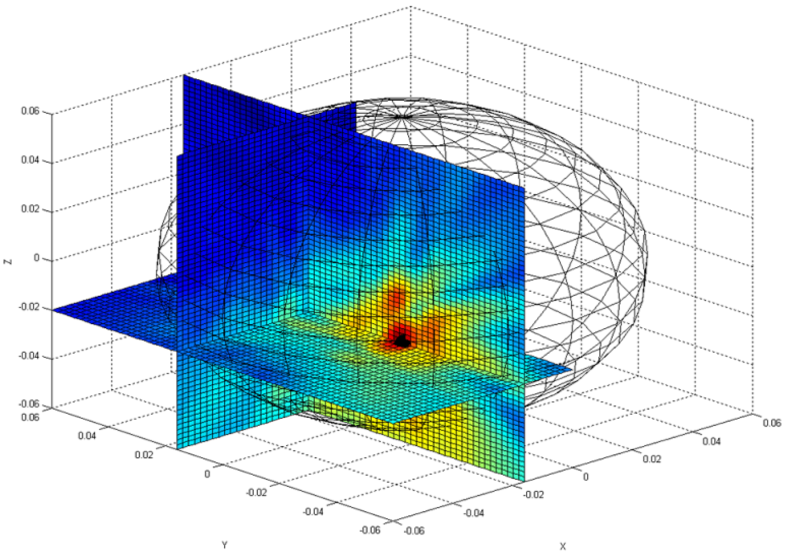

(a)

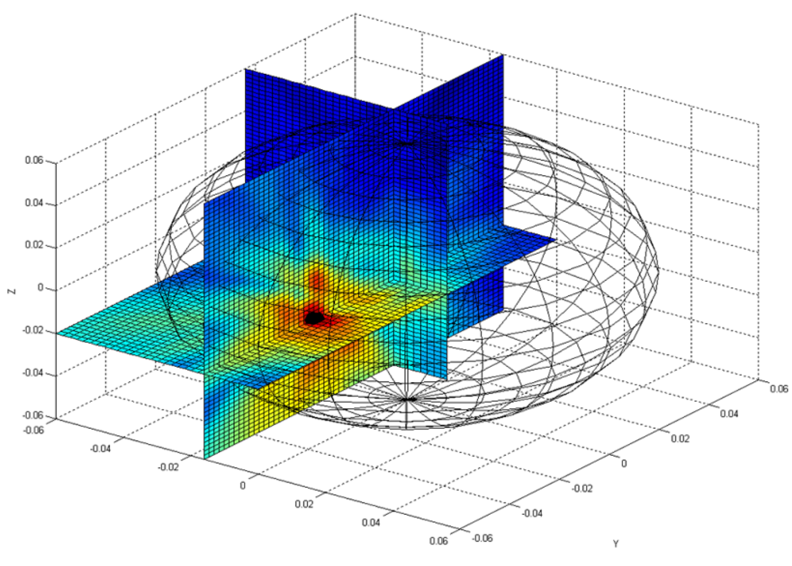

(b)

Figure 4.26: Linear normalised intensity obtained through eq. (4.4), (a) view1, (b) view2; a peak can be clearly detected in the region of the inclusion; x and y axes are in metres.

4.5 Summary

A novel microwave imaging procedure based on the Huygens principle has been introduced and analysed. Using the HP procedure to forward-propagate the waves removes the need to solve inverse problems, and unlike the MM approach, which can be referred to as a special case of the HP based technique for a sophisticated Green's function employing higher order Bessel functions, no matrix generation/inversion is required.

The method allows all the information in the frequency domain to be utilised by combining the information from the individual frequencies to construct a consistent image. Initial simulation and measurement results indicate that this feature is capable of producing as good or better performance when compared to similar examples in conventional time-domain approaches; specifically, the S/C reaches 8 dB. The procedure is robust to uncertainties in the medium, and it is capable of resolving multiple scatterers as well, with a resolution of approximately one quarter of the shortest wavelength in the dielectric medium. The power levels used are well within safety limits, while the bandwidths satisfy the UWB rule of being at least 20% of the centre frequencies. It follows that the methodology permits the detection and location of significant scatterers inside a volume.

Validation of the techniques through both simulations and measurements have been performed and presented, illustrating the effectiveness of the methods. It is worthwhile pointing out that the S/C given in fig. 4.7(a) has been calculated using simulated, i.e. noiseless data. A slight decrease in S/C can be observed when using measurement data. However, this decrease does not affect the detection and localisation, as gathered from measurement result sections.

The next two chapters of this thesis will focus on the extension of HP to more complex and realistic geometries. In chapter 5, application of HP on multilayered cylindrical mediums will be investigated both analytically and through simulations/measurements; while in chapter 6, further extension of the methodology to three-dimensional phantoms with realistic shape and realistic tissue architecture will be covered both through FDTD simulations and measurements, which will permit the exploitation of the potential of the new methodology when applied to realistic medical imaging problems.

5

Modelling Multilayered Media With Inclusions

5.1 Introduction

This chapter covers the extension of the HP technique, introduced in chapter 4, to more realistic geometries constituting multiple layers. Using HP to forward propagate the waves removes the need to solve inverse problems and, consequently, no matrix generation/inversion is required. In addition to its simplicity, the methodology permits the capture of contrast, to the extent in which different materials with different properties within the region of interest can be discriminated in the final image. It follows that the methodology can identify the presence and location of significant scatterers inside a volume, without having a'priori knowledge on the dielectric properties of the target object. Thus, due to all the mentioned advantages of the HP, it has been chosen as the desired technique to be used for the rest of this thesis.

Here, in contrast to conventional approaches based on FDTD methods, the propagation of UWB signals in human tissue will be investigated analytically. The human body will be modelled as 3-layer concentric and eccentric cylinders of infinite length, and Maxwell's equation will be solved. The analytical results from section 2.8 will then be used to simulate realistic examples involving 3 cylindrical layers. Validation of the technique through measurements on multilayered cylindrical objects with inclusion has also been performed.

This chapter is organised as follows: In the next section, the procedure is verified through realistic simulations involving 3-layer cylindrical mediums, based on solution of Maxwell's equation for 3-layer stratified concentric and eccentric cylindrical models, formulated in sections 2.7 and 2.8. Then, in the last section the validation of the method through measurements on a 4-layer cylinder with an inclusion is given.

5.1.1 Simulation Results: Multilayered Object with an Eccentric Inclusion

Before proceeding to perform an experiment, we used the analytical formulation of section 2.8 to verify the applicability of HP in a multilayered configuration. Specifically, an external Agar-Agar cylinder in free space having a radius of 4.25 cm, with electrical properties (frequency independent for the moment) of $\varepsilon_{r1} = 70$ and $\sigma_1 = 0.5$ S/m, with inclusions is considered. A smaller cylinder of radius 3 cm, with the same dielectric constant value but a higher conductivity value $\sigma_2 = 2$ S/m is placed inside the outer cylinder to represent the second medium. Finally, an eccentric inclusion made of a PEC cylinder of radius 3 mm, is placed 1.75 cm away from the axis of the cylinder, 90° relative to the x-axis.

The external cylinder is illuminated using 4 transmitter sources situated 8 cm from the axis of the cylinder, while a frequency band of 1-3 GHz with frequency spacing of 10 MHz is used. For each illuminating source and for each frequency, the field $E_{np,\mathrm{tx}_m}^{\mathrm{known}}$ at $N_{\mathrm{PT}} = 120$ points lying on the external surface is calculated. It should be noted that in this example, $E_{np,\mathrm{tx}_m}^{\mathrm{known}}$ has been determined using the analysis presented in section 2.8. Finally, the average of the 4 data sets is calculated and HP is applied to the difference between the measured field and the average field as stated in eq. (4.6). Fig 5.1 shows the normalised intensity obtained through eq. (4.4) and using an appropriate image adjusting. The image is adjusted by enforcing to zero the intensity values below 0.5 and expanding from 0 to 1 of the values above 0.5. A peak can be clearly detected in the region of the inclusion; thus, both detection and localisation are achieved for this multilayered problem.

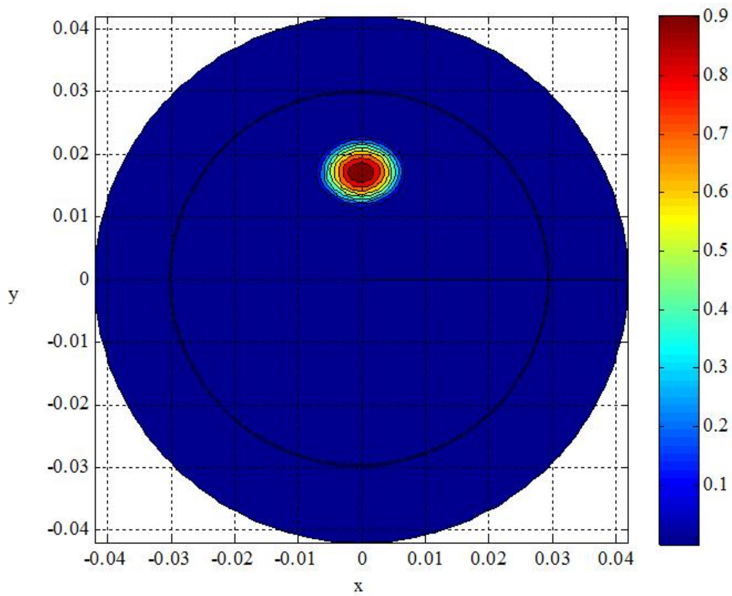

Figure 5.1: 3-layer cylinder with an inclusion: linear normalised intensity obtained through eq. (4.4). x and y axes are in metres.

Next, a similar geometrical model, this time with realistic human body tissue properties assigned to its 3 layers is further simulated. The external cylinder is assumed to be a thin human skin with radius 4.25 cm, $\varepsilon_{r1} = 41$ and $\sigma_1 = 0.9$ S/m [29]. The internal concentric cylinder and the eccentric inclusion are then assigned the electrical properties of a normal ($\varepsilon_{r2} = 10$ and $\sigma_2 = 0.4$ S/m) and malignant ($\varepsilon_{r3} = 50$ and $\sigma_3 = 5$ S/m) tissue respectively. The inclusion with a radius 3 mm, is placed 1.5 cm away from the axis of the cylinder, 90° relative to the x-axis. In the simulation, the radius of the middle cylinder is increased to 4.05 cm in order to have a thin skin layer of only 2 mm, while the sizes of other layers remain unchanged. The values of frequency range and sampling, and the number of transmitting and receiving sources also remain the same as the previous simulation. Figure 5.2(b) shows the normalised intensity obtained through eq. (4.4) and using an appropriate image adjusting and averaging. It is important to point out that in both multilayered simulation, the quantity k_2 is used instead of k_1 in the Green's function for the reconstruction process. This is due to the fact that the target is now contained in the second layer. The use of k_1 too results in the detection of the inclusion at its correct angular position, but in such case a slight decrease in the resolution and an offset of 2 mm in the positioning of the inclusion with respect to the axis is noticed.

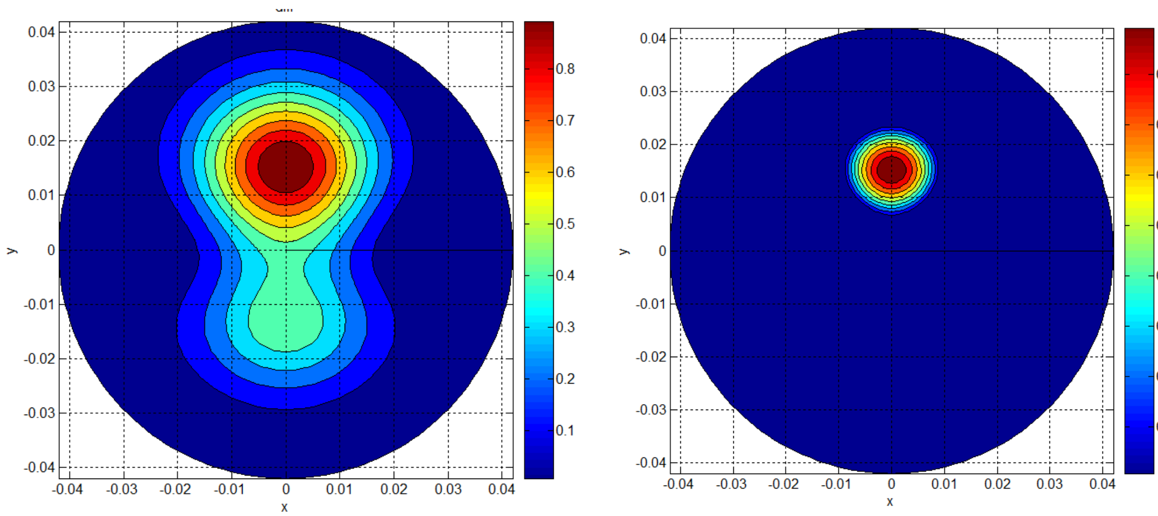

(a) (b)

Figure 5.2: 3-layer cylinder with human tissue properties. Linear normalised intensity obtained through eq. (4.4): (a) before image adjusting, (b) after image adjusting. x and y axes are in metres.

A peak can be clearly detected in the region of the inclusion. It can be seen that the method successfully detects and locates the breast tumour in this multilayered simulation, and knowing that malignant breast tissue has a conductivity value higher than most human tissues [48], its detection will be achieved in nearly all cases.

Next, an analysis of the S/C and resolution with respect to the band is performed. To evaluate the S/C with respect to the band, we apply eq. (4.3) for different bandwidths; more in detail, we perform image reconstruction assuming a bandwidth of 1, 2, and 4 GHz (the lower frequency is fixed at 1 GHz). Next, for each image the S/C is calculated and reported in table 5.1. Note that in HP procedure the within-breast S/C approaches 4 dB for a bandwidth of 4 GHz. This value has been obtained with M=4 transmitter positions, N_{PT}=120, and a frequency sampling of 20 MHz. It should be noted that since no mirror image is present in this case, M=4 has been used in order to achieve a better S/C. Use of M=3 too results in the detection and localisation of the inclusion, but with a slight decrease in S/C. Further details concerning the variation of S/C with respect to M, N_{PT} and frequency sampling has been presented in chapter 4 [63]. In the same chapter, it has been shown that an increase of approximately 4 dB occurs if using M=12. It should be pointed out that in [27], for a similar problem of 4 GHz bandwidth, a within-breast S/C of 4.1 dB has been obtained by employing the delay-and-sum beamforming algorithm and using M =45, while in [32] a within-breast S/C of 4 dB has been obtained by employing time-reversal approach and using M=7. Note that in both [27] and [32], the skin has also been considered.

Resolution, i.e. the dimension of the region whose normalised intensity is above 0.5, has been addressed with respect to the band. Specifically, in table 5.1 the resolution is given assuming a bandwidth of 1, 2 and 4, respectively. It has been shown (see table 5.1) that the resolution achieves the optical resolution limit of $\lambda_{f_{\max}}/4$; this value is comparable to that achieved by time-reversal approach [32], and by the delay-and-sum beamforming algorithm [27]. In [80], it has been shown that time-reversal approach is capable of achieving sub-wavelength resolution. A detailed analysis of computational efficiency has already been presented in the previous chapter.

Table 5.1: Within-breast S/C and Resolution for bandwidths of 1, 2 and 4 GHz.

Band (GHz)	Within-breast S/C (dB)	Resolution (mm)
1	3	7.5
2	3.5	6
4	3.9	5

5.1.2 Measurement Results: 4-layer Cylinder with an Eccentric Inclusion

To assess the practical ability of the HP method in locating an eccentric inclusion in a multilayered medium, a human tissue like model was constructed. To achieve this purpose, a 2 mm thick PVC cylindrical pipe with radius of 5 cm was concentrically placed inside a larger plastic pipe, also 2 mm thick but with a larger radius of 6.25 cm. Both pipes were filled with Agar-Agar gel approximating a high water-content human tissue; a 3mm thick PEC rod representing a tumour was positioned eccentrically inside the gel [fig. 5.3(a)], at a distance of 3.25 cm from the axis of the cylinders [fig. 5.3(b)]. Although the thickness of the pipes was chosen to be as narrow as possible (2 mm), their minimal effect on the imaging procedure could not be ignored, making this model effectively a 5-layer problem.

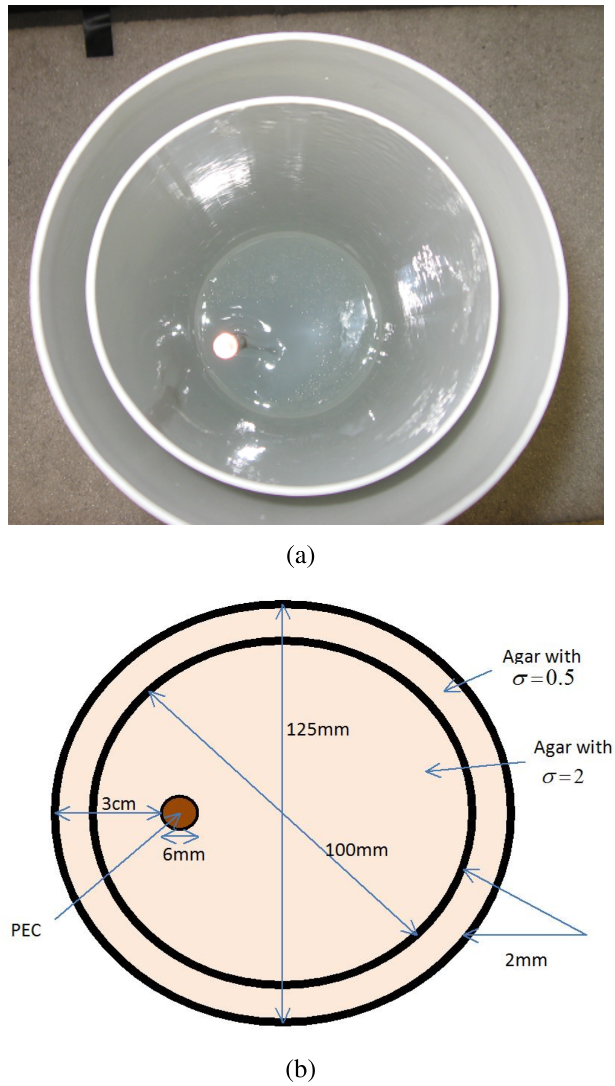

Figure 5.3: (a) Multilayered medium with an inclusion, (b) Pictorial view of the problem.

The Agar-Agar was dissolved in hot water at approximately 95°C and then cooled to room temperature to form a semi-transparent gel. The dielectric constant and the conductivity are functions of the concentration of the Agar-Agar [52]; for this experiment two distinct concentrations of Agar-Agar were used. The external plastic pipe was filled with a lower conductive Agar-Agar ($\sigma_1 = 0.5$), while the smaller plastic pipe was filled with a higher conductive Agar-Agar ($\sigma_1 = 2$). This increase in conductivity value can be gained by adding the necessary amount of salt to the original Agar-Agar mixture; By comparing these values with those given in [48], it can be noted that the dielectric constant and the conductivity of Agar-Agar are similar to the actual dielectric properties of human tissues. It is worthwhile to point out that the loss in Agar-Agar is even greater than that encountered in some human tissue imaging problems (due to higher conductivity); thus, it follows that the example here presented can be considered representative of lossy media imaging problems.

Frequency-domain UWB measurements were performed in free space, using a VNA arrangement to obtain the transfer function. Discone antennas, vertically polarised and omnidirectional in the azimuth plane were used, after calibration. In order to observe the variation of signal in different frequencies, the measurements were recorded using a large frequency range of 1-10 GHz, using a frequency step of 5.6 MHz. For each set of measurements, the location of the transmitting antenna was fixed at approximately 15 cm away from the axis of the cylinder, while the receiver antenna was positioned roughly 1 cm away from the external surface of the Agar-Agar cylinder and mounted on a computer-controlled rotating stage with 3° of angular resolution. In addition, a 30 dB amplifier was used to increase the received signal. Figure 5.4 shows the logarithmic S_{21} magnitude for the employed frequency range when the transmitting and the receiving antennas are at their farthest position.

Next, the field $E^{\text{known}}_{np,\text{tx}_m}$ at $N_{\text{PT}} = 120$ equally phi-spaced points lying on the external surface was measured; it should be noted that the employed number of points leads to a spatial sampling of approximately $0.1\lambda_{1,f_{\max}}$, where $\lambda_{1,f_{\max}}$ represents the wavelength in the cylinder calculated at the highest frequency (10 GHz). It has been shown that the number of measured points and the frequency samples can be reduced to $N_{\text{PT}} = 24$ and 20 MHz, respectively, without decreasing the detection capability [78]. Four sets of data were recorded, changing the position of the transmitting antenna along phi with a step of 90°. Next, the average of the 4 data sets

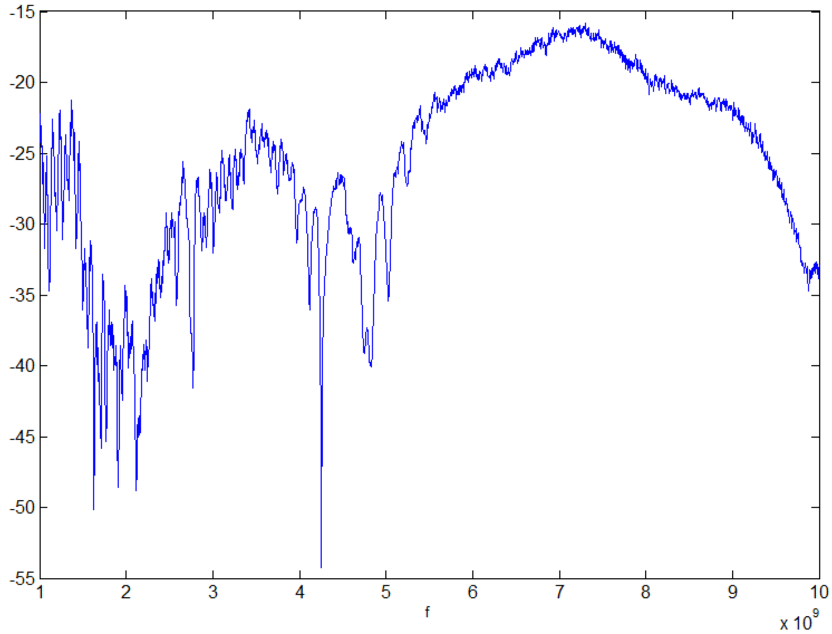

Figure 5.4: S_{21} magnitude (dB) for the frequency range 1-10 GHz when the transmitting and the receiving antennas are at their farthest position.

$(\mathrm{avg}_M\{E^{\mathrm{known}}_{np,\mathrm{tx}_m}\})$ is calculated and the HP is applied to the difference between the measured field and the average field as stated in eq. (4.6). However, when applying the Green's function in the reconstruction process, k_0 is now used. This is done due to the fact that unlike previous measurements, here the receiving antenna was not touching the external layer of the medium containing the target, and therefore the layer of air (free space) between the antenna and the medium could not be ignored; hence the initial use of k_1 resulted in some distortion. It was then observed that the use of k_0 (which corresponds to air) not only resulted in detection of the target, but also excellent positioning. Furthermore, the use of k_0 removes the need of having any knowledge about the dielectric properties of the target volume. Figure 5.5(b) shows the linear normalised intensity obtained through eq. (4.4) and using an appropriate image adjusting. A peak can be clearly detected in the region of the inclusion; thus, both detection and localisation are achieved for this multilayered problem.

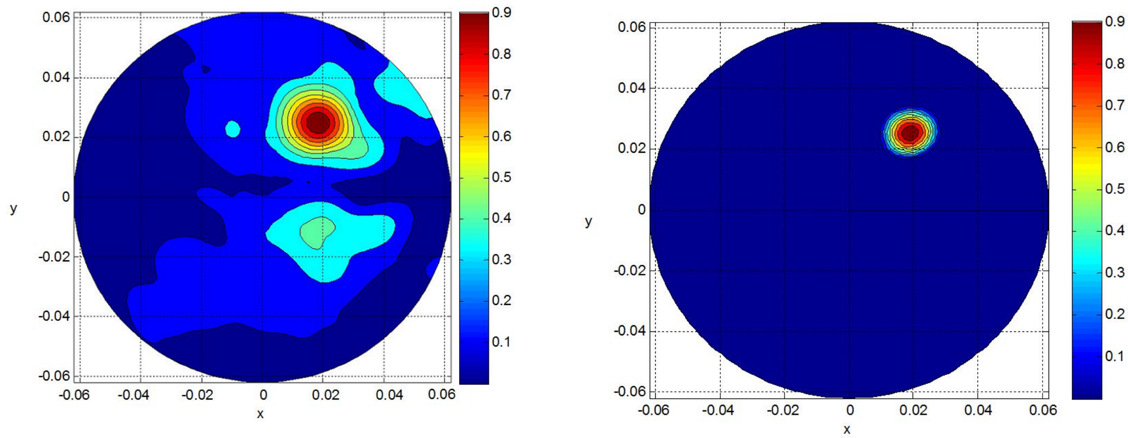

(a) (b)

Figure 5.5: Normalised intensity (linear), (a) before image adjusting, (b) after image adjusting. x and y axes are in metres.

5.2 Summary

In this chapter, the analysis of a novel microwave imaging procedure based on the Huygens principle has been extended to multilayered mediums, by making use of an analytical formulation based on the exact Maxwell solution for a multilayered eccentric cylinder. The model assumes that the body can be approximated as a stratified multilayered cylinder with an eccentric inclusion representing a tumour. The analytical model has been used for verifying HP procedure through simulations. Analysing the S/C and the resolution of the simulated model shows that HP method provides better performance when compared to some of the conventional time-domain approaches. Additionally, the HP has been tested through measurements using a multilayered phantom constituting of human-like tissues containing an inclusion. It has been shown that the HP can detect and locate an inclusion in multilayered cylindrical mediums. In the next chapter, we will see the extension of the HP through TLM simulations and measurements on inhomogeneous breast phantoms with inclusions.

6

Investigation of Huygens Principle Method on an Inhomogeneous Breast Phantom

6.1 Introduction

In previous chapters, the applicability of the HP method was tested on a range of moderately complex phantoms involving different numbers of layers and inclusions. All presented simulation and measurement results verified the capability of the method in detecting and locating one or more inclusions in a homogenous medium. In this chapter, both simulations and measurements are extended to image inhomogeneous hemispherical phantoms with inclusions.

The data obtained from the Microstripes analysis package is used in the reconstruction process for the case of a hemispherical breast model. Additionally, a commercially supplied breast phantom with multiple hidden inclusions has been used for measurements. As no information was provided by the manufacturer regarding the electromagnetic properties of the phantom, or the location of its inclusions, careful Elastography scanning [81, 82] was required to acquire an exact idea about the location and the size of the inclusions. Elastography is a non-invasive method in which stiffness or strain images of soft tissues are used to detect or classify tumours [83]. A tumour is normally between 5 and 28 times stiffer than the background of normal soft tissue [84]. Hence, when applying a form of mechanical compression or vibration, the tumour deforms less than the surrounding tissue, i.e. the strain in the tumour is less than that of its surrounding tissue [85]. The resulting tissue strain image is then shown on an Elastogram.

The rest of this chapter will then focus on imaging the breast phantom by employing HP, using vertically polarised antennas inside an anechoic chamber, and comparing it with the results achieved using the Elastography scanning machine. At the end of the chapter, the measurement is repeated with cross-polar and horizontal polarisation configurations, and the polarisation issues of electromagnetic imaging are also briefly investigated.

6.2 Numerical CST Microstripes Simulation using Transmission Line Matrix Method

Computer simulation technology (CST) Microstripes package is a solver of 3D electromagnetic problems, which employs the transmission line matrix (TLM) method to solve Maxwell's equations in time domain. The idea behind the TLM method is to discretise and approximate the space for computation of electromagnetic fields, based on the analogy between field propagation and a mesh of transmission lines [86]. Electromagnetic fields are then solved numerically in time domain with simpler and less computationally intensive equations.

6.2.1 Model 1: Cylinder

Before moving on to perform the simulation on a more complicated hemispherical model, the cylindrical model with an inclusion, which was successfully simulated analytically on MATLAB in section 4.3.3, is now numerically simulated to test the effectiveness of the TLM procedure for our purpose [87]. In this context, the dimensions of the base circle of the cylinder were kept the same as in the analytical model. This was also the case for the electrical properties of the materials and the position of the excitations (wire antennas). For each frequency, the output of the simulation was defined by a region encapsulating one layer of the cells in the cylinder, indicated by the yellow cuboid in fig. 6.1. The layer consisted of 10000 cells creating a cuboid of $100\times100\times1$ cells. There were attempts to further increase the number of cells for a better resolution, however this did not result in any improvements at the reconstruction stage.

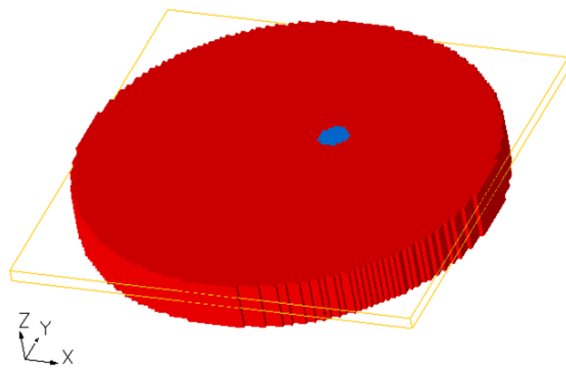

Figure 6.1: Discretised cylinder with frequency output region.

A frequency range of 1-1.2 GHz with 50 MHz sampling rate, creating 41 outputs was used in the simulation. The output table, which was then imported to MATLAB as a matrix, had 10000 rows representing each cell in the output region. The field reconstruction was done based on the field data on the surface of the cylinder. A vector of values were created to represent consecutive points on the cylinder surface. The matrix was then stripped off unnecessary rows and columns leaving only real and imaginary field components in the z-direction.

Having gathered the surface field data from both analytical and numerical solutions in MATLAB and Microstripes, respectively, it was possible to compare their outputs for one simulation. To do so, the magnitudes and phase plots of both solutions at 2 different frequencies have been plotted in fig. 6.2. The figures show similar patterns for both sets of solutions. In the left part of fig. 6.2(a), a difference in amplitude between the numerical and analytical solution can be seen. This is due to the lack of data point in the numerical solution for that particular frequency, which prevents the phase from reaching the desired maximum; this issue can be solved by changing the step size to achieve a better resolution.

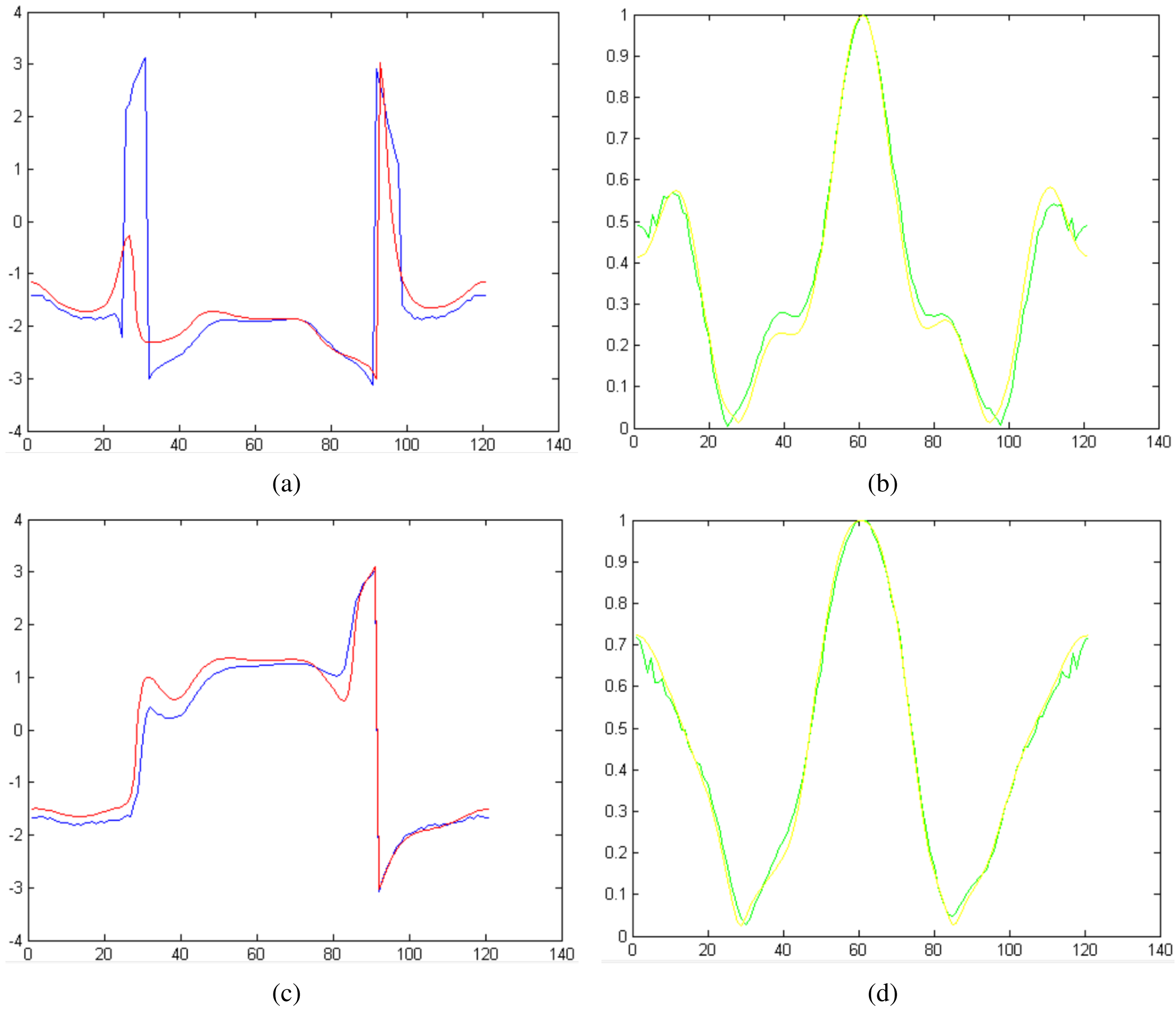

Figure 6.2: Comparison of analytical and numerical solutions. Graphs show normalised field of the 120 points on the surface of cylinder (Blue/Red - phase of analytical/numerical solution, Yellow/Green - magnitude of analytical/numerical solution) for (a),(b) 1 GHz and (c),(d) 1.1 GHz.

At this point, all analytical and numerical output solutions consisted of 120 data points on the surface of the cylinder. This is not very realistic, as in reality, it would be very time consuming to take such large number of measurements; rather, the most convenient way would be to use an array of antennas to perform more measurements at once. In such case, the number of received data points would be limited depending on the size of the single array. Assuming an array cell size of 2 cm, there could be around 18 data points on the cylinder surface. Moreover, in real life, the antenna array around the breast could scatter the incoming waves from the transmitting antenna.

The proposed solution was to use cells from the antenna array as transmitters in the following Microstripes simulations. The cylindrical model was modified such that the sources were on the cylinder. In addition, many adipose inclusions, with dielectric constant and conductivity values of 10 and 0.02 S/m, respectively, were placed randomly inside the cylinder in this model to evaluate the performance of the reconstruction algorithms in dealing with an inhomogeneous medium. Next, the algorithms were modified to include only 18 data points from the surface of the cylinder. The new solution was tested and the resulting reconstruction image was compared with the previous one, which employed 120 receiving points. Figure 6.3 shows the difference between normalised intensity images. It can be seen that there is only a minor difference between the original model and the more realistic one.

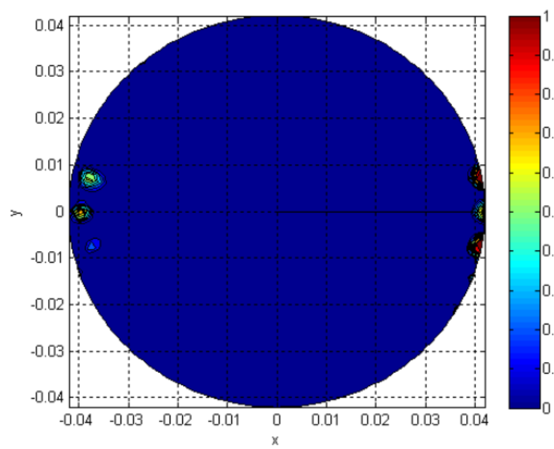

Figure 6.3: Difference between normalised intensities of the two antenna configurations (original model with 120 receiving data points and the more realistic one with 18 receiving data points), showing that there is not much difference between the two models.

Having tested the effectiveness of the method on a cylindrical geometry, it was then possible to move on to more complex simulations on a hemispherical model.

6.2.2 Model 2: Hemisphere

A hemisphere is the simplest geometrical 3D approximation to a female breast and a reasonably good one too. Unlike the cylindrical model, it presents the problem in the method of data gathering. In previous analysis it was assumed that it is possible to collect data from the whole surface of cylinder. In the case of a hemisphere it is possible to collect data only from the spherical surface as in real life the flat surface is joined to the rest of the body. According to HP there is a need of knowledge of all field points on the wavefront to reconstruct the wave. In a hemisphere this could limit reconstruction in z-direction. To test how the reconstruction algorithms would deal with a hemisphere a model (shown in fig. 6.4) was created (Chmielewski [87]). The hemisphere has a radius of 5 cm and electrical properties of $\varepsilon_1 = 40$ and $\sigma_1 = 0.2$ S/m. In addition, a small spherical inclusion having a radius of 3 mm, with $\varepsilon_1 = 60$ and $\sigma_1 = 2$ S/m was placed at a radial position of 2.6 cm from the axis of the sphere, at an azimuth and inclination position of 45° with respect to the axis.

It should be pointed out that the model considered here is a basic one, and hence does not consider some of the important challenges in real breast imaging scenarios such as skin reflection, spine effects and the presence of dense tissues.

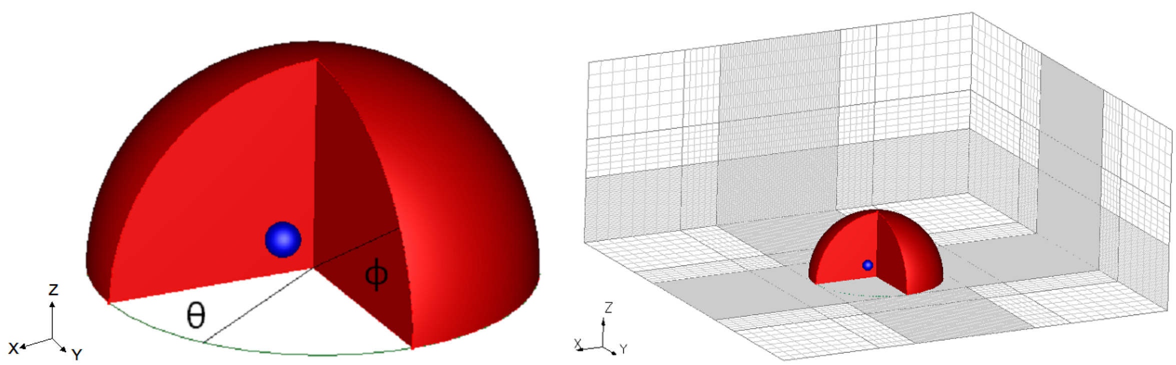

(a) (b)

Figure 6.4: (a) Hemisphere model of a human breast and (b) mesh around it [79].

Meshing for the hemisphere is much larger as it is extended by 50% of a wavelength in 5 directions. The computation takes approximately 6 times longer than that of the cylindrical model. All boundaries, including the bottom, were absorbing. In real life, there would be some scattering from the rest of the body but here it was assumed that such scattering is negligible in comparison with other unwanted effects described later.

The antenna sources had also to be reconsidered for the hemispherical model. In the 2D analysis of the cylinders, the wire antennas were represented as point sources and only z-polarisation of the field was analysed. Other types of antenna could have been used but the wire was consistent with the analytical solution and allowed for some verification. In the case of the 3D analysis of the hemisphere, 3 directions needed to be considered and it was uncertain where and how antennas should be placed to provide the best reconstruction. The most widely used excitation, with the least degrees of freedom, is a plane wave and it offers more clarity in 3D analysis. It is less realistic in the context of medical scanning but the plane wave excitation could provide a good initial step to 3D modelling.

However, there is a phase change when using the plane wave instead of a wire. Figure 6.5 shows two wavefronts of a plane wave indicated by green colour, and a wavefront from a wire antenna shown in blue. For these two different waves the fields on the surface of the hemisphere have a relative phase difference. This effect is magnified because of the curvature of the hemisphere and would also occur for other polarisations (i.e. when the blue wavefront was generated by a horizontal wire).

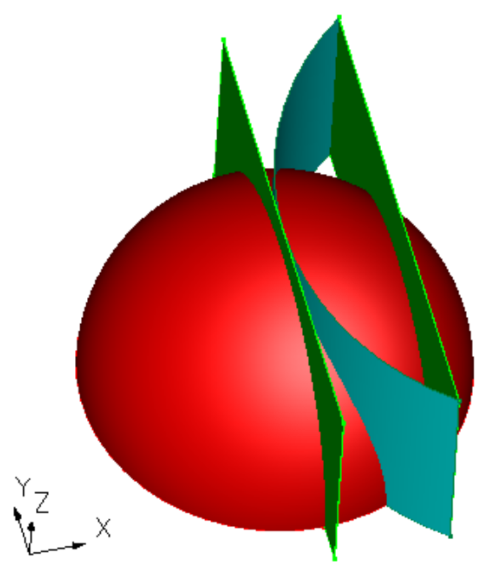

Figure 6.5: Wavefronts from plane wave and wire antenna, shown in green and blue colour, respectively.

In order to check whether the reconstruction algorithms can deal with the phase difference a quick test was performed. As such, the 2D homogeneous cylinder model was re-simulated with plane wave sources instead of line sources propagating at 0°, 120° and 240° to the xz-plane (similar to fig. 6.5 but in 2D). The localisation is good but a mirror effect is present (fig.

6.6). This mirror effect can be explained due to the small number of observation points in the Microstripes simulation, resulting in the generated field to be less accurate than the analytical simulations performed in the previous chapters.

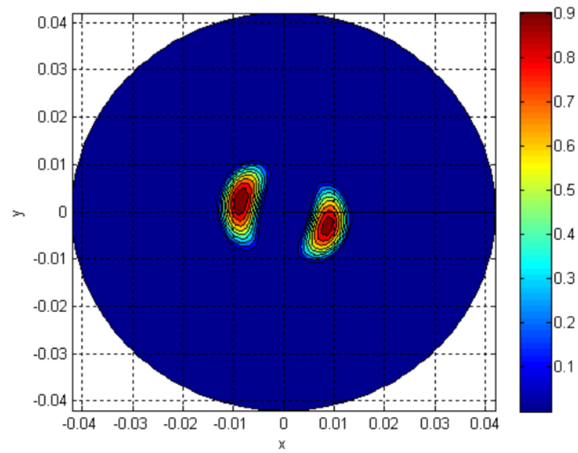

Figure 6.6: Reconstructed field for planar wave excitation. x and y axes are in metres.

Having confirmed that the reconstruction algorithms were compatible with a planar waveform in 2D, it was possible to continue with the hemispherical model. There were 4 planar excitations directed at 0°, 90°, 180° and 270°, each with two polarisations orthogonal to propagation direction. Hence, all 3 components were present in the analysis which could provide extra information.

The reconstruction algorithms had to be modified to accommodate 3D analysis with 3 polarisations. There were two ideas of approaching the problem [87]. In the first one, the hemisphere was cross sectioned into 2D slices and analysed as cylinders [fig. 6.7(b)]. The biggest advantage of this method is that reconstruction algorithms have been already proved to work in the cylindrical models. However, changing the 3D analysis into a sequence of 2D analyses allows for only one polarisation, so information from the remaining two is lost. Moreover the scattering from neighbouring layers could influence the result for a particular layer and worsen the localisation. Thus this approach was not researched further. The more sophisticated way of modifying the reconstruction algorithms was to implement vector analysis. Numerical solutions provide information about all three polarisations and hence the output electric field is a vector field. The reconstruction algorithms had to propagate all three polarisations from each surface point taking into consideration the direction of propagation [fig. 6.7(a)]. The field magnitudes were then summed for all frequencies and antenna positions to create the final reconstructed field. Hence, no information was lost and inclusions' shapes that would be difficult to detect in only z polarisation could be clearly visible. Therefore, this method was chosen to modify the algorithms.

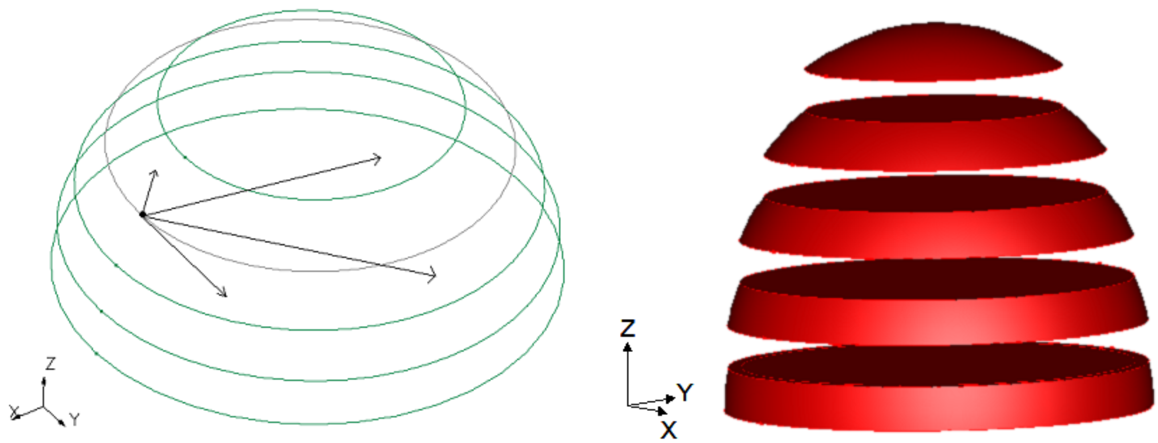

(a) (b)

Figure 6.7: Principle of: (a) full 3D reconstruction and (b) 2D cross-sections [79].

The first step in the new reconstruction algorithm was to import data. As mentioned above the output included extra dimension because of all 3 polarisations being analysed. The surface data points were defined on the edges of cross sections in z direction [green rings in fig. 6.7(a)]. They were equally spaced with their number proportional to the ring radius. Each point was defined by a position vector and a field vector. For each of these sources and each point inside the hemisphere, a propagation vector was defined, which simply linked these two points. This vector was then used to define a new coordinate system with the x$'$-axis along the vector. A transformation matrix linking these two systems had to be derived.

Lets assume a vector **p** to be an example of a propagation vector with spherical coordinates $\theta = \beta$, $\phi = \alpha$ and $\rho = r$, as shown in fig. 6.8. To create the new coordinate system X$'$Y$'$Z$'$, the existing coordinate system should be rotated first by β in xy-plane and then by α in z direction. Similarly, if there is a field defined in XYZ coordinates by polarisations E_x, E_y and E_z it also

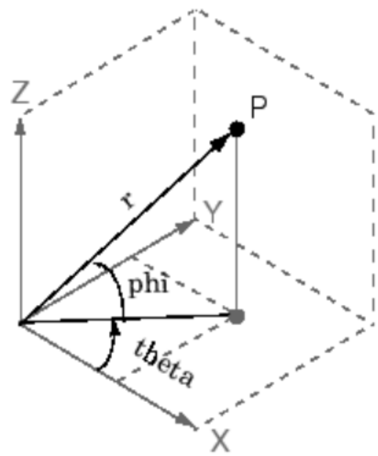

Figure 6.8: Propagation vector **p** defined by point P in XYZ coordinate system.

should undergo a similar transformation to be expressed in X′Y′Z′ coordinates by polarisations E'_x, E'_y and E'_z. Hence it is necessary to build the following transformation matrix.

$$\begin{bmatrix} E''_x \\ E''_y \\ E''_z \end{bmatrix} = \begin{bmatrix} \cos(\beta) & -\sin(\beta) & 0 \\ \sin(\beta) & \cos(\beta) & 0 \\ 0 & 0 & 1 \end{bmatrix} \begin{bmatrix} E_x \\ E_y \\ E_z \end{bmatrix} \quad \text{or} \quad \mathbf{E''} = \mathbf{BE} \tag{6.1a}$$

$$\begin{bmatrix} E'_x \\ E'_y \\ E'_z \end{bmatrix} = \begin{bmatrix} \cos(\alpha) & 0 & -\sin(\alpha) \\ 0 & 1 & 0 \\ \sin(\alpha) & 0 & \cos(\alpha) \end{bmatrix} \begin{bmatrix} E''_x \\ E''_y \\ E''_z \end{bmatrix} \quad \text{or} \quad \mathbf{E'} = \mathbf{AE''} \tag{6.1b}$$

$$\mathbf{M} = \mathbf{AB} \quad \text{and} \quad \mathbf{E'} = \mathbf{ME} \tag{6.1c}$$

Note that in eq. (6.1), E''_x, E''_y and E''_z represent the coordinates after xy-transformation. After obtaining the transformation matrix for the propagation vector, the surface point source field $\mathbf{E_{ps}}$ was transformed to the propagation coordinates. Naturally, only components perpendicular to the propagation direction matter and in the new coordinate system these were simply E'_y and

E'_z polarisations. The field was then propagated using an exponential function with appropriate impedance and propagation constant. Finally it was transformed back to original coordinates.

$$E(x,y,z) = \mathbf{M}^{-1} Z e^{-k_1|r|} \mathbf{E_{prop}} \tag{6.2}$$

where, $E(x,y,z)$ represents the field at a point (x,y,z) and $\mathbf{E_{prop}}$ is equal to $\mathbf{M}.\mathbf{E_{ps}}$ (point source field transformed into propagation coordinates) but with the first coordinate equal to 0.

Next, the 3 polarisations for all frequencies, source points and antenna positions were summed to give a 3D vector field. The resolution of the reconstructed field was set to be 30 by 30 by 8 cells using 512 point sources on the surface. Previous results from 2D analysis showed that it is adequate to use less point sources and therefore, their number was decreased to 128. The normalised intensity of the reconstructed field is shown in fig. 6.9.

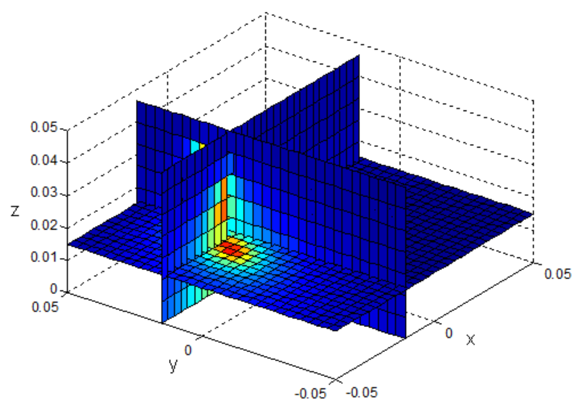

Figure 6.9: Reconstructed field of a homogeneous hemispherical model. x, y and z axes are in metres.

The inclusion can be clearly detected at its correct position in the reconstructed field without any mirror or shift effects present. The results prove that extra information from additional polarisation would improve the localisation of the inclusion. Having successfully tested the application of 3D reconstruction algorithms on a homogeneous breast model, it was then necessary to test them with an inhomogeneous hemisphere. For this purpose, some adipose inclusions with electrical properties $\sigma = 0.02$ S/m and $\varepsilon = 10$ were added to the existing model (fig. 6.10).

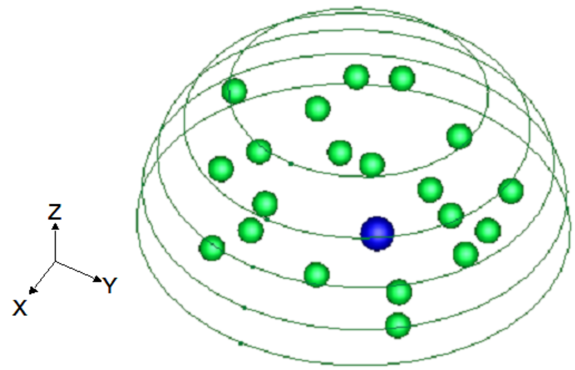

Figure 6.10: Inhomogeneous hemisphere model with hidden normal tissue spots.

Figure 6.11 shows the linear normalised intensity obtained through HP. Again, the reconstruction successfully detects the inclusion spot. However, another large residual spot is also present, most probably, due to the decrease in resolution caused by the reduced number of receiving points, and could be removed by increasing the input data which enhances the resolution. Before further modelling, it was important to validate the capability of the HP method on measurements involving inhomogeneous phantoms, as we will see in the next section.

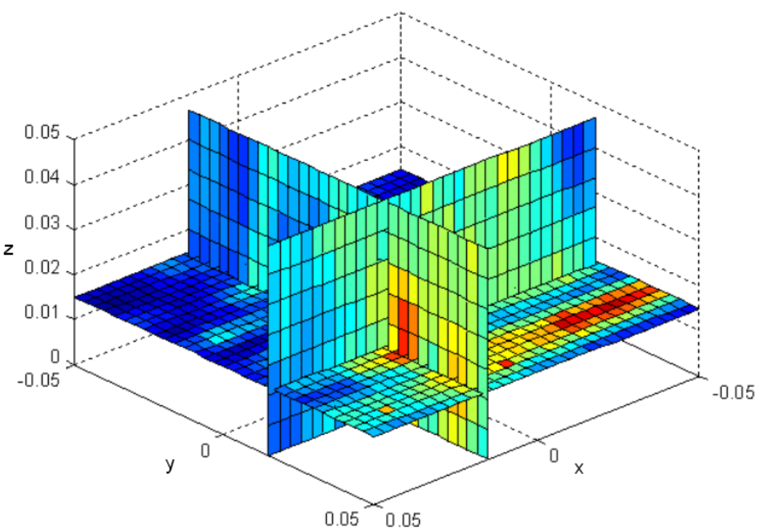

Figure 6.11: Reconstructed field of an inhomogeneous hemispherical model. x, y and z axes are in metres.

6.3 Breast Phantom Imaging: Measurement Results

6.3.1 Elastography Imaging Results

A model-059 [88] breast phantom, 15 cm in length, 12 cm in width and 7 cm in height, was chosen for the purpose of measurements. The phantom is made of a solid elastic water based polymer, known as Zerdine [89], and has a volume of 600 cc (see fig. 6.12). The size and shape of the phantom simulates that of an average patient in the supine position. The properties of the model allow it to accurately mimic the ultrasonic characteristics of tissues found in an average human breast [90].

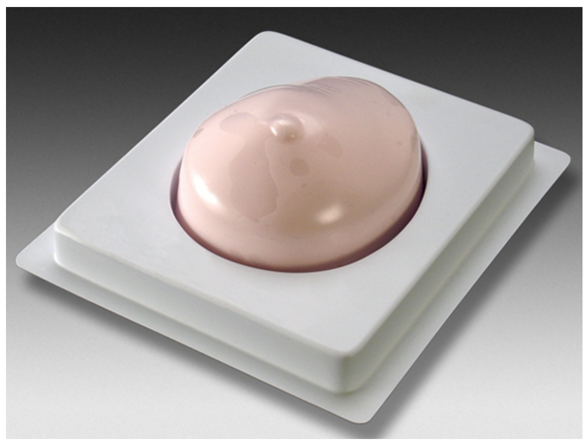

Figure 6.12: Breast phantom model 059.

According to the company, the phantom contains 12 randomly positioned solid masses (inclusions), 3-12 mm in diameter, that appear isoechoic to the simulated breast tissue under normal ultrasound, however, the lesions are 3 times stiffer than the background enabling them to be detected on Elastograms [88]. As the Elastograms are accurate, and an exact information on the size and position of each inclusion was needed, it was necessary to image the phantom using the ultrasound based Elastography machine first before proceeding to perform HP based measurements. The Elastography imaging is performed by attaching the Elastography transducer to the phantom (fig. 6.13), slightly pressuring it inwards and outwards whilst slowly moving the transducer around until an inclusion appears on the Elastogram image (fig. 6.14). This procedure is repeated in all directions until the whole phantom surface is covered. The

Elastogram image provides the necessary information about the dimensions of the inclusion and its depth from the surface of the phantom. In order to increase the matching between the transducer and the phantom, a thin layer of gel needs to be placed between them.

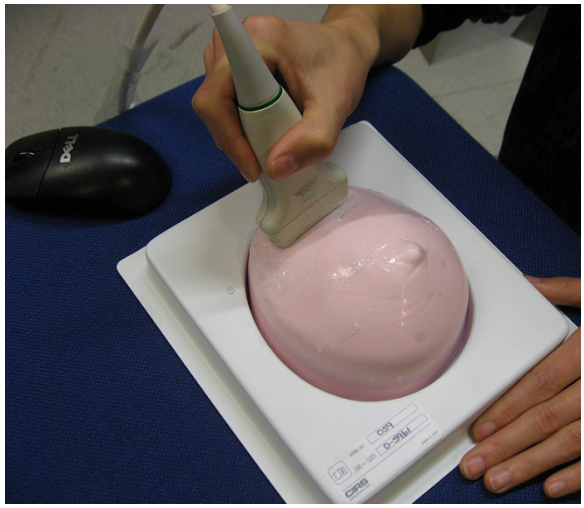

Figure 6.13: Elastography scanning of the phantom via the transducer.

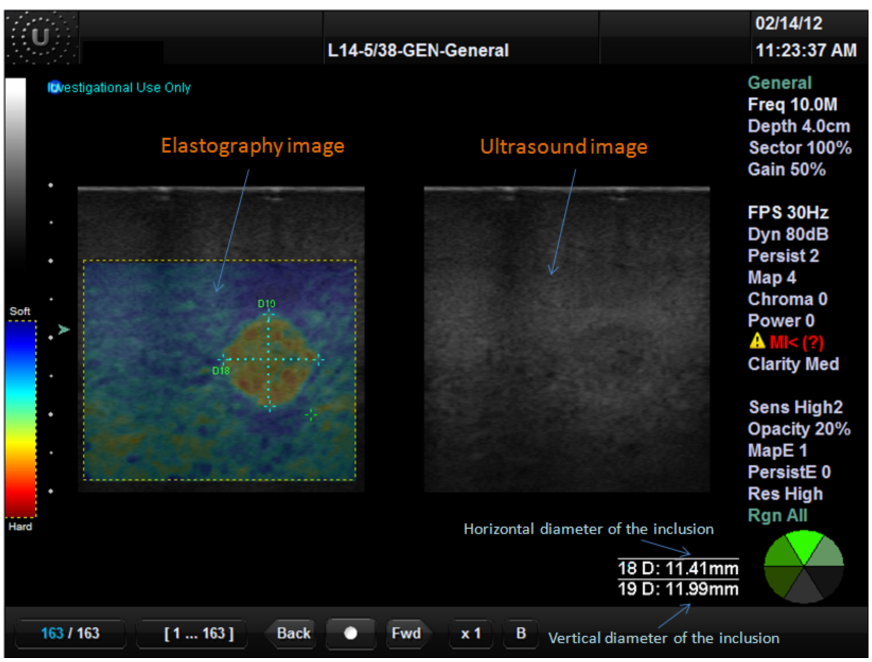

Figure 6.14: Elastogram screen, an inclusion is detected by Elastography while it remains hidden in the ultrasound image.

After a careful scan, 8 masses, varying in diameter between 8 and 12 mm were detected around the phantom (table 6.1). The information from the Elastogram image was then used to locate the position of the masses on a 3D hemispherical design. The resulting diagrams, from three different views are shown in fig. 6.15. The blue '+' mark indicates where the centre of each mass is located.

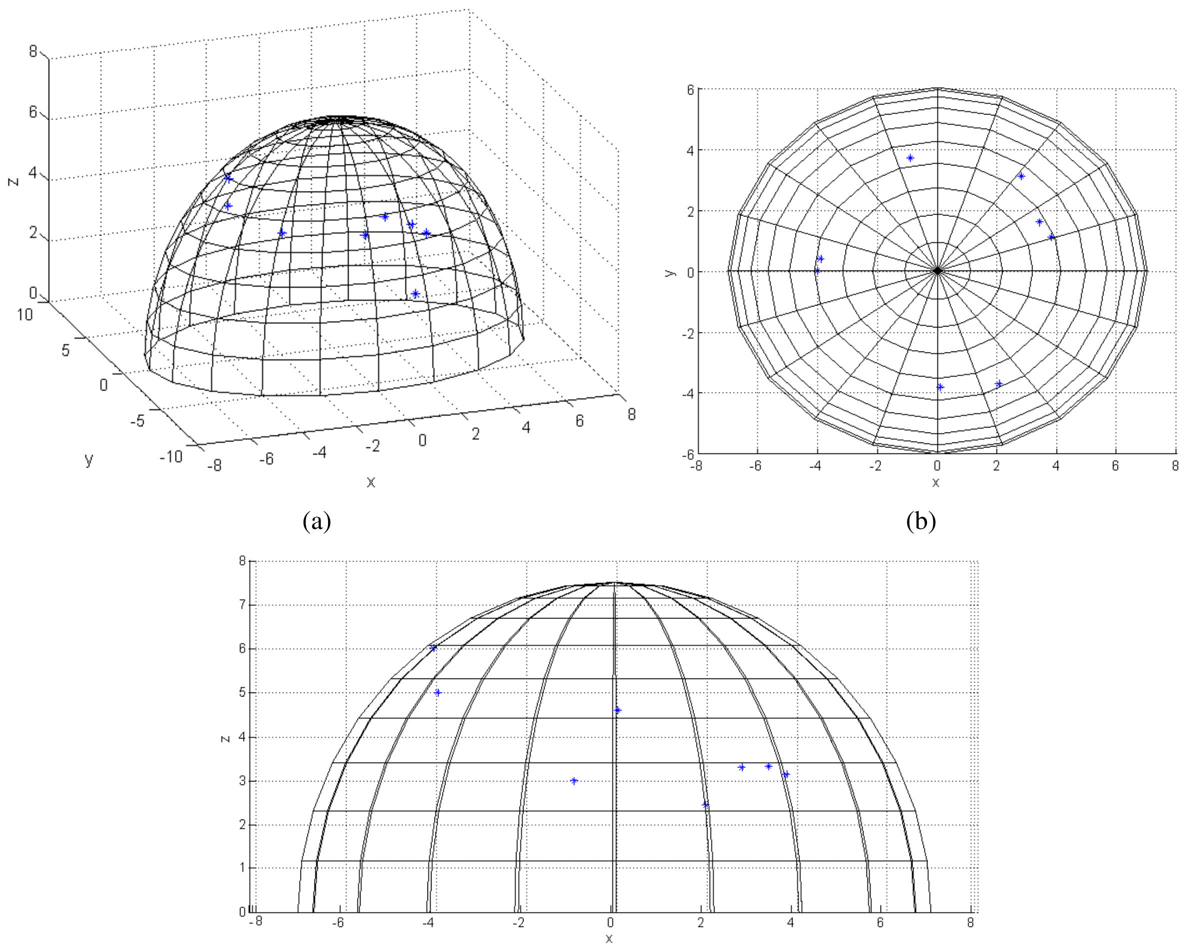

(a) (b) (c)

Figure 6.15: 3D mapping of the location of the inclusions from different views: (a) general 3D view, (b) view from above (planar) showing x and y axes, (c) view from the side showing x and z axes. All axes are in centimetres.

6.3.2 Microwave Imaging Results

The results from the previous section indicate that the solid masses are spread in different depths and heights inside the breast phantom. Elastography imaging results show that all of the inclusions are situated between 2 and 6 cm above the flat surface of the phantom [fig. 6.15(c)].

Table 6.1: Coordinate location and diameter size of the detected inclusions from Elastography scanning.

Inclusion	x-coordinate	y-coordinate	z-coordinate	diameter (mm)
1	-0.91	3.7	3	8.5
2	2.8	3.1	3.3	8
3	-4	0	6	11.9
4	3.8	1.1	3.14	12
5	-3.9	0.4	5	12
6	3.4	1.6	3.33	9.3
7	2.05	-3.7	2.45	9
8	0.1	-3.8	4.6	10

Hence, to cover this height of interest, it was decided to perform 4 planar measurements at 1 cm intervals using the discone antenna. For this purpose, four pairs of cylindrical stands (fig. 6.16), with heights 5, 6, 7 and 8 cm were constructed and used such that the centres of the antennas were placed at 2.5, 3.5, 4.5 and 5.5 cm above the surface of the phantom, respectively. Both transmitting and receiving discone antennas used were 1.5 cm long, enabling each measured cut to be fully covered by their signals.

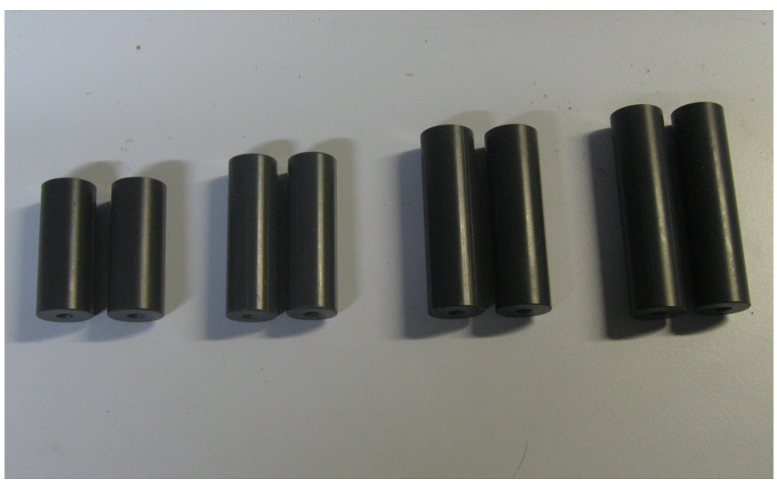

Figure 6.16: 4 pair of cylindrical stands with heights 5, 6, 7 and 8 cm used for measuring different breast phantom cuts.

Frequency-domain UWB measurements were performed in an anechoic chamber, using a VNA arrangement to obtain the transfer function. Discone antennas, vertically polarised and omni-directional in the azimuth plane, were used after calibration. The measurements were recorded using a large frequency range of 1-10 GHz and a frequency sampling of 5.6 MHz. For each set of measurements, the location of the transmitting antenna was fixed at approximately 25 cm away from the centre of the breast phantom, while the receiver antenna was positioned roughly 1 cm away from the major axis surface of the phantom and mounted on a computer-controlled rotating stage with 3° of angular resolution (fig. 6.17).

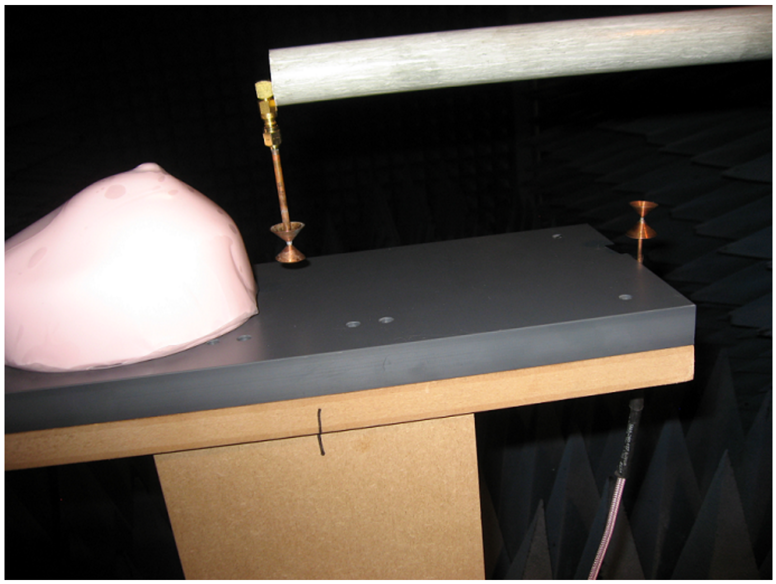

Figure 6.17: Antenna arrangement corresponding to the bottom cut measurement (2.5 cm above surface).

After observing the S_{21} magnitude, frequency range of 2-3 GHz was chosen for the purpose of reconstruction. Next, the field at $N_{\mathrm{PT}} = 120$ equally phi-spaced points lying on the external surface was measured; the employed number of points leads to a spatial sampling of approximately $0.1\lambda_{1,f_{\max}}$. For each height, 8 sets of data were recorded, changing the position of the transmitting antenna along phi with a step of 45°. Next, the average of the 8 data sets was calculated and the HP was applied to the difference between the measured field and the average field as stated in eq. (4.6). The same procedure was repeated for the other 3 planar measurements. Figures 6.18(a), (b), (c) and (d) show the linear normalised intensity obtained through eq. (4.4), corresponding to heights 2.5, 3.5, 4.5 and 5.5 cm of the phantom above the flat surface, respectively.

In total, 10 peaks of varying intensities can be clearly detected in the figures, 6 of which have been detected at approximately the same positions using the Elastography machine. The

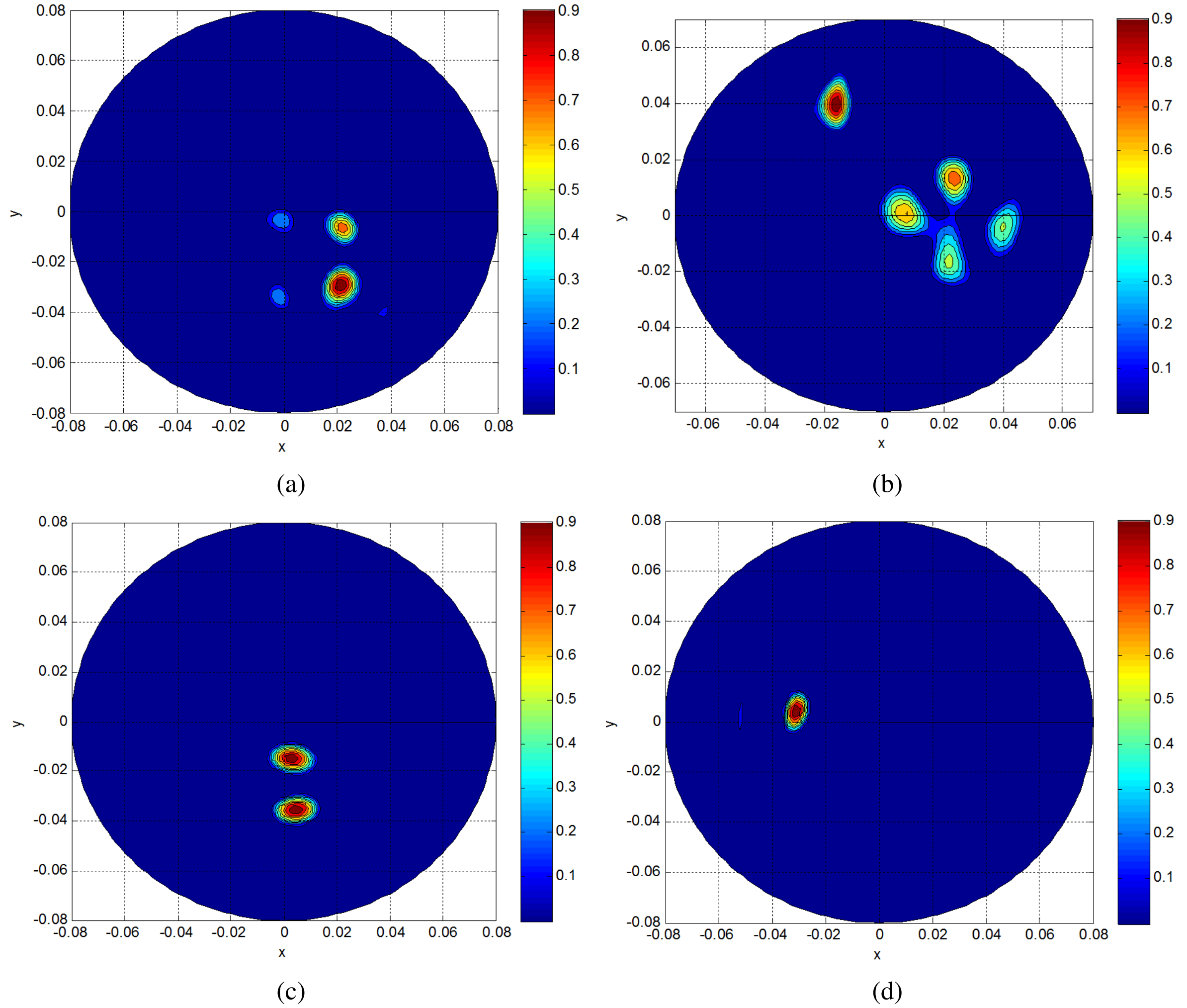

Figure 6.18: Linear normalised intensity, corresponding to heights (a) 2.5, (b) 3.5, (c) 4.5 and (d) 5.5 cm of the phantom above the flat surface, respectively.

others, could have either been detected as mirror image [see figs. 6.18(a) and 6.18(b)], or might represent an inclusion undetected by the Elastogram possibly due to its deep position inside the phantom (inner inclusion in fig. 6.18(c)). Therefore, it has been shown that our technique is capable of detecting and locating inclusions even in an inhomogeneous medium.

It is important to point out that for this measurement, the quantity k_1 was used instead of k_0 (which was used in multilayered measurement of section 5.3.2) in the Green's function for the reconstruction process. It is speculated that, this is because of less contrast in the relative permittivity between air ($\varepsilon_r = 1$) and breast phantom (speculated to have $\varepsilon_r \simeq 10$), than there is between air and Agar-Agar ($\varepsilon_r \simeq 70$). This means that, comparing to the previous measurement the contrast between the two mediums is reduced by a factor of 7 and hence there is less mismatch. Therefore, the algorithm considers the breast phantom (and not the air) as the first medium for this configuration. Another important point to note is that due to the hemispherical shape of the phantom and circular rotation of the receiving antenna, the distance of the receiving antenna from the surface of the phantom varies during the 360° scan of the object which could have had minor affect on the exact positioning of the inclusions during the reconstruction process. This problem could be solved by employing a mechanical scanning system which has the receiving antenna always placed at a touching distance from the external surface.

6.3.3 Changing the Antenna Polarisation

So far all the measurements performed had seen both transmitting and receiving antennas vertically polarised with respect to the medium being imaged. In this section, to observe the effect of changing the polarisation on the quality of the detected image, two other polarisation setups were investigated. Specifically, the breast phantom imaging measurement for the cut containing the most number of inclusion, i.e. height of 3.5 cm above level, was repeated twice considering cross-polar and horizontal polarisation arrangements of discone antennas, respectively.

6.3.3.1 Cross-polarisation Measurement

The measurement performed in section 6.3.2 was repeated for the cut containing the most inclusions (3.5 cm cut), by rotating the transmitting antenna by 90° with respect to the phantom, thus placing the discone antennas in a cross-polar formation. Again, a frequency range of 1-10 GHz with 5.6 MHz sampling rate was used. Figure 6.19 shows the logarithmic S_{21} magnitude in the 1-10 GHz range for the farthest antenna position ($\sim$33 cm). It can be observed that for most part there is poor signal that falls below the -70 dB noise level, which is the expected behaviour for this kind of polarisation.

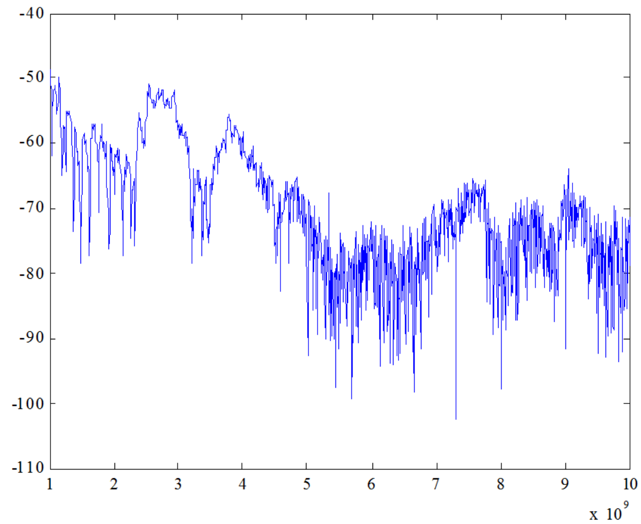

Figure 6.19: S21 magnitude (dB) corresponding to the frequency range 1-10 GHz when transmitting and receiving antennas are at their farthest position ($\sim$ 33 cm) in a cross-polarisation setup.

The frequency range with the best power level, i.e. 2.5-3 GHz was chosen for the purpose of reconstruction. Next, the average of the 8 data sets was calculated and the HP was applied to the difference between the measured field and the average field as stated in eq. (4.6). Figure 6.20 shows the linear normalised intensity obtained through eq. (4.4), and after image adjusting.

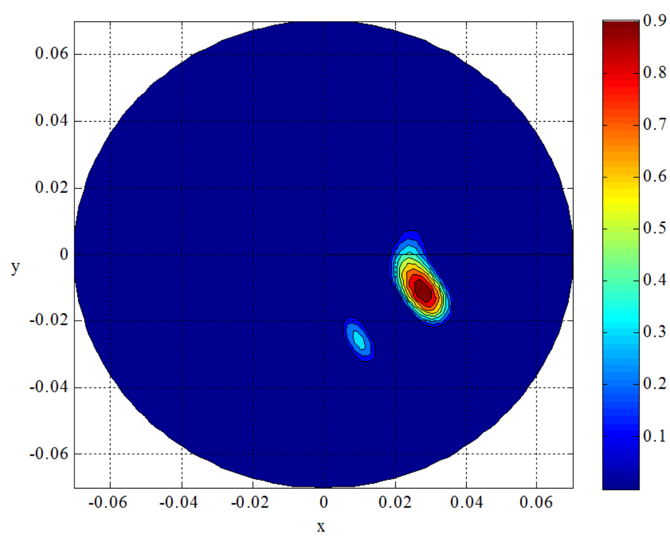

Figure 6.20: Linear normalised intensity when imaging the breast phantom using cross-polarised antennas.

A peak can be seen on the x-axis; the peak does not move as the position of the transmitter is varied; therefore it is assumed to be an image of the transmitter.

6.3.3.2 Horizontal Polarisation Measurement

Previously, we observed that our proposed imaging technique is capable of locating the inclusions using vertically polarised antennas. An investigation was needed to check whether similar detection can be achieved using horizontally polarised antenna setup. To repeat the breast phantom measurement of section 6.3.2 using a horizontal polarisation, both transmitting and receiving discone antennas were rotated by 90° with respect to the position of the phantom (fig. 6.21); meanwhile the frequency range, sampling, number of measurements and the distance of the antenna from the object remained the same as before. Figure 6.22 shows the

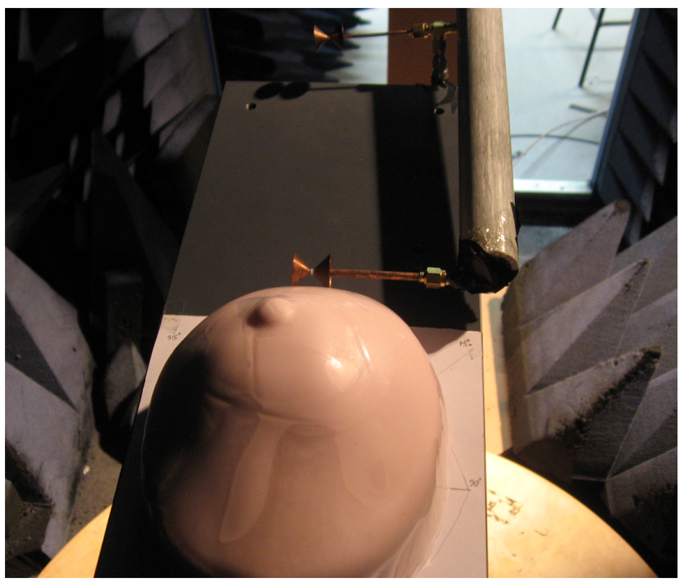

Figure 6.21: Experimental setup for imaging the breast phantom with horizontally polarised discone antennas.

S_{21} logarithmic magnitude corresponding to the recorded frequency range. We can see a much better power level compared to the cross-polar case and the magnitude only falls below the noise level after 5 GHz. Once more, frequency range of 2.5-3 GHz was chosen for the purpose of reconstruction. The average of the 8 data sets was calculated and the HP was applied to the difference between the measured field and the average field as stated in. Figure 6.23 shows the linear normalised intensity after image adjusting.

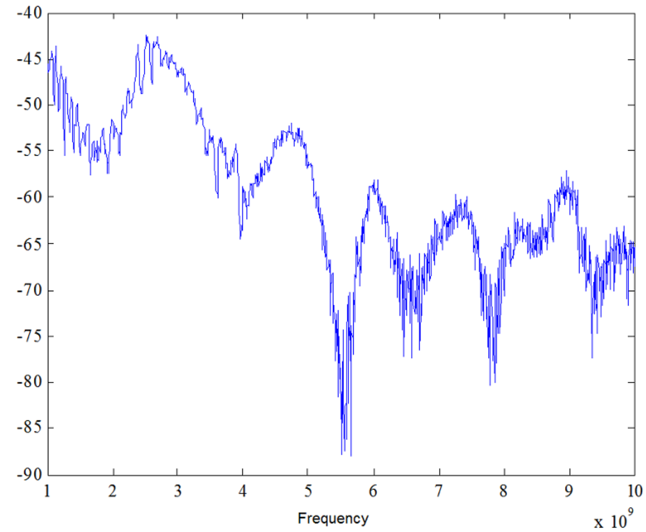

Figure 6.22: S21 magnitude (dB) corresponding to the frequency range 1-10 GHz when the transmitting and the receiving antennas are at their farthest position (∼33 cm) in a horizontal polarisation setup.

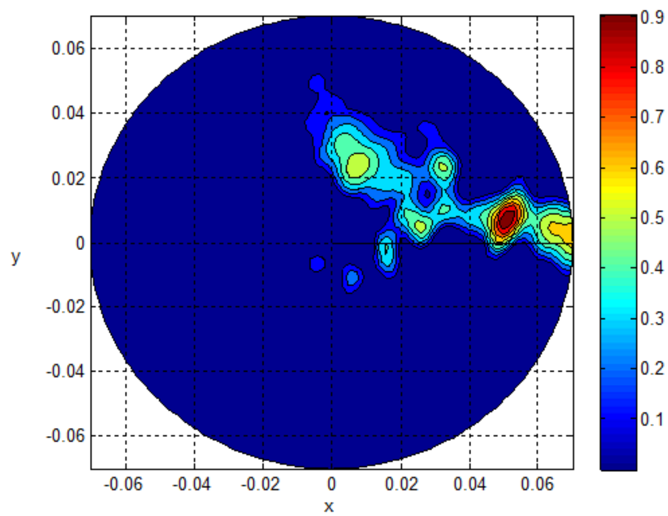

Figure 6.23: Linear normalised intensity when imaging the breast phantom using horizontally polarised antennas.

Some peaks with different intensities are seen, which do not represent any of the inclusions because their position does not vary with the movement of the transmitter. The darkest peak is presumed to be an image of the transmitter. Therefore, we can conclude that the phantom is not an electromagnetic type, but rather an "anisotropic" one. To validate this assumption, the P.M.M.A. with 2 inclusion measurement in section 4.4.3 was repeated using horizontal polarisation. Both inclusions were detected, although the measurement showed a decrease in signal level and the resolution due to less current being excited in the wires compared to the vertical polarisation case, as would be expected.

6.3.3.3 Polarisation comparison when no object is present

One final set of measurements was carried out to compare the performance of the discone antenna for different polarisations when no object is present. The distance between the antennas and all other measurement parameters remained unchanged. Figure 6.24 shows the linear magnitude for different polarisations with respect to the measured angular position for a single frequency, when the antennas are in their nearest position (∼15cm). A similar trend can be seen in all polarisation setups.

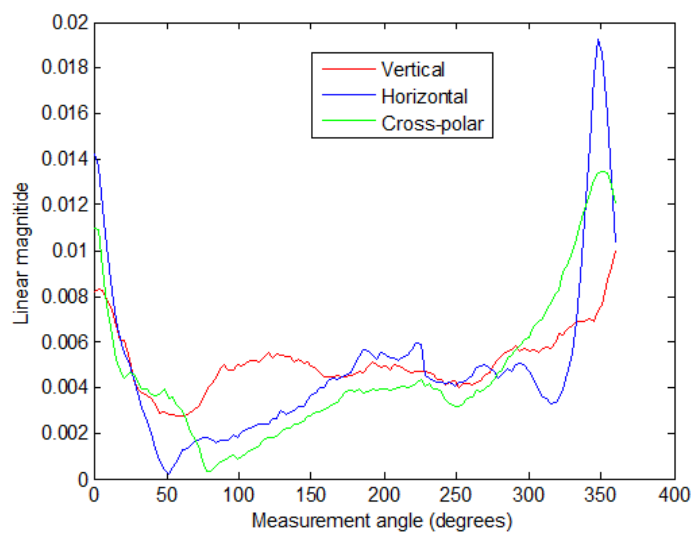

Figure 6.24: Comparison in linear magnitude between the 3 polarisations for a single frequency when no object is present.

Finally, the logarithmic magnitude with respect to the frequency range of 1-10 GHz for a single measurement in horizontal and cross-polar polarisations, when the antennas are in their nearest position (∼15cm) is plotted in fig. 6.25. It can be observed that the horizontal polarisation gives a good performance for very low (1-3 GHz) and very high (8-10 GHz) frequency ranges whilst in the cross-polar case we have a low power, noisy and alternating signal for most of the frequency band.

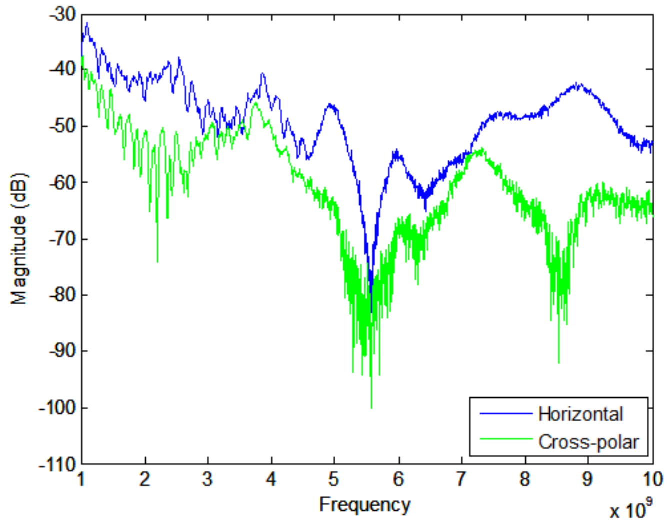

Figure 6.25: Comparison in logarithmic magnitude between horizontal and cross-polar measurements for a single measurement, when no object is present.

6.4 Summary

In this chapter, the application of the HP technique was extended to simulations and measurements involving inhomogeneous media. Numerical simulations on Microstripes showed promising results in detecting and locating an inclusion within both homogenous and inhomogeneous cylindrical and hemispherical models. Furthermore, comparing HP based measurement results (using a very simple setup with only 2 antennas) on an inhomogeneous hemispherical breast phantom with many inclusions, with that obtained from Elastography scanning further proved the capability of this novel method in good detection and localisation of multiple inclusions while satisfying the optical resolution limit.

In the microwave measurements performed in this research, the nominal output power of the VNA is 2 mW, out of which a much lower power of approximately 0.3μW reaches the object; this value is very low in comparison with existing imaging techniques. In terms of the specific absorption rate (SAR) [91], which indicates the rate of absorption of electromagnetic radiation by human body tissues, the measurements show a low value of 3.3 mW/kg. This is much less than the SAR limits set by the USA (1.6 W/kg in 1g of tissue) and Europe (2 W/kg in 10g of tissue) [91], and the average of SAR of mobile phones (0.7-1.3 W/kg) [92].

Hence, it can be seen that the transmitted power of the measurements can be further increased without causing any damage to the tissues. With more time and investment spent on improving this method, especially in terms of building an automatic scanning machine, the technique will have the potential to emerge as an alternative and efficient technique for clinical testing.

7

Conclusions and Proposed Future Work

7.1 Conclusions

This thesis's contribution to the UWB microwave imaging has been the development of two novel methods of image formation for the purpose of medical applications. Other than their simplicity, non-ionising and non-invasive features, another benefit of the two methodologies is their capability of capturing the contrast or dielectric variation. The methods, which are equivalent to a synthetic time-reversal algorithm, allow all the information in the frequency domain to be utilised by combining the information from the individual frequencies to construct a consistent image with a resolution of approximately one quarter of the shortest wavelength in the dielectric medium, without using contrast agents.

The first introduced method based on the mode-matching of Bessel Functions covered a smaller part of this thesis. Using the MM Bessel function procedure (which employs Born approximation) leads to the generation/inversion of a rather small matrix, whose dimensions are not related to the discretisation of the volume where the image is required. Validation of the technique through both simulations and measurements on cylindrical media with one or more inclusions has been presented, illustrating the effectiveness of the method. It follows that, if the properties of the external object are known, both detection and localisation are achieved using

MM. On the other hand, with regards to the MM method, the use of Bessel functions limits the applicability to cylindrically-shaped objects, and the extension of the method to realistic 3D geometries does not seem to be straightforward; moreover, MM requires matrix generation and inversion, and the knowledge of the field on the entire external surface. Hence, due to these difficulties, another approach was needed to be exploited.

The last three chapters of this thesis have focused on Huygens principle technique, a novel, fast and accurate microwave imaging method based on the principles of physical optics. Using HP to forward-propagate the waves removes the need to solve inverse problems and, consequently, no matrix generation/inversion is required. HP can be applied to more general geometries and its application is not limited to cylindrical or spherical media. It follows that the methodology can identify the presence and location of significant scatterers inside a volume, without the need for a'priori knowledge on the dielectric properties of the target object. Due to the above features, HP was the chosen method for the rest of the investigations. Going along the thesis, a step by step extension of the HP method to more and more complex geometries can be seen. The simulations and measurements began on simple media with an inclusion, and then followed to successfully image media with multiple inclusions, multilayered media and finally inhomogeneous realistic hemispherical phantoms, respectively.

All the measurements performed in this thesis have satisfied the UWB definition of having bandwidth of at least 20% of centre frequencies, while the power levels used and the specific absorption rates were well within the safety limits. Moreover, the measurement results indicate the robustness of the methods with respect to the usage of two different types of UWB designed antennas. In addition, quantitative analysis on signal to clutter ratio and resolution with respect to the band, optimum number of transmitting and receiving positions required, frequency sampling and performance with respect to uncertain knowledge of the dielectric properties of the target volume has shown that HP technique provides better performance when compared to some of the conventional time-domain approaches.

The work in this thesis has been based on the assumption that a significant contrast exists between the dielectric properties of normal and malignant tissues. Recent investigation however, indicate that this contrast exists between malignant and fatty (or adipose) breast tissue, while the contrast between malignant and healthy fibroglandular tissues can be as low as 10% in both permittivity and conductivity. In addition, other important factors such as the presence of skin reflection, spine signals and dense tissues which would make the imaging problem more challenging need to be carefully considered and investigated.

7.2 Future Work

Like any other technique during its first years of development, the two methods introduced in this thesis still have a lot of room for improvement before they can be used in clinical applications such as breast cancer detection, internal organ imaging, and whole body imaging.

A major change that should be made to the current experimental set up would be the use of an array of antennas as transmitters and receivers, in order to achieve multiple simultaneous measurements which would reduce time and increase the accuracy of the measurements. Current set up uses one single transmitting and receiving antennas, which requires manual movement of the transmitting antenna to the next position after each set of measurement, which means there is a possibility of human error. Measurement time may also be reduced by increasing the number of VNAs; having twenty VNAs instead of one would reduce the measurement time by a factor of 20, while the cost of the imaging procedure would still be less than most already existing methods.

One source of improvement is the use of a consistent frequency range for all future measurements. Different frequency bands and samplings were used depending on the media under investigation, and in some cases due to the high losses of the medium, a low frequency range (compared to UWB standards) of 1-1.6 GHz or 1-3 GHz was employed. It is known that increasing the frequency also increases the resolution of the image; therefore, in future, transmitter amplifiers will be implemented in all measurements to increase the frequency band, and hence the resolution.

Although a detailed computational analysis regarding the performance of HP was presented in the thesis, more investigation on the lowest number of receiving points which can be used, minimum power level applicable and detectable contrast with respect to the permittivity is required. Moreover, only two types of UWB antennas (bow-tie and discone) were used in the measurements. More investigation on other types of antennas and their effect on imaging result is also needed.

Concerning the MM method, further research should focus on the investigation on the robustness with respect to errors in the measurement grid and knowledge of the dielectric properties of the target volume. Furthermore, a quantitative investigation on the detectable dielectric contrast with respect to the frequency band is also required. Also, the extension of the method to geometries other than cylinders needs to be investigated. This could be possible by replacing Bessel functions with Mathieu functions or spherical Bessel functions if ellipsoidal and spherical problems are encountered. An extension to more realistic 3D geometries is possible by resorting to the extraction of the modes as explained earlier in the thesis.

Bibliography

[1] G. F. Ross, “Transmission and reception system for generating and receiving base-band duration pulse signals for short base-band pulse communication system,” U.S. Patent 3,728,632, 1973.

[2] C. L. Bennett and G. F. Ross, “Time-domain electromagnetics and its applications,” *Proceedings of the IEEE*, vol. 66, no. 3, pp. 299–318, 1978.

[3] A. Papoulis, *The Fourier Integral and Its Applications*. McGraw-Hill, New York, Chapter 5, 1962.

[4] “Time domain.” `http://www.timedomain.com` .

[5] “Xtremespectrum.” `http://www.xtremespectrum.com` .

[6] A. Leimer, *TCB Workshop Ultra-Wideband (UWB)*. Office of Engineering and Technology/Equipment Authorization Branch FCC Laboratory, May 2004.

[7] S. k. Jones, *The Evolution of Modern UWB Technology: A Spectrum Management Perspective*. FCC/OET Laboratory Technical research Branch, May 2005.

[8] L. Yang and G. B. Giannakis, “Ultra-Wideband communications: An idea whose time has come,” *IEEE Signal Processing Magazine*, vol. 21, no. 6, pp. 26–54, Nov. 2004.

[9] D. Porcino and W. Hirt, “Ultra-Wideband radio technology: Potential and challenges ahead,” *IEEE communications Magazine*, vol. 41, no. 7, pp. 66–74, Jul. 2003.

[10] M. Ghavami, L. Michael, and R. Kohno, *Ultra Wideband signals and systems in communication engineering*. John Wiley & Sons, 2nd ed., Jan. 2007.

[11] "UWB Tutorial." Wireless2000: RF and UWB Technologies.

[12] "Mit educational project for the radar stethoscope." Massachusetts Institute of Technology, Department of Mechanical Engineering, Mar. 1995.

[13] T. E. McEwan, "Body monitoring and imaging apparatus and method," US Patent No. 5,573,012, Issued on November 12, 1996.

[14] J. Pan, "Medical applications of Ultra-Wideband (UWB)." , survey paper.

[15] C. R. Hill and G. R. Ter-Harr, "Review article: High intensity focused ultrasound-potential for cancer treatment," *British Journal of Radiology*, vol. 68, no. 816, pp. 1296–1303, Dec. 1995.

[16] R. F. Cotellessa *et al.*, *Principle of Computerized Tomography*. IEEE Free Press, 1987.

[17] "Mammography and beyond: Developing techniques for the early detection of breast cancer." Washington, DC: Institute of Medicine, National Academy Press, 2000.

[18] A. H. Golnabi, P. M. Meaney, S. Geimer, T. Zhou, and K. D. Paulsen, "Microwave tomography for bone imaging," in *Biomedical Imaging: From Nano to Macro, 2011 IEEE International Symposium on*, pp. 956–959, 2011.

[19] P. M. Meaney, D. Goodwin, A. Golnabi, M. Pallone, S. Geimer, and K. D. Paulsen, "3d microwave bone imaging," in *Antennas and Propagation (EUCAP), 2012 6th European Conference on*, pp. 1770–1771, 26-30 Mar. 2012.

[20] P. M. Meaney and K. D. Paulsen, "Nonactive antenna compensation for fixed-array microwave imaging: Part II: Imaging results," *IEEE Transactions on Medical Imaging*, vol. 18, no. 6, pp. 508–518, Jun. 1999.

[21] D. W. Winters, B. D. Van-Veen, and S. C. Hagness, “A sparsity regularization approach to the electromagnetic inverse scattering problem,” *IEEE Transactions on Antennas and Propagation*, vol. 58, no. 1, pp. 145–154, Jan. 2010.

[22] S. Kusiak and J. Sylvester, “The scattering support,” *Communications on Pure and Applied Mathematics*, vol. 56, no. 11, pp. 1525–1548, 2003.

[23] S. Kusiak and J. Sylvester, “The convex scattering support in a background medium,” *SIAM Journal on Mathematical Analysis*, vol. 36, no. 4, pp. 1142–1148, 2005.

[24] M. Chiappe and G. L. Gragnani, “An analytical approach to the reconstruction of the radiating currents in inverse electromagnetic scattering,” *Microwave and Optical Technology Letters*, vol. 49, no. 2, pp. 354–360, Feb. 2007.

[25] G. L. Gragnani, “Two-dimensional non-radiating currents for imaging systems: Theoretical development and preliminary assessment,” *Microwaves, Antennas and Propagation, IET*, vol. 3, no. 8, pp. 1164–1171, Dec. 2009.

[26] X. Li and S. C. Hagness, “A confocal microwave imaging algorithm for breast cancer detection,” *Microwave and Wireless Components Letters, IEEE*, vol. 11, no. 3, pp. 130–132, Mar. 2001.

[27] E. C. Fear, X. Li, S. C. Hagness, and M. A. Stuchly, “Confocal microwave imaging for breast cancer detection: Localization of tumors in three dimensions,” *IEEE Transactions on Biomedical Engineering*, vol. 4, no. 8, pp. 812–822, Aug. 2002.

[28] E. J. Bond, X. Li, S. C. Hagness, and B. D. V. Veen, “Microwave imaging via space-time beamforming for early detection of breast cancer,” *IEEE Transactions on Antennas and Propagation*, vol. 51, no. 8, pp. 1690–1705, Aug. 2003.

[29] X. Li, S. K. Davis, S. C. Hagness, D. W. van der Weide, and B. D. VanVeen, “Microwave imaging via space-time beamforming: Experimental investigation of tumor detection in

multilayer breast phantoms," *IEEE Transactions on Microwave Theory and Techniques*, vol. 52, no. 8, pp. 1856–1865, Aug. 2004.

[30] M. Klemm, I. J. Craddock, J. A. Leendertz, A. Preece, and R.Benjamin, "Radar-based breast cancer detection using a hemispherical antenna array: Experimental results," *IEEE Transactions on Antennas and Propagation*, vol. 57, no. 6, pp. 1692–1704, Jun. 2009.

[31] P. Kosmas and C. M. Rappaport, "Time reversal with the FDTD method for microwave breast cancer detection," *IEEE Transactions on Microwave Theory and Techniques*, vol. 53, no. 7, pp. 2317–2323, Jul. 2005.

[32] Y. Chen, E. Gunawan, K. S. Low, Y. K. S. Wang, and C. B. Soh, "Pulse design for time reversal method as applied to Ultrawideband microwave breast cancer detection: A two-dimensional analysis," *IEEE Transactions on Antennas and Propagation*, vol. 55, no. 1, pp. 194–204, Jan. 2007.

[33] R. K. Amineh, M. Ravan, A. Khalatpour, and N. K. Nikolova, "Three-dimensional near-field microwave holography using reflected and transmitted signals," *IEEE Transactions on Antennas and Propagation*, vol. 59, no. 12, pp. 4777–4789, 2011.

[34] P. S. Hall, Y. Hao, Y. I. Nechayev, A. Alomalny, C. C. Constantinou, C. Parini, M. R. Kamarudin, T. Z. Salim, D. T. M. Hee, R. Dubrovka, A. S. Owadally, W. Song, A. Serra, P. Nepa, M. Gallo, and M. Bozzetti, "Antennas and propagation for on-body communication systems," *IEEE Antennas and Propagation Magazine*, vol. 49, no. 3, pp. 41–58, Jun. 2007.

[35] Y. Zhao, Y. Hao, A. Alomainy, and C. Parini, "UWB on-body radio channel modeling using ray theory and subband FDTD method," *IEEE Transactions on Microwave Theory and Techniques*, vol. 54, no. 4, pp. 1827–1835, Jun. 2006.

[36] D. A. Mcnamara, C. Pistorius, and J. Malherbe, *Introduction to the Uniform Geometrical Theory of Diffraction*. Boston, MA: Artech House, 1991.

[37] B. G. Korenev, *Bessel Functions and Their Applications*. CRC Press, 2002.

[38] F. E. Relton, *Applied Bessel Functions*. Blackie and Son Limited, 1946.

[39] E. T. Bell, *Men of Mathematics: The Lives and Achievements of the Great Mathematicians from Zeno to Poincar*, pp. 131–138. New York: Simon and Schuster, 1986.

[40] J. F. W. Herschel, *A brief notice of the life, researches, and discoveries of Friedrich Wilhelm Bessel*. London: Barclay, 1847.

[41] M. Abramowitz and I. A. Stegun, *Handbook of Mathematical Functions with Formulas, Graphs, and Mathematical Tables*, p. 360. New York: Dover, 9th ed., Jan. 2007.

[42] G. N. Watson, *A Treatise on the Theory of Bessel Functions*. Cambridge University Press, 2nd ed., 1995.

[43] M. Abramowitz and I. A. Stegun, *Handbook of Mathematical Functions with Formulas, Graphs, and Mathematical Tables*, p. 358. New York: Dover, 9th ed., Jan. 2007.

[44] M. Abramowitz and I. A. Stegun, *Handbook of Mathematical Functions with Formulas, Graphs, and Mathematical Tables*, pp. 374–375. New York: Dover, 9th ed., Jan. 2007.

[45] R. F. Harrington, *Time-Harmonic Electromagnetic Fields*. McGraw-Hill Book Company, 1961.

[46] R. P. Parrikar, A. A. Kishk, and A. Z. Elsherbeni, "Scattering from an impedance cylinder embedded in a nonconcentric dielectric cylinder," *Microwaves, Antennas and Propagation, IEE Proceedings H*, vol. 138, no. 2, pp. 169–175, 1991.

[47] A. A. Kishk, R. P. Parrikar, and A. Z. Elsherbeni, "electromagnetic scattering from an eccentric multilayered circular cylinder," *IEEE Transactions on Antennas and Propagation*, vol. 40, no. 3, pp. 295–303, Mar. 1992.

[48] C. Gabriel, S. Gabriel, and E. Corthout, "The dielectric properties of biological tissues: I. literature survey," *Physics in Medicine and Biology*, vol. 41, no. 11, pp. 2231–2249, 1996.

[49] J. A. Stratton, *Electromagnetic Theory*. McGraw-Hill Book Company, 1941.

[50] A. Fort, F. Keshmiri, G. R. Crusats, C. Craeye, and C. Oestges, "A body area propagation model derived from fundamental principles: Analytical analysis and comparison with measurements," *IEEE Transactions on Antennas and Propagation*, vol. 58, no. 2, pp. 503–514, 2010.

[51] C. Zhou and R. C. Qiu, "Pulse distortion caused by cylinder diffraction and its impact on UWB communications," *IEEE Transactions on Vehicular Technology*, vol. 56, no. 4, pp. 2385–2390, Jul. 2007.

[52] K. Iizuka, "An agar-agar chamber for study of electromagnetic waves in an inhomogeneous medium," *IEEE Transactions on Antennas and Propagation*, vol. 19, no. 3, pp. 365–377, May 1971.

[53] T. Yorkey, "Comparing reconstruction methods for electrical impedance tomography." PhD Thesis, University of Wisconsin, 1986.

[54] D. Bennett, "NaCl doping and the conductivity of agar phantoms," *Materials Science & Engineering C*, vol. 31, no. 2, pp. 494–498, 2011.

[55] G. Tiberi, N. Ghavami, D. J. Edwards, and A. Monorchio, "UWB body area network channel modeling: an analytical approach," *AEUE - International Journal of Electronics and Communications*, vol. 66, no. 11, pp. 913–919, Nov. 2012.

[56] A. Wexler, "Solution of waveguides discontinuities by modal analysis," *IEEE Transactions on Microwave Theory and Techniques*, vol. 15, no. 9, pp. 508–517, Sep. 1967.

[57] J. Zheng and M. Yu, "Rigorous mode-matching method of circular to off-center rectangular side-coupled waveguide junctions for filter applications," *IEEE Transactions on Microwave Theory and Techniques*, vol. 55, no. 11, pp. 2365–2373, Nov. 2007.

[58] D. Arena, M. Ludovico, G. Manara, and A. Monorchio, "Analysis of waveguide discontinuities using edge elements in a hybrid mode matching/finite elements approach," *Microwave and Wireless Components Letters, IEEE*, vol. 11, no. 9, pp. 379–381, Sep. 2001.

[59] M. El-Shenawee and E. L. Miller, "Spherical harmonics microwave algorithm for shape and location reconstruction of breast cancer tumor," *IEEE Transactions on Medical Imaging,*, vol. 25, no. 10, pp. 1258–1271, Oct. 2006.

[60] A. G. Radwan, M. H. Bakr, and N. K. Nikolova, "Transient adjoint sensitivities for discontinuities with gaussian material distributions," *Progress In Electromagnetics Research B*, vol. 27, pp. 1–19, 2011.

[61] G. Tiberi, "Modelling Ultra Wideband radio propagation in human body." Intra-European Fellowships (IEF), final report, 2010.

[62] G. Tiberi, N. Ghavami, D. J. Edwards, and A. Monorchio, "A mode matching bessel functions based approach for UWB microwave imaging," *Antennas and Propagation Society International Symposium (APSURSI), 2010 IEEE*, pp. 1–4, 11-17 July 2010.

[63] N. Ghavami, G. Tiberi, D. J. Edwards, and A. Monorchio, "UWB microwave imaging of objects with canonical shape," *IEEE Transactions on Antennas and Propagation*, vol. 60, no. 1, pp. 231–239, 2012.

[64] N. K. Nikolova, "Microwave imaging for breast cancer," *IEEE Microwave Magazine*, vol. 12, no. 7, pp. 78–94, Dec. 2011.

[65] G. Tiberi, N. Ghavami, D. J. Edwards, and A. Monorchio, “A mode matching bessel functions based approach for UWB microwave imaging: Validation through measurements,” in *proc. of 2010 AP-S/URSI conference*, Toronto, Jul. 2010.

[66] T. Onishi and S. Uebayashi, “Biological tissue-equivalent phantoms usable in broadband frequency range,” *NTT DoCoMo Technical Journal*, vol. 7, no. 4, pp. 61–65, 2006.

[67] D. Frenkel and R. Portugal, “Algebraic methods to compute mathieu functions,” *Journal Of Physics A: Mathematical And General*, vol. 34, pp. 3541–3551, 2001.

[68] F. P. Mechel, *Mathieu Functions: Formulas, Generation, Use.* Stuttgart, Germany: Hirzel, 1997.

[69] G. Arfken, “Spherical bessel functions,” in *Mathematical Methods for Physicists*, pp. 622–636, Orlando, FL: Academic Press, 3rd ed., 1985.

[70] E. Lucente, G. Tiberi, A. Monorchio, G. Manara, and R. Mittra, “The characteristic basis function method (CBFM): A numerically efficient strategy for solving large electromagnetic scattering problems,” *Turkish Journal of Electrical Engineering & Computer Sciences*, vol. 16, no. 1, pp. 41–56, 2008.

[71] E. Lucente, A. Monorchio, and R. Mittra, “An iteration free mom approach based on excitation independent characteristic basis functions for solving large multiscale electromagnetic scattering problems,” *IEEE Transactions on Antennas and Propagation*, vol. 56, no. 4, pp. 999–1007, Apr. 2008.

[72] P. Enders, “Huygens principle as universal model of propagation,” *Latin American Journal of Physics Education*, vol. 3, no. 1, pp. 19–32, Jan. 2009.

[73] R. S. Longhurst, *Geometrical and Physical Optics.* Longman, 3rd ed., 1973.

[74] R. P. Porter and A. J. Devaney, “Holography and the inverse source problem,” *Journal of the Optical Society of America*, vol. 72, no. 3, pp. 327–330, 1982.

[75] A. J. Devaney and R. P. Porter, "Holography and the inverse source problem. part ii: Inhomogeneous media," *Journal of the Optical Society of America*, vol. 2, no. 11, pp. 2006–2012, 1985.

[76] Y. Xu and L. V. Wang, "Time reversal and its application to tomography with diffracting sources," *Physical Review Letters*, vol. 92, no. 3, 2004.

[77] X. Zhuge, T. G. Savelyev, A. G. Yarovoy, L. P. Ligthart, and B. Levitas, "Comparison of different migration techniques for UWB short-range imaging," *European Radar Conference,EuRAD 2009*, pp. 184–187, 30 Sep. - 2 Oct. 2009.

[78] G. Tiberi, N. Ghavami, D. J. Edwards, and A. Monorchio, "Ultrawideband microwave imaging of cylindrical objects with inclusions," *Microwaves, Antennas & Propagation, IET*, vol. 5, no. 12, pp. 1440–1446, Sep. 2011.

[79] N. Ghavami, G. Tiberi, and D. J. Edwards, "Huygens principle-based approach for UWB medical imaging," in *41st European Microwave Conference (EuMC)*, pp. 1257–1260, Oct. 2011.

[80] G. Lerosey, J. De-Rosny, A. Tourin, and M. Fink, "Focusing beyond the diffraction limit with far-field time reversal," *Science*, vol. 315, no. 10, pp. 1120–1122, Feb. 2007.

[81] K. Parker, M. Doyley, and D. Rubens, "Imaging the elastic properties of tissue: the 20 year perspective," *Physics in Medicine and Biology*, vol. 56, no. 1, pp. R1–R29, 2011.

[82] J. Ophir, I. Cspedes, H. Ponnekanti, Y. Yazdi, and X. Li, "Elastography: a quantitative method for imaging the elasticity of biological tissues," *Ultrasonic Imaging*, vol. 13, pp. 111–134, 1991.

[83] H. Mehrabian and A. Samani, "An iterative hyperelastic parameters reconstruction for breast cancer assessment," in *proc. of SPIE conference*, vol. 6916, 2008.

[84] A. Kurjak and F. A. Chervenak, *Donald School Textbook of Ultrasound in Obstetrics and Gynecology*, pp. 792–793. JP Medical Ltd, Sep. 2011.

[85] T. A. Krouskop, T. M. Wheeler, F. Kallel, B. S. Garra, and T. Hall, "Elastic moduli of breast and prostate tissues under compression," *Ultrasonic Imaging*, vol. 20, pp. 260–274, 1998.

[86] C. Christopoulos, *The Transmission Line Modeling Method: TLM*. Piscataway, NY, IEEE Press, 1995.

[87] A. Chmielewski, "Ultrawideband medical imaging." Supervised by Prof David Edwards and Navid Ghavami, Final Honour School of Engineering part II, 2011.

[88] Computerized Imaging Reference Systems Inc, 23513, Norfolk, Virginia, USA, *Breast Elastography Phantom (model 059)*, 2008.

[89] M. B. Zerhouni and M. Rachedine, "Ultrasonic calibration material and method," U.S. Patent 5196343, Mar. 1993.

[90] J. Mende, M. Radicke, A. L. Kofahl, J. Schindler, D. Ulucay, J. Finsterbusch, B. Weber, and K. Maier, "Detecting breast phantom lesions with acoustic radiation force in MR images: experiment and finite-element simulations," in *ISMRM 18th Scientific Meeting & Exhibition, Stockholm*, May 2010.

[91] D. Seabury, "An update on sar standards and the basic requirements for sar assessment," *Conformity, white paper*, April 2005.

[92] "Sar values in mobile phones." `http://www.mobile-phones-uk.org.uk/sar.htm` .